3-2020

Enhanced BRDF Modeling Using Directional Volume Scatter Terms

Michael W. Bishop

ENHANCED BRDF MODELING USING DIRECTIONAL VOLUME SCATTER TERMS

THESIS

Michael W. Bishop, Capt, USAF

AFIT-ENP-MS-20-M-081

DEPARTMENT OF THE AIR FORCE
AIR UNIVERSITY

AIR FORCE INSTITUTE OF TECHNOLOGY

Wright-Patterson Air Force Base, Ohio

AFIT-ENP-MS-20-M-081

ENHANCED BRDF MODELING USING DIRECTIONAL VOLUME SCATTER TERMS

THESIS

Presented to the Faculty

Department of Engineering Physics

Graduate School of Engineering and Management

Air Force Institute of Technology

Air University

Air Education and Training Command

in Partial Fulfillment of the Requirements for the

Degree of Master of Science in Applied Physics

Michael W. Bishop, B.S. Physics

Capt, USAF

26 March 2020

AFIT-ENP-MS-20-M-081

ENHANCED BRDF MODELING USING DIRECTIONAL VOLUME SCATTER TERMS

THESIS

Michael W. Bishop, B.S. Physics
Capt, USAF

Committee Membership:

Lt Col Samuel D. Butler, Ph.D.
Chairman

Michael. A. Marciniak, Ph.D.
Member

Maj Tyler. J. Hardy, Ph.D.
Member

Abstract

Accurate Bidirectional Reflectance Distribution Function (BRDF) models provide critical scatter behavior for computer graphics and remote sensing performance. The popular microfacet class of BRDF models is geometric-based and computationally inexpensive compared to wave-optics models. Microfacet models commonly account for surface scatter and Lambertian volume scatter, but not directional volume scatter. This work proposes directional volume scatter modeling for enhanced performance over all observation regions. Five directional volume models are incorporated into the modified Cook-Torrance microfacet model. Additionally, a semi-empirical directional volume term is presented based on the Beckmann microfacet distribution and a modified Fresnel reflection term. High fidelity, low density data from 15 datasets are fit to each hybrid model using a recursive optimization method then compared to the baseline Cook-Torrance model. By including a directional volume term, analysis shows fit quality is improved based on the square of the mean standard error (MSE^2) by as much as 78% and backscatter agreement is improved by as much as 92%. Including the semi-empirical, Oren-Nayar, or Beard-Maxwell directional volume term reduced backscatter MSE^2 across datasets exhibiting high volume scatter by an average of 52%, 46%, and 26% respectively. Directional volume terms showed statistically insignificant improvement for low volume scatter materials, while full model improvements were apparent across all high volume scatter visually diffuse materials. Results suggest directional volume scatter modeling can consistently improve full model fit quality with emphasized model agreement for backscatter observations. These results validate directional volume scatter significance and are expected to lead to enhanced remote sensing and scene generation.

Acknowledgements

"Seeming to do is not doing." Thomas Edison

This material is based upon work supported by the Air Force Office of Scientific Research under award number F4FGA09014J002. The author would also like to thank Joe Costantino of the Air Force Research Lab, Materials and Manufacturing Directorate for selecting and providing the BRDF data used in this work. Additional thanks to Dr. Marciniak, Lieutenant Colonel Butler, and Major Hardy for their patience, guidance, and mentorship throughout this learning process. Most importantly, to my wonderful wife, thank you for your enduring love, support, and friendship.

Michael W. Bishop

Table of Contents

Page

Abstract iv

Acknowledgements v

List of Figures viii

List of Tables xi

I. Overview 1

II. BRDF Theory and Background 5

2.1 Foundational Electromagnetism 5
2.2 Scatter Theory 7
2.3 Surface Reflection 9
2.4 The Radiometric Model 12
2.5 BRDF Principles and the Cook-Torrance Microfacet Model 18
2.6 Volumetric BRDF Models 24
2.6.1 Roujean 24
2.6.2 Modified Beard-Maxwell 28
2.6.3 Sandford-Robertson 30
2.6.4 Modified Walthall 31
2.6.5 Schlick 32
2.6.6 Oren-Nayar 34
2.6.7 Kubelka-Munk 35

III. Methodology 41

3.1 Measurement and Samples 42
3.2 Empirical Directional Volumetric Scatter Term Formulation 44
3.3 Volumetric Model Comparison 48
3.3.1 Optimized Simulation 51
3.3.2 Error Metrics 55

IV. Results 58

4.1 Rough Surface Comparison 59
4.2 Polished Surface Comparison 74
4.3 NIST Standards Comparison 79
4.4 Summary of Results 83

Page

V. Conclusion 89

Appendix A. All Fitted Models 92

Bibliography 113

List of Figures

Figure		Page
1	Spherical Geometry	10
2	Radiometric Model	12
3	Source and Apparent Signal Contributions Diagram	17
4	Specular and Diffuse Surface Reflection	20
5	Macrosurface and Microsurface Coordiante Geometry	21
6	Roujean Subsurface Scatter Geometry	26
7	Duplicated Roujean Surface and Volume Plots	28
8	Kubelka-Munk Volumetric Scatter Geometry	37
9	BRDF Imaging System Diagram	43
10	Semi-empirical Backscatter Lobe Equivalence Plot	47
11	Spherical Plot of Model 2	48
12	Idealized Test Data Plot	52
13	Tests Data With Random Noise	53
14	Optimization Algorithm Fit to Test Data	54
15	Optimization Algorithm Fit to Actual Data	54
16	PNT65 NIR Fit Plots	60
17	Error Bar Chart By Region Explained	61
18	PNT65 NIR Error Bar Chart	62
19	PNT65 MWIR Results	64
20	PNT65 LWIR Results	65
21	PNT65 UV Results	66
22	PNT65 VIS Results	67

Figure Page

23 PNT66 NIR Results . . . 68

24 PNT66 MWIR Results . . . 69

25 PNT66 UV Results . . . 70

26 PNT36375 NIR Results . . . 71

27 PNT36375 NIR Backscatter Results . . . 72

28 PNT36495 VIS Results . . . 73

29 PNT36495 VIS Backscatter Results . . . 74

30 PNT01006 NIR Results . . . 76

31 PNT01006 NIR Backscatter Results . . . 77

32 PNT01014 NIR Results . . . 78

33 PNT01014 NIR Backscatter Results . . . 79

34 STD00696 MWIR Results . . . 80

35 STD00698 MWIR Results . . . 81

36 STD00698 MWIR Backscatter Results . . . 82

37 STD00699 MWIR Results . . . 83

38 Resulting six models fit to diffuse paint PNT65 illuminated by a NIR source. . . . 93

39 Resulting six models fit to diffuse paint PNT65 illuminated by a MWIR source. . . . 94

40 Resulting six models fit to diffuse paint PNT65 illuminated by a LWIR source. . . . 95

41 Resulting six models fit to diffuse paint PNT65 illuminated by an UV source. . . . 96

42 Resulting six models fit to diffuse paint PNT65 illuminated by a VIS source. . . . 97

Figure Page

43 Resulting six models fit to diffuse paint PNT66 illuminated by a NIR source 98

44 Resulting six models fit to diffuse paint PNT66 illuminated by a MWIR source. 99

45 Resulting six models fit to diffuse paint PNT66 illuminated by an UV source. 100

46 Resulting six models fit to diffuse paint PNT36375 illuminated by a NIR source. 101

47 All PNT36375 NIR Backscatter Results 102

48 Resulting six models fit to diffuse paint PNT36495 illuminated by a VIS source. 103

49 All PNT36495 VIS Backscatter Results 104

50 Resulting six models fit to glossy paint PNT01006 illuminated by a NIR source. 105

51 All PNT01006 NIR Backscatter Results 106

52 Resulting six models fit to glossy paint PNT01014 illuminated by a NIR source. 107

53 All PNT01014 NIR Backscatter Results 108

54 Resulting six models fit to NIST standard STD00696 illuminated by a MWIR source. 109

55 Resulting six models fit to NIST standard STD00698 illuminated by a MWIR source. 110

56 All STD00698 MWIR Results 111

57 Resulting six models fit to NIST standard STD00699 illuminated by a MWIR source 112

List of Tables

Table		Page
1	Radiometric Parameters	14
2	Summary of Data	44
3	Hybrid Model Parameter Summary	51
4	Parameter Bounds	52
5	Number of Parameters by Model	84
6	Improvement Table (%)	86

ENHANCED BRDF MODELING USING DIRECTIONAL VOLUME SCATTER TERMS

I. Overview

Light reflected at opaque surfaces can be modeled mathematically according to the direction of the incoming light and light direction upon reflection. Such a light reflection description is widely employed in computer graphics, medical imaging, multilayer color printing, resource monitoring, weather modeling, and paint development industries. Hyperspectral imaging, also known as imaging spectroscopy is an example application that is of particular interest to the Department of Defense (DoD). Hyperspectral imaging is an advanced remote sensing technique combining imaging and spectroscopy in a single system to provide a densely sampled spectral dataset for man-made material identification, vegetation and resource monitoring, and weather detection. For a complete dataset, one must make assumptions about the direction, magnitude, and wavelength dependency of light reflection off the observed material. Such a reflection description is given by a Bidirectional Reflectance Distribution Function (BRDF) wherein the observed reflection is uniquely described for a given material based on incident illumination geometry and detection geometry. Lab measurements over the full observation space is unrealistic, if not impossible in most cases, and accurate full electromagnetic descriptions are computationally expensive. Therefore, a variety of BRDF models have been developed ranging from purely empirical to full wave optics theory models. Today, China, Russia, and the United States are actively seeking efficient and accurate wavelength scalable BRDF models for a variety of terrestrial and space-based remote sensing mission sets [1, 2].

BRDF databases such as the Nonconventional Exploitation Factors Data System (NEFDS), and data from the National Air and Space Association (NASA) Moderate Resolution Imaging Spectroradiometer (MODIS) utilize microfacet BRDF models. This class of BRDF models provides a geometric approximation for rough surface reflection using idealized linear combinations of surface and subsurface scatter terms.

Microfacet surface reflection descriptions have been modeled extensively and provide the specular lobe most dominantly seen in glossy materials. Subsurface scatter, or volume scatter, has often been approximated as Lambertian diffuse scatter which is an idealized approximation that is largely inconsistent with laboratory observations. A generalized microfacet description describes volume scatter as a linear combination of directional volume scatter and Lambertian volume scatter. Common BRDF models often neglect the directional volume term leading to models that are inconsistent with laboratory measurement. Inconsistencies are particularly true for backscatter observations where detection is in the same hemispherical region as the illumination source. The backscatter scene geometry was historically less likely for passive solar illumination; however, increasing presence of active illumination sources will increase the need to improve existing models for backscatter geometries.

A rigorous study of directional volume scatter and its impact on microfacet modeling fit quality is required. Several directional volume BRDF models are described in Chapter 2. High fidelity, low density data collected from nine different materials at five illumination wavelengths is fit to five hybrid models using a non-linear least-squares optimization algorithm as described in Chapter 3. Each hybrid model includes the Cook-Torrance microfacet surface and Lambertian term, and an added directional volume scatter term. Directional volume terms were extracted from Kubelka-Munk, Beard-Maxwell, Sandford-Robertson, Oren-Nayar, and Roujean BRDF models for application in each hybrid model. This study robustly categorizes and compares di-

rectional volume scatter models when applied to the generalized microfacet form. A semi-empirical BRDF model was developed as a baseline comparison for the study. Each hybrid model, including the semi-empirical directional volume baseline, was compared to the baseline Cook-Torrance model. Results and analysis in Chapter 4 show fit performance of each model and highlight performance gains observed by adding a directional volume scatter term.

Results suggest incorporating a directional volume scatter term can consistently improve overall quality of fit and significantly improve model agreement with backscatter observations for high volume scatter materials. Improvements to fit quality are observed in all materials and across all hybrid models, but are most significant in visually diffuse materials that exhibit high volume scatter. The semi-empirically derived directional volume term particularly improves model fit based on the square of the mean standard error (MSE^2) for backscatter observations. This is due to the directional volume term's highly specular backscatter lobe that is characteristically similar to observations of directional subsurface scatter. Full model MSE^2 reductions greater than 67% are observed when implementing the Beard-Maxwell or Oren-Nayar directional volume terms. Fit quality improvements are minimal for low volume scatter materials where fit agreement is largely dictated by the quality of the surface scatter term.

Adding a directional volume scatter term can be unnecessary for materials with approximately Lambertian diffuse scatter behavior. For these materials, the best fit solutions minimize the directional volume term and can be equivalent to the unmodified Cook-Torrance model. Preliminary results agree with anticipated model improvement areas, specifically reducing MSE^2 in the backscatter grazing region to result in full model improvement.

Large improvements to fit quality can be gained by including a directional volume

scatter term with minimal risk of increasing backscatter MSE and no risk of increasing total model mean standard error. Applications such as passive detection of objects in backscatter geometries will benefit most by including a directional volume scatter term.

Resulting contributions of this thesis work include:

- Development of a multi-lobe semi-empirical directional volumetric term
- Robust categorization of several directional volume scatter models for several materials and wavelengths
- Hybrid model development and comparison to the Cook-Torrance model
- Validation of directional volume scatter term significance in BRDF modeling
- Identification of need for a Rayleigh-based physical BDRF model
- Correction to the Yang modifed Kubelka-Munk model

Existing applications have need for a predictive physical BRDF model that is both wavelength scalable and accurate for a range of material types. This research lays the foundational volumetric scatter work necessary to achieve that objective.

II. BRDF Theory and Background

This chapter introduces BRDF theory and the supporting mathematical construct of reflection and scatter theory for volumetric BRDF models. A progression from foundational electromagnetism to surface scatter and surface reflection leads to a description of sub-surface scatter principles and the microfacet model. Canonical BRDF models are introduced with attention to those with directional volumetric terms.

2.1 Foundational Electromagnetism

One must acknowledge that a comprehensive description of light propagation and interaction with opaque surfaces requires application of Maxwell's equations. This concise set of equations established light as an electromagnetic wave and are described in Gaussian units by: [3]

$$\begin{aligned} \nabla \cdot \vec{\boldsymbol{D}} &= 4\pi\rho \\ \nabla \cdot \vec{\boldsymbol{B}} &= 0 \\ \nabla \times \vec{\boldsymbol{E}} &= -\frac{1}{c}\frac{\partial \vec{\boldsymbol{B}}}{\partial t} \\ \nabla \times \vec{\boldsymbol{H}} &= -\frac{4\pi}{c}\vec{\boldsymbol{J}} + \frac{1}{c}\frac{\partial \vec{\boldsymbol{D}}}{\partial t} \end{aligned} \tag{1}$$

where, $\vec{\boldsymbol{D}}$ is the electric displacement, ρ is the charge density following the macroscopic formulation, $\vec{\boldsymbol{B}}$ is the magnetic field, c is the speed of light, $\vec{\boldsymbol{E}}$ is the electric field, $\vec{\boldsymbol{H}}$ is the magnetic intensity and $\vec{\boldsymbol{J}}$ is the free current density. $\vec{\boldsymbol{B}}$ is directly related to $\vec{\boldsymbol{H}}$ by μ which is the permeability of a material. Similarly, $\vec{\boldsymbol{D}}$ is related to $\vec{\boldsymbol{E}}$ by ϵ defined as the permittivity. In an isotropic medium μ and ϵ are scalar quantities.[3].

Maxwell's work showed unique agreement of electromagnetic theory with the scalar description of the wave equation when velocity of the wave was allowed to be described as:[3]

$$v = c/\sqrt{\mu\epsilon}, \tag{2}$$

where μ and ϵ can be determined experimentally. The result predicted the speed of electromagnetic waves in free space to greatly agree with the speed of light, establishing light as a propagating electromagnetic wave with velocity known today:[3]

$$c = 2.99792458 \times 10^8 m/s. \tag{3}$$

The general solution in free space for plane, monochromatic electromagnetic waves are transverse waves having the form:[3]

$$\boldsymbol{\Psi}(\boldsymbol{r}, t) = \vec{\boldsymbol{A}} e^{i(\boldsymbol{k}\cdot\boldsymbol{r} - \omega t)}, \tag{4}$$

where $\vec{\boldsymbol{A}}$ is a constant vector, $\boldsymbol{k}$ is the propagation vector, $\boldsymbol{r}$ is the direction vector, ω is the angular frequency where $\omega = 2\pi f$ with f defined as the frequency, and t is time.

As shown in Equation (2), wave velocity depends on properties of the propagating medium described by ϵ and μ. Maxwell's description links electromagnetic theory and optical material characteristics by defining n, the index of refraction of a material as:[3]

$$n = \sqrt{\epsilon\mu} \tag{5}$$

where the index of refraction describes the magnitude of the propagation vector $\boldsymbol{k}$ by:[3]

$$|\boldsymbol{k}| = n\frac{\omega}{c} = \frac{2\pi}{\lambda}. \tag{6}$$

Equation (6) nicely links optical theory with electromagnetics for non-conducting media.[3]

Focus in this chapter has been placed on the interaction of light and electromagnetic waves within a material of defined volume. Boundary conditions assume free space is defined outside the material and the index of refraction defines the boundary within the material so light traveling inside the material travels at speed $v \neq c$. These conditions lay the framework to characterize surface reflection and volumetric scatter, as further defined in this chapter.

2.2 Scatter Theory

For a material interacting with incident electromagnetic waves, generally two atomic reactions can occur. If the incident light is of proper energy, the light can be absorbed, exciting the atom to the next energy level. In solids, this phenomenon occurs in solids only at resonant energy levels large enough to jump the energy gap. The other atomic reaction is non-resonant scatter. Incident photons with too little energy collide elastically with atoms in the media. After collision, electrons are set in vibrational motion oscillating about the atomic nucleus. The result is scatter, or re-radiation of the incident energy.[4] This collision and re-radiation is foundational to BRDF scatter theory, atoms colliding with incident light behave much like spherical point sources radiating electromagnetic wavelets in random directions.[3, 4] Scatter occurs at the boundary allowing a portion of the incident light to forward propagate into the material. Each successive interaction continues re-emission resulting in continued forward propagation as well as backward propagation toward the surface. Several specific types of electromagnetic scatter are defined, each uniquely dependent on particle size, charge, or relative orientation. This work does not focus on resonant absorption. Next, three types of non-resonant scatter is discussed.

Mie Scatter is a description of spherical scatter that differs from Rayleigh scatter for large particle sizes on the order of a $(1-10)\lambda$. Mie Scatter is weakly dependent on wavelength, particularly at particle sizes well beyond λ. The intensity of scattered radiation can be found by expanding the incident spherical wave function into a series of extinction, scattering, and absorption efficiency coefficients using Bessel functions and a set of infinite series terms. The result is a strong forward scatter lobe much like an antenna. The forward lobe becomes increasingly dominant as particle size increases. A small particle approximation to Mie scatter is Rayleigh scatter.[4]

Rayleigh scatter often refers to scattering of light caused by the molecules in the Earth's atmosphere. These molecules can be as large as 1/10 of the incident wavelength. The wavelength and particle size dependence effects the strength and direction of re-emission. In the early 19^{th} century, Lord Rayleigh found the intensity of this scattered light is inversely proportional to the fourth power of the incident wavelength or $1/\lambda^4$. The intensity received by an observer at distance R from a scatterer of diameter d and refractive index n is given by:[5]

$$I = I_0 \left(\frac{1+\cos^2\theta_s}{2R^2} \right) \left(\frac{2\pi}{\lambda} \right)^4 \left(\frac{n^2-1}{n^2+2} \right)^2 \left(\frac{d}{2} \right)^6, \tag{7}$$

where I_0 is the incident intensity, and θ_s is the scatter angle to the observer. Shorter wavelengths are scattered more than longer wavelengths giving rise to blue skies mid-day and red skies at sunrise and sunset. Additionally, Rayleigh scatter shows equally strong forward scatter and backscatter in plane with the incident light. Scatter is minimized when observation is perpendicular to the incident light. A comparison between the Rayleigh approximation and Mie scatter theory was provided by Li in 2012.[6]

Rutherford scatter is an elastic Coulombic scatter description that relies on the charge of interacting particles. Incident particles of atomic number z_e (alpha particles

in the original 1909 experiment) elastically collide with target atoms with nucleus of atomic number Z_e. Collisional recoil is neglected for collisions where the nucleus of the target particle is sufficiently large compared to the incident particle. By equating the initial kinetic energy to the Coulomb energy of the target point particle, the minimum approach distance D can be found. This is the distance measured from the target nucleus for which an on axis collision will result in perfect backscatter, i.e. a maximum scatter angle of $\theta_s = \pi$. Incident particles that are offset from the direct target line of incidence by distance b will have a small scatter angle less than when $b = 0$ given by:[7]

$$\theta_s = 2\tan^{-1}\left(\frac{D}{2b}\right). \tag{8}$$

Here b is referred to as the impact offset parameter. In Rutherford scatter, this offset from inline collision and the initial kinetic energy defines the scatter angle as opposed to geometric angle of incidence or specular reflection. It is possible that a strong backscatter signal may be observed inline with the scattering particle.[7]

While Rayleigh, Mie, and Rutherford scatter propagate incident light in many directions, some light opposite a surface boundary will scatter specularly backward into the incident plane. This specific scatter defined as reflection is discussed in the following section.

2.3 Surface Reflection

Having mathematically defined a plane wave and scatter theory, consider propagation of a field incident on a boundary at an oblique angle as shown in Figure 1; where $\boldsymbol{z}$ is the vector normal to the boundary. Three field vectors given as incident (i), scattered (s), and transmitted (t) rays, describe the law of specular reflection where the angle of incidence θ_i is equal to the angle of specular reflection θ_s.[4] Combined with Maxwell's equations that define continuity between the tangential components

of $\vec{\boldsymbol{E}}$ and $\vec{\boldsymbol{H}}$, and the normal components of $\vec{\boldsymbol{B}}$ and $\vec{\boldsymbol{D}}$, Snell's law can be derived:[3]

$$n_1 \sin\theta_i = n_2 \sin\theta_t \tag{9}$$

where n_1 and n_2 are the respective index of refraction on each side of the boundary. In general, material index of refraction is described as a complex quantity $\tilde{n} = n + ik$ where n and k are real and complex components of the index respectively.[4]

Further, an incident plane wave's $\vec{\boldsymbol{E}}$ and $\vec{\boldsymbol{B}}$ field can be described by the field components that are either parallel or perpendicular to the surface plane and are used to describe the reflection and transmission magnitude of a wave of given polarization. Under the previously assumed conditions dealing with dielectrics, the set of equations

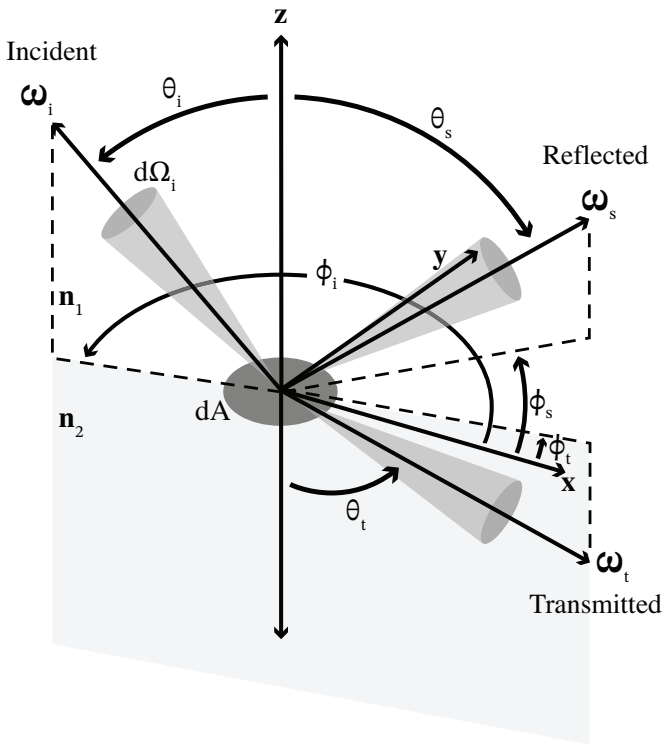

Figure 1. Spherical geometry of incident, scattered, and transmitted radiation

known as the Fresnel equations can be derived and is given by:[3]

$$\begin{aligned} r_s &= \frac{n_i \cos\theta_i - n_t \cos\theta_t}{n_i \cos\theta_i + n_t \cos\theta_t} \\ t_s &= \frac{2n_i \cos\theta_i}{n_i \cos\theta_i + n_t \cos\theta_t} \\ r_p &= \frac{n_t \cos\theta_i - n_i \cos\theta_t}{n_i \cos\theta_t + n_t \cos\theta_i} \\ t_p &= \frac{2n_i \cos\theta_i}{n_i \cos\theta_t + n_t \cos\theta_i}. \end{aligned} \tag{10}$$

Reflection (r) and transmission (t) coefficients are defined so the electric field parallel the plane of incidence is termed $P - Polarized$ indicated by the p subscript. The other component is perpendicular to the plane of incidence and parallel to the material surface and is termed $S - Polarized$ indicated by subscript s.[3] Note the subscript s here specifies the polarization state and is different from the s shown to specify the scattered component of light as shown in Figure 1.

The Fresnel equations describe the electric field reflection coefficient; however, intensity of such reflection is often of greater interest and is described by the magnitude squared of the field reflection coefficient given as:[4]

$$\begin{aligned} F_p &= |r_p|^2 \\ F_s &= |r_s|^2. \end{aligned} \tag{11}$$

For randomly polarized light, the average across both polarization states can be described using:[4]

$$F_u(\theta) = \frac{F_p + F_s}{2}. \tag{12}$$

Polarization is often a consideration in BRDF models and is generally described in models using polarized components of the Fresnel equations.[8, 9, 10] With familiarity of surface reflection, one may form an understanding of the Radiometric model.

2.4 The Radiometric Model

To baseline assumptions made throughout this thesis, this section establishes relevant radiometric theory necessary to understand the BDRF and its relation to the rendering equation.

From the fundamental radiometric quantity, radiant flux Φ_e, one can derive other radiometric quantities such as: radiance (L), intensity (I), irradiance (E), and exitance (M), of which the quantities can be described in photon units denoted by subscript q, or in joule units denoted by subscript e. The later is assumed throughout this thesis. To further radiometric theory, consider the diagram in Figure 2. dA_s is the differential area of an opaque surface, dA_d is an infinitesimal area of the detector, and the two surface normals are offset relative the separation path along $\boldsymbol{r}$ by θ_d and θ_s.[11]

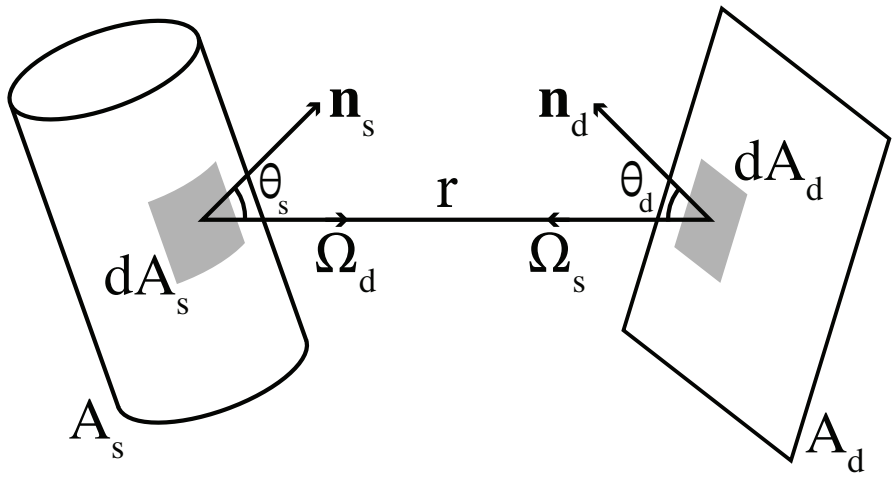

Figure 2. Source radiance from an extended object can vary over the surface and depends on observation geometry defined by the solid angle Ω_d, the tilt of the differential surface areas (dA_s and dA_d) and the distance between source and detector (r).

The differential radiant power, $d^2\Phi_e$, describes the power transferred from an infinitesimal source area to an infinitesimal detector area given as:[11]

$$d^2\Phi_e = L(\hat{\Omega}) \cos\theta_d \, dA_d \, d\Omega_s = L(\hat{\Omega}) \cos\theta_s \, dA_s \, d\Omega_d, \tag{13}$$

where $d\Omega_s$ and $d\Omega_d$ are the projected solid angles subtended by the source and detector at the detector and source respectively. The total power from the source is determined by integrating over the surface area of the source and the surface area of the detector given by: [11]

$$\Phi = \frac{\int_{A_s} \int_{A_d} L(\hat{\Omega}) \cos\theta_s \cos\theta_d \, dA_d \, d_s}{\boldsymbol{r}^2}, \tag{14}$$

where radiance L is the conserved intrinsic quantity that describes the radiation field in a non-participating medium. Aside from gains or losses along the path, radiance is independent of source size, detector size, and scene geometry, making it a practical radiometric quantity. Radiance as the flux per unit solid angle at the detector per unit projected source area is defined by:[12]

$$L = \frac{d^2\Phi_e}{dA_s \cos\theta_s d\Omega_d} \tag{15}$$

where $\cos\theta_s$ arises from the angular variance between the source normal and the line of sight direction.

From the definition of radiance and radiant flux, exitance (M) and irradiance (E) are easily defined. Both are integrated, non-directional quantities where exitance is the flux exiting one side of the source surface and is an integrated value over 2π steradian. Similarly, irradiance is the power received, or flux per unit area incident on a surface over 2π steradian. Together they are expressed by:[12]

$$M_e = \frac{d\Phi_e}{dA_s} = \int_{2\pi} L_e \cos\Theta_s d\Omega_d \tag{16}$$

$$E_e = \frac{d\Phi_e}{dA_d} = \int_{2\pi} L_e \cos\Theta_d d\Omega_s, \tag{17}$$

where the units on exitance and irradiance are the same and the difference is the relative directionality of the flux. Intensity I is often confusingly misused interchangeably with irradiance and exitance. Intensity is the flux per solid angle relative to the detector emitted in a specific direction $\hat{\Omega}$ given by: [12]

$$I_e = \frac{d\Phi_e}{d\Omega_d} = \int_{A_s} L_e \cos\Theta_s dA_s. \tag{18}$$

Intensity is most often appropriate for detection over small angles such as extended point sources. Table 1 summarizes the common radiometric quantities, including units, the symbolic identifier, and the defining relation to radiance through radiant flux.

Symbol	Parameter	Units	Definition
Φ_e	Radiant Flux	Watts	$\frac{dQ_e}{dt}$
Q_e	Radiant Energy	Joules	$\int \Phi_e dt$
L_e	Radiance	Watts $cm^{-2}(sr)^{-1}$	$\frac{d^2\Phi}{dA_s \cos\Theta_s d\Omega_d}$
M_e	Exitance	Watts cm^{-2}	$\frac{d\Phi_e}{dA_s}$
E_e	Irradiance	Watts cm^{-2}	$\frac{d\Phi_e}{dA_d}$
I_e	Intensity	Watts $(sr)^{-1}$	$\frac{d\Phi_e}{d\Omega_d}$

Table 1. Radiometric Parameters

From these radiometric quantities used to describe the transport of light between source and detector, we can consider the generating mechanism for the thermal radiation at the source. In 1900, Max Planck discovered that hot objects emit radiation over a spectral distribution. Some objects can be approximated as a blackbody with spectral radiance L_B described by:[12, 3, 4, 11]

$$L_B(\lambda, T) = \frac{2hc^2}{\lambda^5} \frac{1}{e^{hc/\lambda kT} - 1}, \tag{19}$$

where h is Planck's constant, c is the speed of light, k is the Boltzmann constant, and T is the temperature of the blackbody. Spectral radiance is detected over a specific wavelength interval defined by the sensor design. As such, measured radiance is a function of temperature by integrating over the frequency band of interest which is given as:[11]

$$L_B(T) = \int_{\lambda 1}^{\lambda 2} \frac{2hc^2}{\lambda^5} \frac{1}{e^{hc/\lambda kT} - 1} d\lambda. \tag{20}$$

In practice, most materials are not perfect blackbodies and behave more like a grey-body, a blackbody scaled by an emissivity factor ϵ to account for less than perfect radiative emission from the source. For an object in thermal equilibrium, conservation of energy requires the incident flux on an absorber to be equal to the sum of the reflected flux, the transmitted flux, and the flux absorbed by the object. This can be extended to form the expression $\rho + \tau + \alpha = 1$ where ρ is the reflectance, τ is the transmittance, and α is the absorptance of the object. Each takes on a value between 0 and 1 and are defined by the following:[12]

$$\begin{aligned} \rho &= \frac{\Phi_{reflected}}{\Phi_{incident}} \\ \alpha &= \frac{\Phi_{absorbed}}{\Phi_{incident}} \\ \tau &= \frac{\Phi_{transmitted}}{\Phi_{incident}} \end{aligned} \tag{21}$$

Kirchhoff's Law dictates a material of absorptivity α placed in a blackbody held in thermal equilibrium must emit a total flux equivalent to the flux absorbed by the material, that is $\alpha = \epsilon$. The emissivity of an object then satisfies:[12]

$$\epsilon = 1 - \tau - \rho, \tag{22}$$

which can be further simplified for opaque objects where $\tau = 0$ to obtain $\epsilon = 1 - \rho$, directly relating the reflectance of an object to the emissivity.[11] This subtle yet significant relation is at the heart of accurate BRDF modeling which seeks to accurately describe the directional reflectance and equivalently, the directional emissivity of the material.

One is now well suited to describe a generalized radiometric scenario shown in Figure 3 using the radiance model. One can assume the atmosphere to be a hemispherical shell centered about an object being observed. The equilibrium radiance leaving a point on the object is the sum of the self emitted radiance L_{self} and all reflected radiance terms at that point. The reflected radiance must account for incident radiance from multiple environmental sources. This simple model includes directionally reflected solar radiance L_{sun} and reflected sky radiance L_{sky} attributed to blackbody-like radiance from the surrounding atmosphere. Additional reflection terms may be included such as cloud, star, or contributing terrestrial radiance, but are not included here to maintain simplicity of the theory. The radiance model is then described as:[11]

$$L_{source}(\hat{\omega}_i, \hat{\omega}_s, \lambda) = L_{self}(\hat{\omega}_s, \lambda) + L_{sun}(\hat{\omega}_i, \hat{\omega}_s, \lambda) + L_{sky}(\hat{\omega}_s, \lambda), \tag{23}$$

where $\hat{\omega}_i$ is the incident unit vector consisting of spherical coordinates θ_i and ϕ_i. $\hat{\omega}_s$ is the scattered unit vector pointing from the object in the direction of reflection consisting of spherical coordinates θ_s and ϕ_s. For discussions forward, the assumed orientation is $\phi_i = 0$ which defines the origin at the azimuthal orientation of the incident light. This assumption places the observer at some position relative to the Sun's azimuthal angle and defines backscattered light as $0 < \phi_s < \pi/2$ and $3\pi/2 < \phi_s < 2\pi$. Forward scatter is defined as $\pi/2 < \phi_s < 3\pi/2$ for geometry shown previously in Figure 1. The wavelength of light,λ, is included in Equation (23) to highlight the spectral

dependence of the radiance function. Here the spherical coordinates are given in relation to $\boldsymbol{z}$ which are defined as normal to the object's surface at the point of reflection. In practice, this source radiance model is coupled with atmospheric propagation models and extended with non-reflecting radiance terms to describe the apparent radiance at the observer.

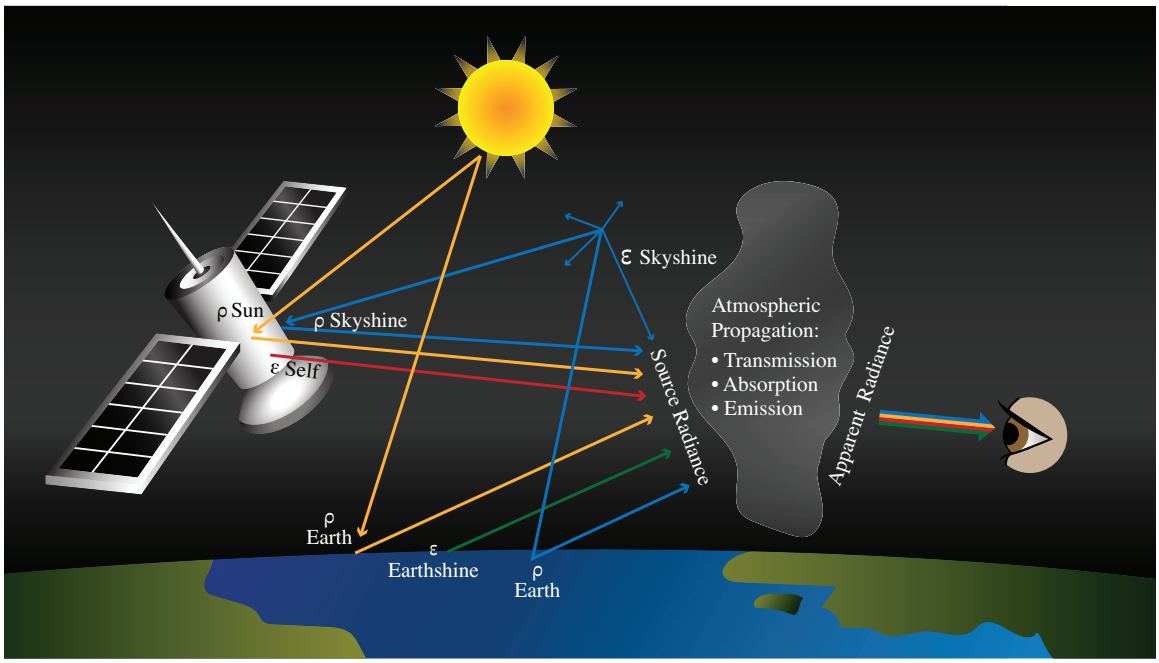

Figure 3. The simplified radiance model shows contributions to the source signal from self emission, Sun, Earth, and skyshine. Atmospheric propagation models can be applied to determine the apparent signal at the observer.

The source radiometric model defines the radiance exiting the surface after reflection. Looking again at each component, the reflected radiance is written in terms of the incident radiance L_i and the reflectance of the object. The rendering equation, given by [13]

$$L_{source}(\hat{\omega}_s, \lambda) = L_{self}(\hat{\omega}_s, \lambda) + \int_{2\pi} BRDF(\hat{\omega}_i, \hat{\omega}_s, \lambda) L_i(\hat{\omega}_i, \lambda) \cos\theta_i \, d\hat{\omega}_i, \tag{24}$$

is often used in computer graphics for scene rendering and equivalently states that the equilibrium radiance leaving a point is the sum of the self-emitted radiance and

the reflected radiance at that point. To get the total reflected radiance in the direction of the detector or observer, the integral of the incident radiance over all incident directions is taken and scaled by the reflectance of the target. This reflectance ρ, as described previously, is not a constant in practice, but is a function of the incident illumination vector and the observation geometry. Understanding this physical approach to a reflectance model leads us to define the BRDF introduced in the following section.

2.5 BRDF Principles and the Cook-Torrance Microfacet Model

A fully inclusive description of material interaction with light is given by the Bidirectional Scatter Distribution Function (BSDF) wherein both the Bidirectional Reflection Distributuion Function (BRDF) and the Bidirectional Transmission Distribution Function (BTDF) combined yield the BSDF. This thesis investigates BRDF specifically for interest in opaque materials when transmission contributions to the apparent signal are negligible. The BRDF f_r is defined as the ratio of the reflected radiance to the incident irradiance as:[14]

$$f_r(\hat{\omega}_i, \hat{\omega}_s) = \frac{dL_r(\hat{\omega}_i, \hat{\omega}_s, \lambda)}{dE_i(\hat{\omega}_i, \lambda)}, \tag{25}$$

where f_r gives the reflectance per solid angle in a given direction in spherical coordinates and has units of sr^{-1}. This convenient description allows the development of reflectance models in terms of illumination and observation geometry.

Consider the definition of reflectance as the ratio of the reflected flux to the incident flux. Dividing out the area of the source and detector yields a ratio of the exitance to the irradiance, [12]

$$\rho = \frac{M_s}{E_i}. \tag{26}$$

For the simplest BRDF, assume a rough Lambertian surface that reflects uniformly over the observation hemisphere by [12]

$$M = \pi L, \tag{27}$$

allowing ρ to be defined as [12]

$$\rho = \frac{\pi L_s}{E_i}, \tag{28}$$

thus relating the Lambertian BRDF to the reflectance by [12]

$$f_r = \frac{L_s}{E_i} = \frac{\rho}{\pi}. \tag{29}$$

Equation (29) defines such a material to have a perfectly diffuse BRDF, independent of illumination or observation geometry.

For monochromatic light incident on an idealized mirror surface, reflection behaves specularly and follows Snell's Law as previously defined in Equation (9). The angle of reflection equals the angle of incidence, thus the reflected radiance is highly directional and dependent on the orientation of the incident light. For surface only BRDF models, a perfectly flat surface would be perfectly specular which can be described with a delta function as:

$$f_r(\hat{\omega}_i, \hat{\omega}_s) = \rho\delta(\theta_i - \theta_s)\delta(\phi_i + \pi - \phi_s), \tag{30}$$

where ρ is the total hemispherical reflectance and the Dirac delta function defines the BRDF to be infinite at the location of mirrored reflection and 0 at all other observation locations.

In practice, materials are not accurately described by a purely diffuse nor purely specular model, but can be well characterized as having both diffuse and specular components as shown in Figure 4. These specular and diffuse contributions can come

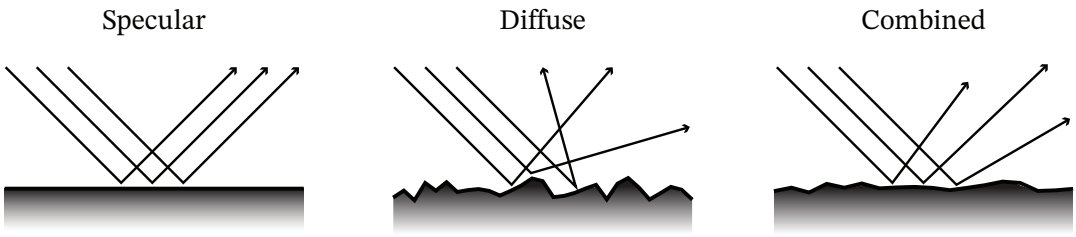

Figure 4. Specular and diffuse reflection are ideal theoretical descriptions of surface reflection. In practice, surface reflections tend to behave like a linear combination of the two.

from surface reflection or volumetric scatter within the surface. Volumetric scatter is often referred to as diffuse scatter while the directional surface reflection is modeled specularly. Together, a BRDF model can be described as:

$$f_r(\hat{\omega}_i, \hat{\omega}_s) = \rho_s S(\hat{\omega}_i, \hat{\omega}_s) + \rho_v V(\hat{\omega}_i, \hat{\omega}_s), \tag{31}$$

where ρ_s and ρ_v are surface and volumetric fitting parameters, S is the surface reflection function, and V is the volumetric scatter function. In the case of Lambertian volumetric scatter, $V = \frac{1}{\pi}$ as shown in Equation (29). Extending this approach, BRDF models may further separate the volumetric term into directional and Lambertian volumetric components leading to the universal BRDF form given as:[15]

$$f_r(\hat{\omega}_i, \hat{\omega}_s) = \rho_s S(\hat{\omega}_i, \hat{\omega}_s) + \rho_v V_d(\hat{\omega}_i, \hat{\omega}_s) + \frac{\rho_d}{\pi}, \tag{32}$$

where ρ_s is the surface fitting parameter, ρ_v is now the directional volumetric fitting parameter, V_d is the directional volumetric scatter function, and ρ_d is the diffuse fitting parameter following Lambertian scatter. The last two terms constitute the volumetric scatter.

Many BRDF models have been developed using this approach, attempting to

best describe the specular and diffuse radiance contributions upon reflection. One common model class is the microfacet model. These geometric optics based models are typically wavelength agnostic and depend on the surface structure of the material which is defined in the model as a distribution of small facets. The facets have a surface normal rotated with respect to the overall macrosurface normal as shown in Figure 5, where $\boldsymbol{\omega_h}$ is the spherical coordinate describing the difference between the

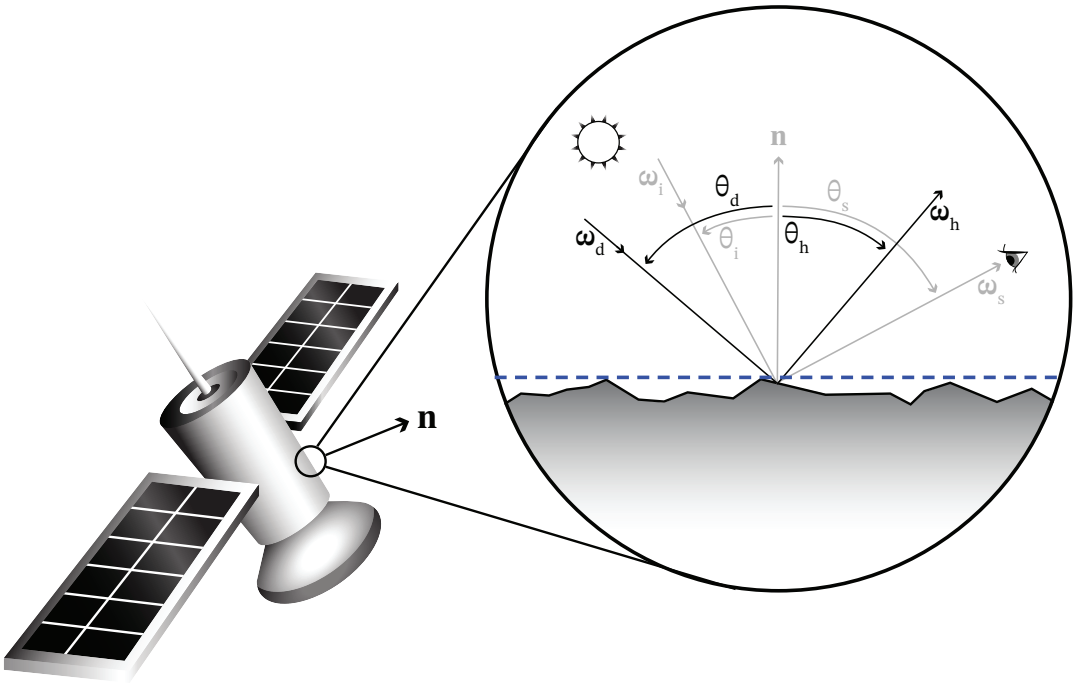

Figure 5. BRDF coordinates are presented in both macrosurface and microsurface geometry. Microsurface coordinates are rotated from the macrosurface normal (n) to model surface microfacet structure.

macrosurface normal and the microsurface normal. $\boldsymbol{\omega_d}$ is the rotated incident vector relative to the microsurface. For isotropic materials, there is symmetry about ϕ and θ is then defined as:[16]

$$\theta_d = \frac{1}{2}\cos^{-1}[\cos\theta_i \cos\theta_s + \sin\theta_i \sin\theta_s \cos(\phi_s - \phi_i)] \tag{33}$$

$$\theta_h = \cos^{-1}\left[\frac{\cos\theta_i + \cos\theta_s}{2\cos\theta_d}\right], \tag{34}$$

where θ_i and θ_s are the incident and scattered angles in the macrosurface normal orientation.

In general, microfacet models take the form:[15]

$$f_r(\hat{\omega}_i, \hat{\omega}_s) = \rho_s P(\hat{\omega}_i, \hat{\omega}_s) D(\hat{\omega}_h) F(\theta_d) G(\hat{\omega}_i, \hat{\omega}_s) \sigma(\theta_i, \theta_s) + \rho_v V_d(\hat{\omega}_i, \hat{\omega}_s) + \frac{\rho_d}{\pi}, \tag{35}$$

where the surface reflection function S from Equation (32) is the product of $P(\hat{\omega}_i, \hat{\omega}_s)$, a model specific prefactor accounting for terms not found in other models of similar form. $D(\hat{\omega}_h)$ is the microsurface normal distribution, $F(\theta_d)$ is the previously defined Fresnel reflection term from Equation (12), $G(\hat{\omega}_i, \hat{\omega}_s)$ is a geometric attenuation term, and $\sigma(\theta_i, \theta_s)$ is a cross section conversion term. Montes provides an overview of BRDF model in [17] and Butler provides a robust categorization of microfacet models in [15, 18].

The Cook-Torrance model is a particularly common microfacet BRDF model and takes the form as follows: [15, 8]

$$f_r(\hat{\omega}_i, \hat{\omega}_s) = 4\rho_s D_b(\theta_h) F(\theta_d) G_c(\hat{\omega}_i, \hat{\omega}_s) \sigma(\theta_i, \theta_s) + \frac{\rho_d}{\pi} \tag{36}$$

Referencing Equation (35), prefactor P is equal to 4 in the Cook-Torrance model and acts as a normalization factor of the cross section conversion term defined as:

$$\sigma(\theta_i, \theta_s) = \frac{1}{4cos\theta_i \cos\theta_s}, \tag{37}$$

which converts reflection from spherical scatterers to reflection off flat microfacet surface scatterers. The included factor of 1/4 defines the cross section conversion term found in many other microfacet models. This converts the surface scatter from

spherical scatter, common in physics, to planar scatter more representative of a typical interface. $D_b(\hat{\theta_h})$ is the Beckmann Gaussian distribution function with the following form:

$$D_b(\hat{\theta_h}) = \frac{1}{\pi m^2 \cos^4 \theta_h} exp\left[-\left(\frac{\tan \theta_h}{m}\right)^2\right], \tag{38}$$

where m is the surface roughness parameter of the distribution and θ_h is the scattered angle rotated in the microfacet normal geometry depicted in Figure 5. $F(\theta_d)$ is the unpolarized Fresnel reflection term from Equation (12) and $G_c(\hat{\omega_i}, \hat{\omega_s})$ is the Blinn geometric function [19] commonly known for its use in the Cook-Torrance model given as:

$$G_c(\hat{\omega_i}, \hat{\omega_s}) = \min\left[1, \left(\frac{2\cos\theta_h \cos\theta_s}{\cos\theta_d}\right), \left(\frac{2\cos\theta_h \cos\theta_i}{\cos\theta_d}\right)\right], \tag{39}$$

where the first term assumes a perfectly specular flat surface where no geometric attenuation occurs. The second term occurs for surfaces displaying obscuration, meaning the microfacet's angle of reflection is large with respect to the macrosurface normal. The third term describes surfaces displaying shadowing, meaning geometric attenuation occurs due to shadowing from microfacets at large angles with respect to the macrosurface normal.

Cook-Torrance, like many other microfacet models, does not include a directional volumetric scatter term ($\rho_v = 0$). The specular contribution from volumetric scatter has often been neglected as further research of appropriate volume scatter functions was required [15]. The following section describes existing BRDF models that consider volumetric scatter. Emphasis is placed on those including directional volumetric scatter.

2.6 Volumetric BRDF Models

BRDF models are categorized as theoretrical, semi-empirical, empirical, and experimental. Theoretical and semi-empirical categorization is often used synonymously; however, the distinction is clearly defined in studies comparing physical optics models and physically inspired models. Microfacet models are a BRDF subclass based on geometric ray optics theory thus are often considered physically-based theoretical models. Diffraction and other wave optics considerations are neglected by microfacet models, thus this subclass is not purely physical for all surfaces but is an approximation. Empirical models are developed to best fit observation trends and are not derived from first principles. Experimental models are those requiring prior measurement to characterize fit parameters for a specific surface type. Such models can be adaptive with each successive measurement and may or may not be physically based; accordingly, the experimental categorization does not specify if a model is theoretical or empirical.

This work has identified a subclass that models directional volumetric scatter either through a theoretical microfacet based approach or empirically. Remote sensing models are used in vegetation resource monitoring, atmospheric correction, and coated material characterization for signature prediction. Computer graphics models are developed to allow a particular effect in 3D rendering of visual effects. These can be physically-based for life-like realism or non-physical allowing a wide range of creative freedom. A description of each model and its directional volumetric term is included in the following section.

2.6.1 Roujean.

The Roujean model [20] takes a two part semi-empirical approach in developing a BRDF. It utilizes radiative transfer based volume scattering kernels. Roujean

describes a geometric term that includes a Lambertian scatter term and a specular surface term. Additionally, the model includes a microfacet based volume scatter term. Originally developed for remote sensing applications, particularly for investigation of earth resource monitoring of forests, grass fields, and plowed soil, Roujean notes that several other models assume surfaces to be homogeneous and require five or more surface parameters whereas this model affords higher computational efficiency having only three adjustable parameters.

A characteristic of soil and canopies is a strong backscattering signature modeled in the microfacet structure. Using a random distribution of protruding vertical reflectors on a surface, one can entertain that reflectance decreases as the observer moves away from the direction of incident light. This is true when one assumes the shadowing area within the field of view increases as the observer moves away from the incident light direction, and secondly, assuming a greater number of facets having normals that deviate from the incident light are observed. The second causes reduced irradiance on the facet and a decreased reflectance in the surface model. [20] The model highlights the significance of volumetric effects on reflectance and assumes a single bounce approximation to determine the emerging radiation scattered by a single microfacet and has not been otherwise obstructed by interaction with additional facets. The volume reflectance increases as the observer approaches grazing, near parallel to the macrosurface. Here the directional volumetric contributions of lower layers are shadowed by the upper layers when observed normal to the macrosurface. As the observer tends towards grazing, shadowing decreases and a greater proportion of the subsurface is accessible to the observer. This is shown in Figure 6, and is the basis for the components of the Roujean model. The final BRDF model takes a form similar to that of Equation (32) and is given as:[20]

$$f_r(\theta_i, \theta_s, \phi) = k_0 + k_1 f_1(\theta_i, \theta_s, \phi) + k_2 f_2(\theta_i, \theta_s, \phi), \tag{40}$$

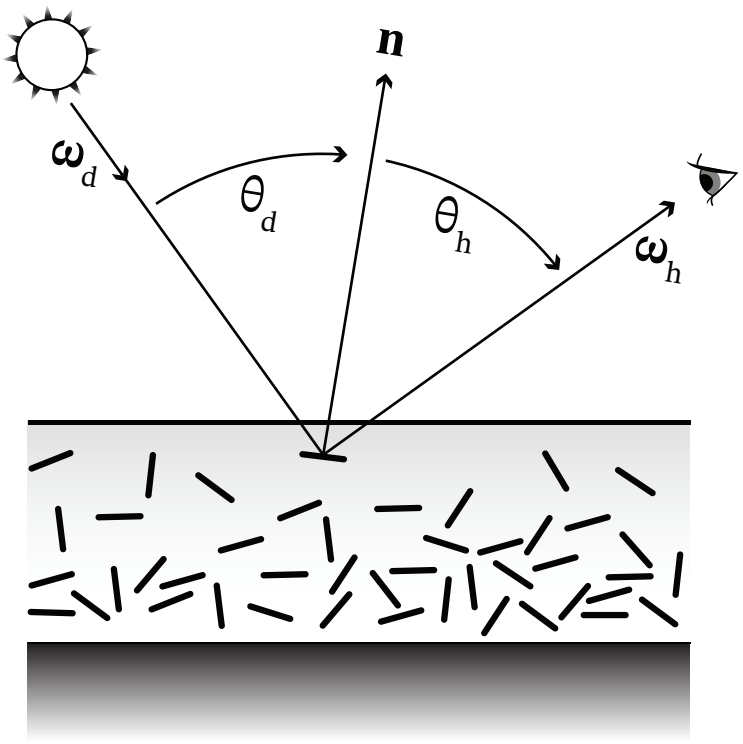

Figure 6. Subsurface scatter is approximated in microsurface coordinates according to single bounce scatter off randomly distributed microfacets.

where k_0 is the Lambertian diffuse scatter term. k_0, k_1, and k_2 are fit parameters to uniquely classify cover types. Roujean identifies k_0 as a geometric diffuse term; however from the perspective of volume scatter, one may consider k_0 as the Lambertian volumetric term as previously described, and $k_2 f_2(\theta_i, \theta_s, \phi)$ as the directional volume term where f_2 is an analytical function of the incident solar and viewing angles described by:

$$f_2(\theta_i, \theta_s, \phi) = \frac{4}{3\pi}\left(\frac{1}{\cos\theta_i + \cos\theta_s}\right)\left[\left(\frac{\pi}{2} - 2\theta_d\right)\cos 2\theta_d + \sin 2\theta_d\right] - \frac{1}{3}. \tag{41}$$

$k_1 f_1$ is thus the surface scatter term given as:

$$\begin{aligned} f_1(\theta_i, \theta_s, \phi) =& \frac{1}{2\pi}[(\pi - \phi)\cos\phi + \sin\phi]\tan\theta_i \tan\theta_s \\ & - \frac{1}{\pi}\left(\tan\theta_i + \tan\theta_s + \sqrt{\tan\theta_i^2 + \tan\theta_s^2 - 2\tan\theta_i \tan\theta_s \cos\phi}\right), \end{aligned} \tag{42}$$

where f_1 is derived from analysis of the vertical facets of random azimuthal orientation with the addition of shadowing effects.

Roujean defines the observation angle θ_s to range from 0 to $\frac{\pi}{2}$, restricting f_1 from vanishing as would occur if θ_s is allowed to be negative. Roujean therefore defines $\phi = 0$ to be backscatter and $\phi = \pi$ as forward scatter when in the principle plane. Figure 7 replicates Roujean's results for the surface and directional volumetric functions. A strength of this model is its ability to capture strong backscatter results at large observation angles.

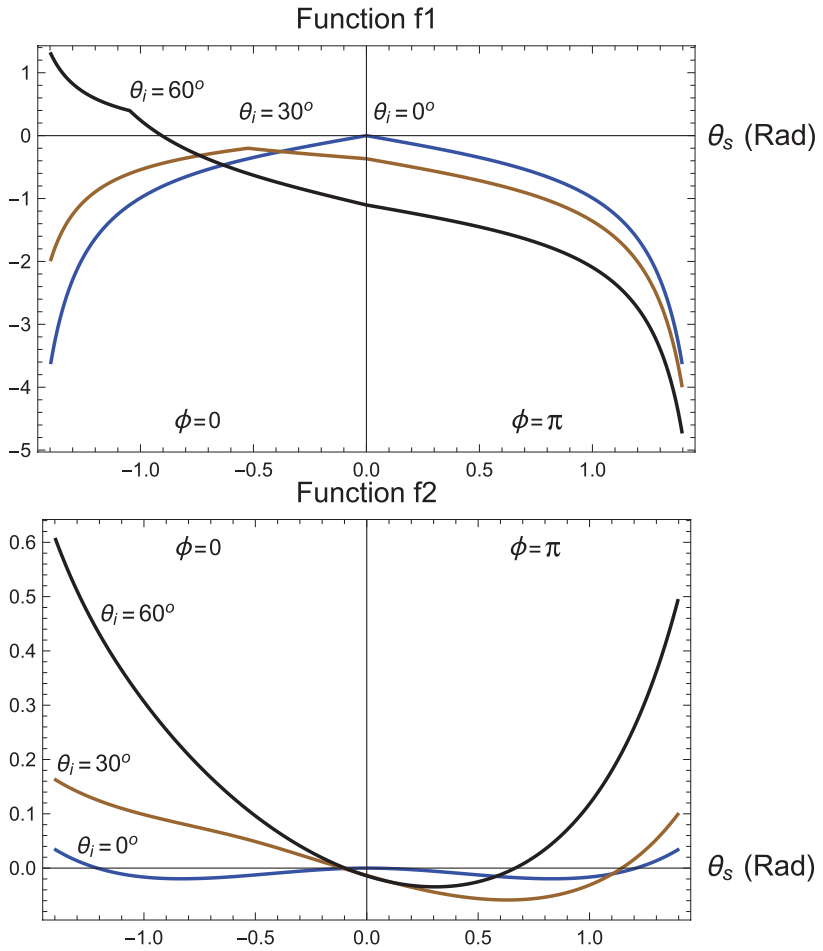

Figure 7. Plots duplicating Roujeans f_1 and f_2 functions which describe the specular surface and directional volume terms respectively. A strong backscatter result occurs in both functions at large observation angles. θ_s is shown negative for backscatter to agree with Roujeans original work; however, computationally θ_s is strictly positive and ϕ is piece-wise as indicated.

2.6.2 Modified Beard-Maxwell.

Originally developed for infrared signature prediction of painted surfaces in 1973, the Beard-Maxwell model[9] laid the foundation for the more commonly used modified Beard-Maxwell model. It follows the generalized microfacet form shown in Equation (35) given by Butler [15] and is given as: [21]

$$f_r(\hat{\omega_i}, \hat{\omega_s}) = \rho_s D_{bm}(\theta_h) F(\theta_d) G_{bm}(\theta_h, \theta_d) \sigma(\theta_i, \theta_s) + \rho_v V_{bm}(\theta_i, \theta_s) + \rho_d, \qquad (43)$$

where the model contains a simple unpolarized directional volumetric term $V_{bm}(\theta_i, \theta_s)$ by: [21]

$$V_{bm}(\theta_i, \theta_s) = \frac{2}{cos\theta_i + cos\theta_s}, \tag{44}$$

and a Lambertian reflectance term ρ_d. ρ_d is referenced as first surface diffuse scatter not volumetric Lambertian scatter.

V_{bm} assumes an exponential scattering function for incident radiation on a volume modeled by infinite layered subsurfaces of finite thickness. Volume scatter at a detector is derived by assuming power loss throughout incident and reflected path travel. Reflected light is scattered off a sublayer at a given distance below the surface toward the receiver. Sublayers are given to be flat thus follow the law of reflection for forward scatter. Absorption is ignored within the volume. Additionally, the volume term assumes zero transmission through the volume, essentially modeling an infinite thickness. The original directional volume term included empirically fit terms f and g in the numerator to account for finite thickness and specular reflectance off the bottom layer. The modified model is often shown without these as they can be accounted for in ρ_v. A full derivation can be seen in the original paper from 1973 [9].

Aside from the cross section conversion, $\sigma(\theta_i, \theta_s)$ given by Equation (37), the surface term is calculated in microsurface coordinates, θ_h and θ_d. The modified Beard-Maxwell model has a geometric function given by:

$$G_{bm}(\theta_h, \theta_d) = \frac{1 + \frac{\theta_h}{\Omega} e^{-2\theta_d/\tau}}{1 + \frac{\theta_h}{\Omega}}, \tag{45}$$

where Ω and τ are surface fitting parameters. A modified Cauchy distribution given by:

$$D_{bm}(\theta_h) = \frac{\beta}{(\cos\theta_h)(s^2 + \tan^2\theta_h)}, \tag{46}$$

defines the microfacet distribution commonly used in one version of the modified

Beard-Maxwell model. This distribution is an estimation based on bi-static surface measurements and is modified from the Cauchy function used in the original model. Here s broadens the microfacet distribution. The surface term also utilizes the familiar Fresnel term $F(\theta_d)$ given in Equation (12).[15]

2.6.3 Sandford-Robertson.

The Sandford-Robertson model is a microfacet model originally developed in 1985 for infrared signature prediction of aircraft paints.[10] Its original form is described with a specular and diffuse term; however, it has been shown an equivalent form exists that follows the generalized microfacet form and consists of a specular surface and volumetric term.[15] The model takes an approach to ensure energy is conserved upon reflection and that Kirchoff's law of radiation is upheld. The full model is given as: [15, 10]

$$\begin{aligned} f_r(\hat{\omega_i}, \hat{\omega_s}) &= f_s(\hat{\omega_i}, \hat{\omega_s}) + f_v(\theta_i, \theta_s) \\ &= \frac{N_e(\theta_i) D_e(\theta_h)}{4\pi \cos\theta_s} [1 - \rho_v F_s(\theta_i) - \varepsilon_0 F_s(\theta_i)] + \rho_v V_s(\theta_i, \theta_s), \end{aligned} \tag{47}$$

where ε_0 is the average emittance over the observation hemisphere and $N_e(\theta_i)$ is a normalization function for the elliptical microfacet distribution $D_e(\theta_h)$ which are given by: [10, 15]

$$N_e(\theta_i) = \frac{2c^2}{(1-c^2)\cos\theta_i + \frac{2c^2 + (1-c^2)^2 \cos^2\theta_i}{\sqrt{(1-c^2)^2 \cos^2\theta_i + 4c^2}}} \tag{48}$$

$$D_e(\theta_h) = \frac{1}{c^2 \cos^2\theta_h + \sin^2\theta_h}. \tag{49}$$

Model parameter c defines the width of the specular lobe. The microfacet distribution itself is not normalized and is calculated microsurface coordinates. The normalization term scales the distribution function such that the prefactor shown in Equation (35)

can be given as: [15, 10]

$$P(\hat{\omega_i}, \hat{\omega_s}) = \frac{N_e(\theta_i)}{4\pi cos\theta_s}[1 - \rho_v F_s(\theta_i) - \epsilon_0 F_s(\theta_i)]. \tag{50}$$

The term in brackets is responsible for maintaining conservation of energy and acts as an effective geometric term for the model. Sandford-Robertson also uses a modified Fresnel reflection term given by:[10, 15]

$$F_s(\theta) = \left[\frac{1}{1 + b^2 \tan\theta}\right] \left[\frac{(1-b)^2(1+b)}{1 - b^2 + 2b^2 ln(b)}\right], \tag{51}$$

where b is the model parameter describing the emittance behavior near grazing and θ is given without a subscript as it may be the incident or scattered angle specified, depending on the location within the model.

The Sandford-Robertson directional volumetric term derives from a directional emissivity model and takes the form similar to that of a directional diffuse term based on Fresnel reflections as opposed to a volumetric scatter description seen in other models. The diffuse volumetric term is the product of the incident energy that is diffusely scattered hemispherically using the approximated Fresnel term and the angular distribution of the scatter energy. The volumetric term is given as:[15, 10]

$$V_s(\theta_i, \theta_s) = \frac{F_s(\theta_i) F_s(\theta_s)}{\pi}. \tag{52}$$

2.6.4 Modified Walthall.

The Modified Walthall is a widely used kernel based empirical BRDF model developed to approximate the bidirectional reflectance from vegetative canopies and bare soil surfaces. Observations of such surfaces showed reflectance increases with increasing observation angle toward grazing. Peak reflectance typically occurs when

observations are in-plane. Additionally, when observing near grazing, reflectance increases with increasing incident angles. This model empirically describes these three observations in its original form given by:[22, 23]

$$f_r(\hat{\omega_i}, \hat{\omega_s}) = A\theta_s^2 + B\theta_s \cos(\theta_s - \theta_i) + C, \tag{53}$$

where θ_s is the observation angle defined from zenith at observation azimuth ϕ_s. Coefficients A, B, and C are typically a function of incident angle θ_i and are fit parameters from data observations using a linear least squares fit. later, Nilson and Kusk [24] improved on the original model[25] by considering scatter terms for the bottom soil layer, the canopy layer, and multiple scatter effects within the canopy as a function of wavelength. The model is given as: [24]

$$f_r(\hat{\omega_i}, \hat{\omega_s}, \lambda) = a_0(\theta_s^2 + \theta_i^2) + a_1\theta_i^2\theta_s^2 + a_2\theta_i\theta_s \cos(\phi_s - \phi_i) + a_3, \tag{54}$$

where $a_0 - a_3$ are wavelength specific fit parameters determined experimentally.

While this model does not have physical surface and volumetric terms, it follows a similar linear combination of weighted terms as shown in other theoretical models. Additionally, the third term $a_2\theta_i\theta_s cos(\phi_s - \phi_i)$ provides a linear dependence on incident and observation angle to interact with the quadratic terms while the ϕ dependency forces reflectance to decrease as observation azimuth deviates from direct backscatter. This forces a strong backscatter signal that is characteristic of volumetric scatter; thus, this model is a good candidate for comparison.

2.6.5 Schlick.

Schlick developed a multilayer semi-empirical microfacet model in 1993 intended for realistic graphics rendering. The model sought to maintain conservation of energy,

obey Fresnel principles, be experimentally adaptable, and provide a description for isotropic and anisotropic materials. [26]. The original paper describes two models, a surface layer model intended for materials with homogeneous optical properties and a double layer model to describe heterogenous materials. Here the focus is on the two layer model where the top layer is used for specular surface reflection while the bottom layer is for subsurface scatter. The top layer is not perfectly opaque so a portion of the energy is specularly reflected by the top layer while the rest is incident on the second layer, all of which is diffusely scattered by a perfectly opaque bottom layer. Each layer is defined by the following properties:

- $R_0 \in [0,1]$: Reflection factor at a given wavelength
- $r \in [0,1]$: Roughness factor (0: perfectly specular, 1: perfectly Lambertian)
- $P \in [0,1]$: Isotropy factor (0: perfectly anisotropic, 1: perfectly isotropic)

The full model is the sum of two single layer models weighted by a specularity scale factor describing the transmittance of the top layer and is given by:[26, 27]

$$f_r(\hat{\omega_i}, \hat{\omega_s}) = F_s(\theta_d)\sigma(\theta_i, \theta_s)D(\hat{\omega_i}, \hat{\omega_s}) + [1 - F_s(\theta_d)]F_s'(\theta_d)\sigma'(\theta_i, \theta_s)D'(\hat{\omega_i}, \hat{\omega_s}) \quad (55)$$

where the prime notation differentiates between the first and second layer. $F_s(\theta_d)$ is Schlick's approximation of the Fresnel term given as:[15, 26, 27]

$$F_s(\theta_d) = R_0 + (1 - R_0)(1 - \cos\theta_d)^5 \quad (56)$$

and $D(\hat{\omega_i}, \hat{\omega_s})$ is a distribution function defining the directional dependence of the BRDF about the observation hemisphere. The dependence on zenith and azimuthal

angle is expressed in the directional factor as:

$$D(\hat{\omega_i}, \hat{\omega_s}) = \frac{Z(\theta_h)A(\phi)}{\pi}, \tag{57}$$

where $Z(\theta_h)$ models the anisotropy of the surface with an angular dependence from zenith given by:

$$Z(\theta_h) = \frac{r}{(1 + r(\cos\theta_h)^2 - (\cos\theta_h)^2)^2}. \tag{58}$$

Here θ_h represents the angular difference between the macrosurface and the microfacet normal as previously defined. $A(\phi)$ is responsible for azimuthal anisotropy and is given by:

$$A(\phi) = \sqrt{\frac{P}{P^2 - P^2(\cos\phi)^2 + (\cos\phi)^2}}, \tag{59}$$

where $\phi = \phi_s - \phi_i = \phi_s$ when $\phi_i = 0$. The familiar cross section conversion term $\sigma(\theta_i, \theta_s)$ is included as shown in Equation (37).

The volumetric term is provided by the second set of terms in Equation (55). Directional volumetric scatter is treated again as surface scatter off the sublayer material which is defined uniquely from the top layer. The Schlick model does not have separate Lambertian and directional diffuse terms; however, for a perfectly isotropic sublayer when $A = 1$ and $r = 1$, the directional factor appears Lambertian only to be scaled by the angular dependence of Schlick's approximated Fresnel term. Together, this model provides an efficient physically based microfacet approximation for realistic rendering and includes an alternative description for directional volumetric scatter.

2.6.6 Oren-Nayar.

The Oren-Nayar model [28] is based on a generalization of the Lambertian model, extended to approximate surface and volumetric diffuse scatter using a microfacet surface description. V-cavities with single slope facets are used to model a Gaussian

slope area distribution with a standard deviation and roughness parameter σ which ranges from 0 to 1. The full model is given by:[28]

$$
\begin{aligned}
f_r(\hat{\omega_i}, \hat{\omega_s}) &= \frac{\rho}{\pi}(A + B \max([0, \cos(\phi_s - \phi_i)] \sin(\alpha) \tan(\beta)) \\
A &= 1 - 0.5\frac{\sigma^2}{\sigma^2 + 0.33} \\
B &= 0.45\frac{\sigma^2}{\sigma^2 + 0.09},
\end{aligned}
\tag{60}
$$

where $\alpha = \max(\theta_i, \theta_s)$ and $\beta = \min(\theta_i, \theta_s)$. A and B are coefficients derived from the source illumination surface radiance computation.

Originally a qualitative model for diffuse reflection, Oren-Nayar provides a simple solution for diffuse rough surface graphics rendering. This pseudo-directional diffuse description accounts for appearance differences of matte materials that tend to display non-Lambertian scatter. Volumetrically, this model provides a directional volume and a Lambertian term. It is considered a semi-empirical model as it describes Lambertian scatter in its limiting case $\sigma = 0$ and accounts for geometric factors such as shadowing and masking.[28] Additionally, the model is accepting of ρ, the surface albedo of the material, as a function of wavelength despite its geometric origins. Backscatter strength increases with larger σ values. Oren-Nayar found dirtier materials tended to retro-reflect light more than clean smooth materials, possibly due to the macroscopic structure allowing for increased volume scatter.

2.6.7 Kubelka-Munk.

Propagation of light is well described within layered surfaces as long as the layers are homogeneous and simplifications are assumed so the boundary connecting each layer is smooth [29]. In practice, multi-layer media is better described as inhomogeneous and rough at the interface. Analytical models exist for light transporting within a volume, but are computationally complex. To describe this efficiently, transport the-

ory is often used wherein light propagates through the media by serial absorption and scatter. This type of transport model is less computationally expensive and describes volumetric scatter using only two parameters [30]. The Kubelka-Munk (K-M) theory is a commonly used transport model developed in 1931 [31] to describe diffuse absorption and partial scatter within paint layers. The theory has since been widely adopted by printing, textile, and paper industries wherein observed color output from scatter of multiple ink layers is desired [30]. Recently K-M models have been used to examine human tissue layers and scatter within leafy canopies [32].

Kubelka and Munk established the original two flux radiative transfer model by assuming the component of light emerging from a layered substrate is based on two light channels, forward and backward scatter within the volume. Each are characterized by absorption and scatter coefficients of the material. The model originally described scatter within the volume of the media, but did not address boundary interaction at the top and bottom of the layer [31]. In 1942, Saunderson extended the model accounting for boundary interactions. [30, 33]

Like the original K-M theory, Saunderson's correction assumes diffuse incident light and diffuse light within the volume. In 2006, Murphy [29] described an extension to the Saunderson correction for collimated light on optically rough surfaces. This extension shows K-M theory is a good approximation for collimated incident light as well as diffuse incident light. Figure 8 shows the geometry described by Murphy[29] for collimated light incident on a coating with an opaque substrate.

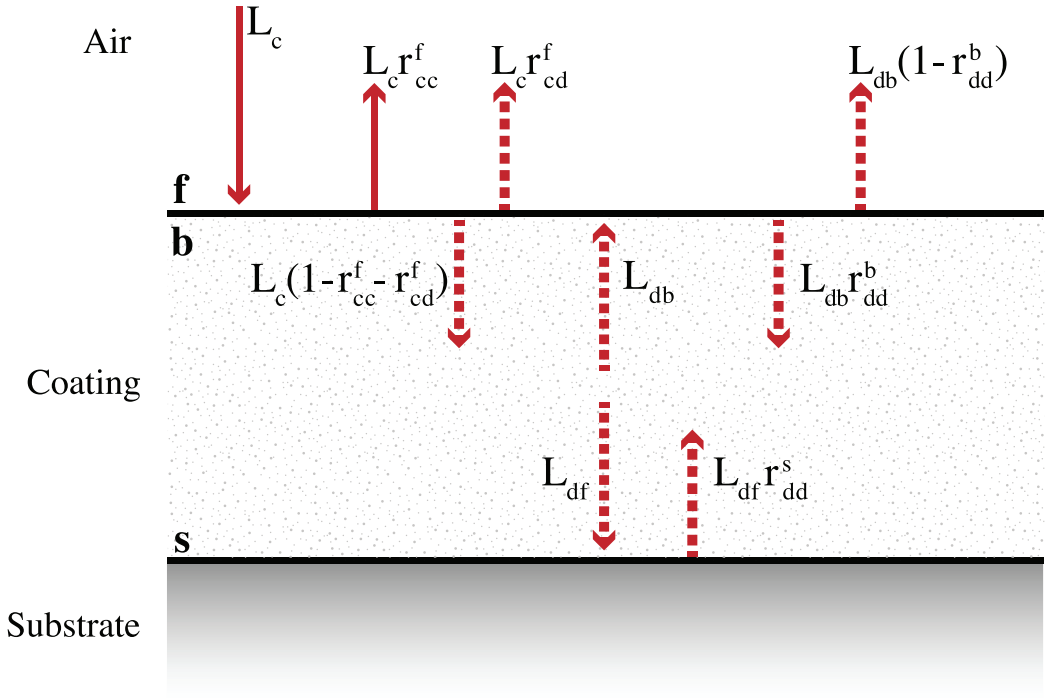

Figure 8. Geometry of incident collimated (solid arrow) light and resulting diffuse (dashed arrow) transport at coating interfaces.

Collimated light is indicated by solid lines while diffuse light is dashed. r^i_{cc} is the reflection coefficient for collimated light reflected speculary. r^i_{cd} is the reflection coefficient for collimated light reflected diffusely. r^i_{dd} is the reflection coefficient for diffuse light reflected diffusely. The superscript i on the coefficient indicates the surface in reference. f is for reflection at the front of the coating, b is for reflection at the back of the coating, and s is reflection at the substrate [29].

Collimated incident light (L_c) interacts at the air-coating interface. Light entering the volume is assumed to be diffuse. This is consistent for a sufficiently rough surface. Light within the volume is scaled by the reflection coefficient for collimated light reflected specularly at the top surface (r^f_{cc}) and the reflection coefficient for collimated light reflected diffusely (r^f_{cd}) at the surface. The resulting diffuse light follows absorption and scatter transport theory as forward and backward directed diffuse light, L_{df}

and L_{db} respectively. L_{df} is scaled by the reflection coefficient at the coating-substrate interface (r^s_{dd}). Backward scattered light is scaled by the reflection at the backside of the coating-air interface (r^b_{dd}) yielding the diffuse volumetric component that is transmitted back through the top surface [29].

Neglecting specular reflection from the surface, the resulting diffuse reflectance from the coating-substrate system is the sum of the diffusely reflected component of collimated light at the top surface and the component of volumetric scatter directed back toward the top surface. Combined, the total diffuse reflectance for collimated light on a coating is given as: [29]

$$R_{cd} = r^f_{cd} + \frac{(1 - r^f_{cd} - r^f_{cc})(1 - r^b_{dd})R_{km}}{1 - r^b_{dd}R_{km}}, \tag{61}$$

where R_{km} is the diffuse reflectance of the coating volume based on the absorption and scatter coefficients. R_{km} is a parameter of the modified K-M model.

Murphy notes the derivation of Equation (61) is consistent with Saunderson's approximation for diffuse illumination where the reflectance reduces to: [29, 33]

$$R_{dd} = r^f_{dd} + \frac{(1 - r^f_{dd})(1 - r^b_{dd})R_{km}}{1 - r^b_{dd}R_{km}}. \tag{62}$$

Diffuse incident light eliminates the need for collimated reflection coefficients in Equation (61) and scales the incident diffuse light by the reflection coefficient for diffuse light reflected as diffuse light. [29, 33].

Murphy's modified Kubelka-Munk model proved valid for collimated and diffuse incident light on optically rough surfaces. In 2019, Yang et al. [2] presented a modified microfacet BDRF model based on the modified Kubelka-Munk volumetric theory. Consistent with other microfacet models, Yang presented a linear combination of specular and diffuse scatter descriptions. The resulting BRDF model is the sum of

the two components given as:[2]

$$f_{ry}(\hat{\omega_i}, \hat{\omega_s}) = k_s S_y(\hat{\omega_i}, \hat{\omega_s}) + k_v V_y(\hat{\omega_i}, \hat{\omega_s}). \tag{63}$$

This form, converted from Yang for consistency, is equivalent to the generalized BRDF form [15] from Equation (31). k_s and k_v are surface and volumetric fitting parameters, S_y is the surface reflection function and V_y is the volumetric scatter function. The surface component is based on Torrance-Sparrow microfacet reflection given as: [2]

$$S_y(\hat{\omega_i}, \hat{\omega_s}) = \sigma(\theta_i, \theta_s) D_g(\theta_h) G_c(\hat{\omega_i}, \hat{\omega_s}), \tag{64}$$

where $\sigma(\theta_i, \theta_s)$ is the cross-section conversion for the microfacet surface described previously by Equation (37). $G_c(\hat{\omega_i}, \hat{\omega_s})$, given previously by Equation (39), is the Blinn geometric function. Known largely for its use in the Cook-Torrance model, $G_c(\hat{\omega_i}, \hat{\omega_s})$ is a simplification of the geometric function given by Torrance-Sparrow. $D_g(\theta_h)$ is a modified version of the Beckmann-Gaussian distribution given by Equation (38), where $m = \sigma\sqrt{2}$ and σ is the surface roughness parameter.

Note S_y does not include a Fresnel reflectance term to account for polarization effects at the boundary. This effect varies based on the index of refraction difference at the surface boundary as well as polarization orientation of the incident light. Including Fresnel reflectance is valid for both polarized and unpolarized light as unpolarized light can be described by a combination of polarized components. The generalized microfacet form given in Equation (35) further describes the inclusion of Fresnel reflectance in microfacet models.

Volume scatter $V_y(\hat{\omega_i}, \hat{\omega_s})$ given as: [2]

$$V_y(\hat{\omega_i}, \hat{\omega_s}) = \frac{\cos\theta_s}{\pi} \frac{(1 - F_{fb}(\theta))(1 - F_{bf}(\theta))R_\infty}{1 - F_{bf}(\theta)R_\infty}, \tag{65}$$

is a simplified form of Equation (62). The reflection coefficients are described using Fresnel reflectance $F(\theta)$ with complex indices of refraction as given in Equation (12). Subscripts fb and bf indicate Fresnel reflectance from air-to-coating and from coating-to-air, respectively. R_∞ is the diffuse reflectance parameter assuming a coating of infinite thickness. The diffuse volume term from Equation (62) has been converted from unitless reflectance to BRDF units by the $\cos\theta_s/pi$ term. This hemispherical conversion transforms reflectance to BRDF accounting for the angular distribution of the volume scatter at the observer.

While Yang investigated Kubelka-Munk volume scatter in a modified microfacet model, Murphy and Saunderson show in their derivations and equations (61) and (62) that a constant (Lambertian) surface scatter term should be included in addition to the directional diffuse volume term for a complete diffuse description. Accordingly, the Yang model would benefit from this extension. [29, 33] The resulting improvements to the Torrance-Sparrow surface description by Yang established Kubelka-Munk theory as a promising extension to generalized microfacet BRDF theory.

This chapter built on foundational electromagnetic theory to describe surface scatter principles, reflection theory, and non-resonant scatter mechanisms to introduce the Radiometric model. From this, BRDF principles and the rendering equation were shown to be key in determining the apparent signal at an observer. The microfacet class of models was introduced and the significance of directional volume scatter was highlighted. Finally, seven directional volume scatter models were presented for analysis throughout this thesis. Chapter 3 describes the methodology for comparing directional volume models with high fidelity, low density BRDF measurements.

III. Methodology

The methodology taken to determine the significance of directional volumetric terms in BRDF modeling performance was accomplished in three parts. First, BRDF measurements of nine samples were collected using a scatterometer with interchangeable illumination sources at LWIR, MWIR, NIR, UV, and visible wavelengths. Data collection was performed at the Optical Measurements Facility (OMF) of the Air Force Research Laboratory, Materials and Manufacturing Directorate in Wright Patterson Air Force Base, Ohio. In total, 15 datasets were studied, each at multiple incident illumination configurations and some at multiple illumination wavelengths. The samples are paints uniquely categorized as a diffuse surface, specular surface, or National Institute of Standards and Timing (NIST) Standard. Further discussion of the sample set is provided in the following sections.

Next, six hybrid BRDF models were developed using the Cook-Torrance model and independent directional volume scatter terms. The first model is the standard Cook-Torrance model. The second model adds a semi-empirically derived directional volume term to the Cook-Torrance model. Models 3 through 7 utilize the Cook-Torrance model while including Kubelka-Munk, Modified Beard-Maxwell, Sandford-Robertson, Oren-Nayar, and Roujean directional volume terms respectively.

Finally, a recursive relative global minima fitting routine written in MATLAB® determines an independent best fit to each of the models for each sample. This script identifies local best-fit solutions within each model's parameter space and extracts the relative global best fit solution of each sample. The square of the Mean standard error (MSE^2) is determined over the full observation ranges as well as in truncated sub-regions contributing of the full model. This method demonstrates model accuracy, highlights model performance regions, and allows comparison of each directional volume model.

3.1 Measurement and Samples

Measuring BRDF requires careful consideration and precision equipment. Reflectance is often thought of in terms of a unitless value between 0 and 1, also known as the Hemispherical-Directional Reflectance (HDR). This is an integrated value over the incident hemisphere and provides little directionally specific reflectance information. BRDF profiles are desired for non-Lambertian materials. In the case of some materials, like glossy (specular) paints, the signal just outside of the forward specular lobe can vary by several orders of magnitude. Accordingly, a chopper wheel and lock-in amplifier system is used in conjunction with the illumination source. The illumination source is periodically blocked, allowing observation and correction of the self-emission component observed at the detector. The lock-in amplifier boots the signal according to observation configuration, allowing BRDF characterization over multiple orders of magnitude.

Figure 9 shows the basic setup of a CASI® BRDF measurement system. The custom scatterometer at the OMF operates similarly. The sample is placed at the center of the system and the illumination source, an interchangeable laser, is propagated through a series of mirrors (M), chopper wheel (Ch), focusing lens (FL), pinhole (PH) to clean up the light, and finally an off-axis parabolic mirror (OAP) before in-plane illumination of the sample. A detector placed on a Goniometer arm is allowed to span both in-plane and out of plane about the observation hemisphere. Incident illumination angle is adjusted by rotating the sample as shown. All measurements were in-plane such that $\phi = 0$ or $\phi = \pi$ exclusively.

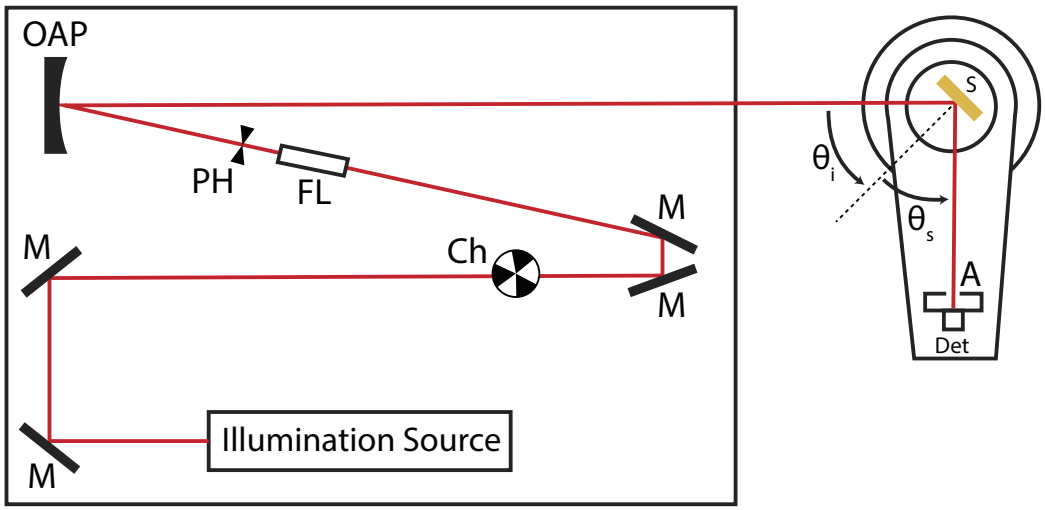

Figure 9. BRDF imaging system captures in-plane measurements using interchangeable illumination sources.

In total, 15 measurements of nine samples were made at incident angles ranging from $\theta_i = 0°$ to $\theta_i = 85°$. Five different illumination wavelengths provided spectral sampling at $0.325\mu m$, $0.6328\mu m$, $1.06\mu m$, $3.39\mu m$ and $10.6\mu m$. Not all samples were illuminated by all wavelengths. A total of 44 incident angles and illumination source combinations were investigated as summarized in Table 2.

Samples are mostly thick paint coatings with glossy (specular) or matte (diffuse) visual characteristics. Samples were chosen to exhibit scatter with a variety of volume scatter components. PNT65, PNT36375, and PNT36495 are visually diffuse and expected to exhibit a high volume scatter component. PNT01006 is visually specular and also anticipated to exhibit a high volume scatter component. PNT66 and PNT01014 are visually diffuse and specular, respectively and expected to exhibit a low volume scatter component. STD00696, STD00698, and STD00699 are all NIST diffuse infrared reflectance standards anticipated to have high surface scatter and low volume scatter components. STD00696 is gold on an arc-sprayed aluminum substrate, STD00698 is a flat black paint on brass, and STD00699 is a silver paint on arc-sprayed aluminum. The author would like to thank Joe Costantino of the Air Force Research

Material	Type	$0.325\mu m$	$0.6328\mu m$	$1.06\mu m$	$3.39\mu m$	$10.6\mu m$
PNT65	Diffuse	X_2	X_2	X_2	X_2	X_2
PNT66	Diffuse	X_2	-	X_2	X_2	-
PNT36375	Diffuse	-	-	X_4	-	-
PNT36495	Diffuse	-	X_{3a}	-	-	-
PNT01006	Specular	-	-	X_{3b}	-	-
PNT01014	Specular	-	-	X_{3b}	-	-
STD00696	NIST Std	-	-	-	X_5	-
STD00698	NIST Std	-	-	-	X_5	-
STD00699	NIST Std	-	-	-	X_5	-

Table 2. Summary of data investigated. X indicates measurements were made for the material at incident angles given by the subscript as 2: $\theta_i = [30, 60]$, 3_a: $\theta_i = [30, 60, 85]$, 3_b: $\theta_i = [20, 60, 75]$, 4: $\theta_i = [20, 40, 60, 8]$, and 5: $\theta_i = [0, 20, 40, 60, 80]$. Symbol (−) indicates no data collected.

Lab, Materials and Manufacturing Directorate for selecting and providing the BRDF data used in this work.

Observations were made to span the in-plane configuration where $\theta_s = \pm 85^\circ$ with some data sets extended further toward grazing at $\theta_s = \pm 89^\circ$. Due to geometric limitations of the scatterometer and the nature of the in-plane measurement, direct backscatter data is not available at $\theta_s = -\theta_i$. That is, for observations at $\phi = 0^\circ$, the illumination source is blocked by the detector in the $\theta_s = \pm 1.5^\circ$ region about $\theta_s = -\theta_i$. Analysis of BRDF model performance in the backscatter observation region is one of the contributions to the field outlined in this thesis.

3.2 Empirical Directional Volumetric Scatter Term Formulation

Model 1 is the Cook-Torrance model as described in Equation (36). This model is described as a surface model with the addition of a Lambertian scatter term. This thesis takes the position that the Lambertian term is one contributing component of the volumetric scatter with the other being a directional volumetric term not included in the Cook-Torrance model.

To best compare existing volumetrically inclusive terms, a two-lobe model was de-

veloped based on directional backscatter peaks observed in laboratory measurements. This semi-empirical volume term is included in the full Cook-Torrance model to form a modified Cook-Torrance model (model 2) and is used as a comparison against other established directional volume terms. The developed directional volume term in model 2 considers the standard Cook-Torrance specular and diffuse terms and adds an additional specular lobe flipped 180 degrees about ϕ to represent a retro-reflection term believed to be caused by volumetric scatter. The process to develop this term is described in detail below.

Beginning with the standard Cook-Torrance model, simulations were run assuming no volumetric term for a reference refractive index of gold, $n = 0.18377 + 3.4313i$, at $632.8nm$ [34]. The index of gold is well known and demonstrates proportionally desirable specular and diffuse behavior at visible wavelengths.

The standard Cook-Torrance model given by Equation (36) shows the forward propagated specular lobe is described by:[8]

$$f_s(\hat{\omega}_i, \hat{\omega}_s) = \rho_s \sigma(\theta_i, \theta_s) D_b(\theta_h) F(\theta_d) G_c(\hat{\omega}_i, \hat{\omega}_s) \tag{66}$$

where ρ_s is the specular prefactor, $\sigma(\theta_i, \theta_s)$ is the cross section conversion, $D_b(\theta_h)$ is the Beckmann microfacet distribution, $F(\theta_d)$ is the Fresnel reflection term, and $G_c(\hat{\omega}_i, \hat{\omega}_s)$ is the geometric attenuation term. This semi-empirical volumetric term assumes that subsurface scatterers are approximately spherical thus obey spherical scatter not planar microfacet surface scatter. Accordingly, the cross section conversion term is not needed in the development of this semi-empirical volumetric term as it was originally included as an approximate conversion from spherical scatter to planar scatter. Similarly, the geometric attenuation term corrects for shadowing and masking caused by the microfacet established with the cross section conversion, therefore G_c is not required in the volumetric baseline for model 2. Finally, the factor of four was

a normalization term on the cross section conversion, therefore is also not included. The result is

$$f_v(\hat{\omega}_i, \hat{\omega}_s) = \rho_s D_b(\theta_h) F(\theta_d) \tag{67}$$

where Equation (67) is a forward propagating simplified specular term. This is modified to produce the same lobe structure in the backscattered orientation. To do so, π phase offset is applied to θ_d. Recall θ_d and θ_h are the incident and scattered angles rotated for the microsurface normal given by Equation (33) and Equation (34). The modified θ_d becomes

$$\theta_{de} = \frac{1}{2}\cos^{-1}[\cos\theta_i \cos\theta_s + \sin\theta_i \sin\theta_s \cos(\phi - \pi)] \tag{68}$$

where $\phi = \phi_s = \phi_s - \phi_i$ when $\phi_i = 0$. θ_h becomes

$$\theta_{he} = \cos^{-1}\left[\frac{\cos\theta_i + \cos\theta_s}{2\cos\theta_{de}}\right] \tag{69}$$

where θ_{de} has a 180 degree offset about ϕ from θ_d for all incident angles. Carrying forward θ_{de} and θ_{he} into the Fresnel reflection term and the Beckmann distribution yields an empirical volumetric term that has results at $\phi = 0$ that are equivalent to that of Equation (67) when $\phi = \pi$. The semi-empirical directional volumetric term used in model 2 is then given by

$$f_{ve}(\hat{\omega}_i, \hat{\omega}_s) = \rho_v D_b(\theta_{he}) F(\theta_{de}) \tag{70}$$

and the results at $\phi = 0$ are equivalent to that of Equation (67) when $\phi = \pi$.

Figure 10 shows an in-plane plot of the simplified Cook-Torrance specular term, described by Equation (67), in forward scatter observation, that is $\phi = \pi$. The figure also shows an in-plane plot of the semi-empirical directional volumetric term,

described by Equation (70) in backscatter observation, that is $\phi = 0$. In both simulations, $\rho_s = \rho_v$ ensuring equal comparison of terms.

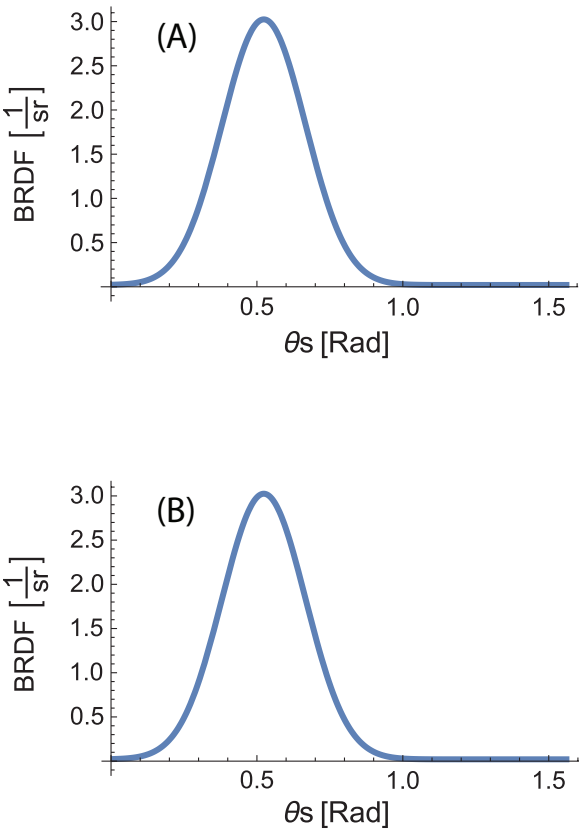

Figure 10. (A) Simplified Cook-Torrance forward scattered specular lobe observed in-plane at $\phi = \pi$ for $m = 0.1$, $\rho_v = 0.1$, and $\theta_i = 30°$. (B) Semi-empirical volumetric backscatter lobe observed in-plane with equivalent parameters at $\phi = 0$. Equivalence between plots verifies the directional volume term maintains characteristics of the simplified Cook-Torrance specular term, yet is observed in the backscatter region.

Matching results confirm that the semi-empirical directional volumetric term will yield a scalable backscatter lobe in-plane with the Cook-Torrance specular surface lobe. The term is then included in the original Cook-Torrance model, yielding an semi-empirical two specular lobe model, one of which is the volumetric backscatter lobe. Model 2 is thus given as:

$$f_{m2}(\hat{\omega}_i, \hat{\omega}_s) = \rho_s \sigma(\theta_i, \theta_s) D_b(\theta_h) F(\theta_d) G_c(\hat{\omega}_i, \hat{\omega}_s) + \frac{\rho_d}{\pi} + \rho_v D_b(\theta_{he}) F(\theta_{de}), \tag{71}$$

where the last term is the directional volume term given in Equation (70). Figure 11 shows a spherical plot of the full modified Cook-Torrance model simulating an incident angle of 30^o on gold with a microfacet surface slope of $m = 0.1$, $\rho_v = 0.1$, $\rho_s = 0.2$, and $\rho_d = 0.7$. The backscatter lobe is weaker than the forward propagated specular lobe which is consistent for small incident angles. Additionally, the diffuse Lambertian term dominates at large out of plane observations.

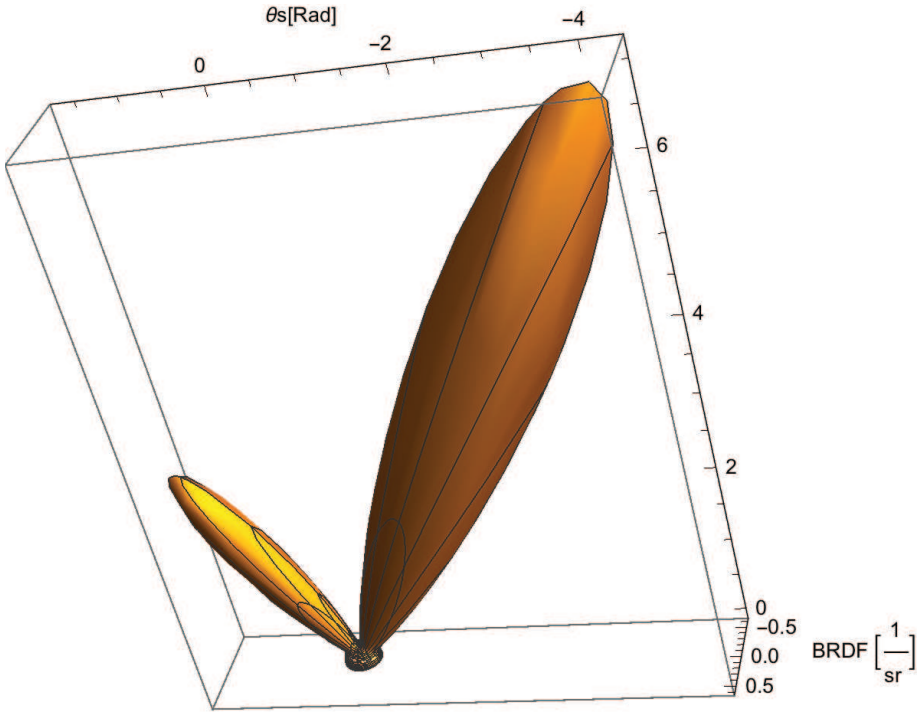

Figure 11. Spherical 3-D plot of model 2 simulating gold illuminated by 632.8nm light incident at 30 degrees. The added directional volume term models in-plane specular backscattered that is commonly observed to be weaker than the forward specular lobe.

3.3 Volumetric Model Comparison

Seven models were fit to the provided BRDF data. While additional directional volume terms were investigated throughout this study and were discussed in Chapter 2, the seven models presented make up the vetted list that appeared most promising to contribute to a better overall fit and improve backscatter performance. Schlick and

Modified Walthall models were found to be highly parameterized, each requiring nine and ten respective fit variables in the final hybrid model form. Additionally, Modified Walthall is a fully empirical model showing dominating Lambertian behavior that would already be captured by the diffuse scatter term in the Cook-Torrance model. Schlick, while directionally volumetric in nature, utilizes an approximated Fresnel term not entirely useful for this physics-based study since it is not easily generalized for future polarimetric studies.

Model 1 is the Cook-Torrance model given by Equation (36). The model includes a surface term, and Lambertian volume term. Model 2, given in the previous section by Equation (71), adds a semi-empirically derived directional volume term to the Cook-Torrance model. Each hybrid model 3 through 7 includes the Cook-Torrance surface term and Lambertian volume term, but differs by changing the directional volume term.

Model 3 utilizes the modified Kubelka-Munk directional volume term from Equation (65) where the coating is assumed to be thick:

$$\begin{aligned} f_{m3} =& 4\rho_s D_b(\theta_h) F(\theta_d) G_c(\hat{\omega_i}, \hat{\omega_s}) \sigma(\theta_i, \theta_s) + \frac{\rho_d}{\pi} \\ &+ \rho_v \frac{\cos\theta_s}{\pi} \frac{(1 - F_{fb}(\theta_i))(1 - F_{bf}(\theta_i))R_\infty}{1 - F_{bf}(\theta_i)R_\infty}. \end{aligned} \tag{72}$$

The model has seven parameters: ρ_s, ρ_d, ρ_v, m, n, k, and R_∞. Model 4 includes the Beard-Maxwell directional volume term given in Equation (44) and is given as:

$$f_{m4} = 4\rho_s D_b(\theta_h) F(\theta_d) G_c(\hat{\omega_i}, \hat{\omega_s}) \sigma(\theta_i, \theta_s) + \frac{\rho_d}{\pi} + \rho_v \frac{2}{\cos\theta_i + \cos\theta_s}. \tag{73}$$

Model 4 is similarly parameterized by ρ_s, ρ_d, ρ_v, m, n, and k. Model 5 includes the Sandford-Robertson directional volume term shown by Equation (52) and is given as:

$$f_{m5} = 4\rho_s D_b(\theta_h) F(\theta_d) G_c(\hat{\omega_i}, \hat{\omega_s}) \sigma(\theta_i, \theta_s) + \frac{\rho_d}{\pi} + \rho_v \frac{F_s(\theta_i) F_s(\theta_s)}{\pi}. \tag{74}$$

Model 5 includes Sandford's modified Fresnel function in the directional volume term, where b describes behavior near grazing. Accordingly, model 5 is parameterized by ρ_s, ρ_d, ρ_v, m, n, k, and b. The directional volume term describes Lambertian scatter in its limiting case, therefore is not always required for idealized diffuse scatterers. Model 6 includes the Oren-Nayar directional volume term given by Equation (60) as:

$$\begin{aligned} f_{m6} =& 4\rho_s D_b(\theta_h) F(\theta_d) G_c(\hat{\omega_i}, \hat{\omega_s}) \sigma(\theta_i, \theta_s) + \frac{\rho_d}{\pi} \\ &+ \frac{\rho_v}{\pi}(A + B \max([0, \cos(\phi_s - \phi_i)] \sin(\alpha) \tan(\beta)), \end{aligned} \tag{75}$$

where $\phi_i = 0$, A and B are functions of the roughness parameter σ, and α and β are functions of θ_i and θ_s. In this form, model 6 may be described by only five parameters. Oren-Nayar describes Lambertian scatter in its limiting case when $\sigma = 0$, therefore does not always require ρ_v or σ. When directional volume scatter and Lambertian scatter is present, the model is described by ρ_s, ρ_d, ρ_v, m, n, k, and σ.

Model 7 includes the Roujean f2 volume term from Equation (41) and is given as:

$$\begin{aligned} f_{m7} =& 4\rho_s D_b(\theta_h) F(\theta_d) G_c(\hat{\omega_i}, \hat{\omega_s}) \sigma(\theta_i, \theta_s) + \frac{\rho_d}{\pi} \\ &+ \rho_v \frac{4}{3\pi} \frac{1}{\cos\theta_i + \cos\theta_s} \left[\left(\frac{\pi}{2} - 2\theta_d \right) \cos 2\theta_d + \sin 2\theta_d \right] - \frac{1}{3}. \end{aligned} \tag{76}$$

Model 7 has only one additional parameter to the standard Cook-Torrance model. This accounts for the directional volume term. In total the parameters are ρ_s, ρ_d, ρ_v, m, n, and k. Table 3 shows the total number of fit parameters in each hybrid model. Each model is similarly parameterized ensuring equitable parameterization for model to model comparison.

Model	Number of Parameters
1	5
2	6
3	7
4	6
5	7
6	7
7	6

Table 3. The number of parameters in each model are comparable ensuring equitable parameterization across models.

3.3.1 Optimized Simulation.

The recursive optimization code uses a non-linear least squares curve fitting function in MATLAB®. This function reads in an initial parameter guess and finds final parameters that correspond to the best non-linear fit to the specified model for the given data. Upper and lower parameter bounds are specified for each model type as provided in Table 4. The number of iterations in the optimization depends on the fitting tolerance, initially set at 1e-6. Fit performance is based on the accuracy of the initial guess. Manually fitting each model to each data set will only converge to one local minima for that particular parameter guess. Accordingly, an array of best fit solutions is determined by randomly initializing 200 sets of parameter values that fall within the defined parameter bounds. Each incident angle is fit simultaneously for each of the models and the error is calculated for that solution. From the array of local best fits, the solution providing the lowest fit error is taken as the relative global best fit. The relative global best fit parameter set is stored and acts as the initial best guess for a second non-linear least squares fit with tighter fitting tolerance set at 1e-8. Here, all incident angles of the dataset are fit at once as the model best fit. The model best fit is taken as this final fit for comparison in this study.

Fits are calculated by fitting to the natural log of the measured BRDF data. BRDF often varies several orders of magnitude and drops off very quickly with devi-

Parameter	Symbol	Lower Bound	Upper Bound
Diffuse fit ρ_d	0	1	
Surface fit	ρ_s	0	100
Volume fit	ρ_v	0	100
Facet slope	m	0.00001	10
Real index	n	0	100
Imaginary index	k	0	100
Kubelka-Munk fit	R_∞	0	1
Sandford-Robertson fit	b	0	1
Oren-Nayar fit	σ	0	1

Table 4. This table shows upper and lower paramater bounds used in the fitting algorithm for each model.

ations from the specular peak; therefore, the logarithmic method allows for an emphasized fit over all observation angles, not just the model's forward specular peak. Fitting performance was based on the mean standard error (MSE) over all observation angles and is discussed further in the following section on error metrics.

To test the fitting algorithm, test data was created from an idealized model 2 BRDF solution with observation from $-85° < \theta_s < 85°$ and fit parameters of $\rho_d = 0.10$, $\rho_s = 2.00$, $\rho_v = 0.01$, $m = 0.1$, $n = 3.00$, and $k = 1.00$. The BRDF is shown in Figure 13.

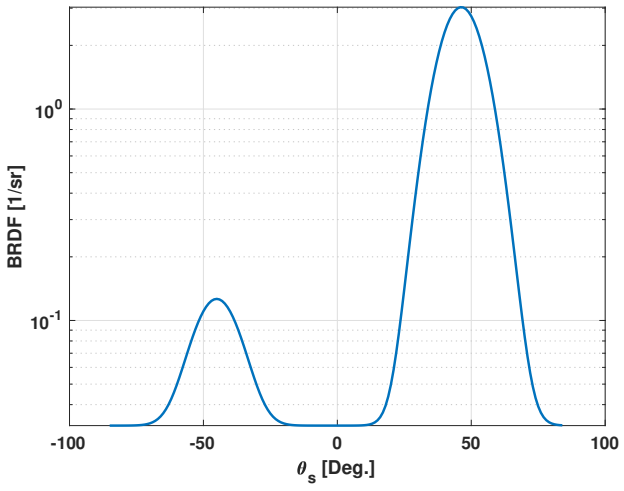

Figure 12. An example test dataset was built from a known model 2 BRDF solution.

From the ideal model, random error ranging between 0 and 10% was placed the on the ideal model at every 1° of observation. The resulting test dataset, shown in Figure 13, is representative of measured BRDF which often has measurement uncertainty less than 5%.

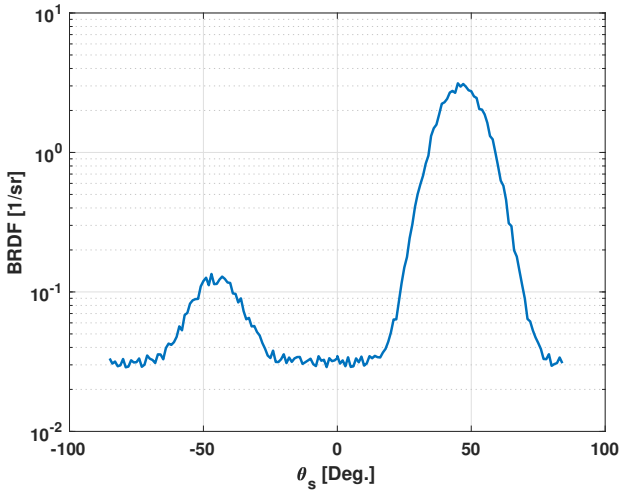

Figure 13. BRDF test data with 10% noise on the known model 2 solution.

The sample test data was fit to model 2 using the optimization algorithm with three converged local solutions, two of which were clearly poor fits. The parameters associated with the best local fits were stored and fit using the final model fit. Figure 14 shows the final model fit as well as the two additional local solutions found.

The final fit converged to parameter values of $\rho_d = 0.10$, $\rho_s = 2.14$, $\rho_v = 0.01$, $m = 0.1$, $n = 3.06$, and $k = 0.65$. Large changes in k result in small changes in the BRDF for this particular sample BRDF configuration; therefore, parameter k varied more significantly from the known value with little impact to best fit solution. All but the complex component of the index of refraction were fit to within 7% of the known parameter value.

Figure 15 shows application of the fitting algorithm to PNT65 MWIR measured BRDF data. Multiple fitting solutions are identified and the best of the local fits is

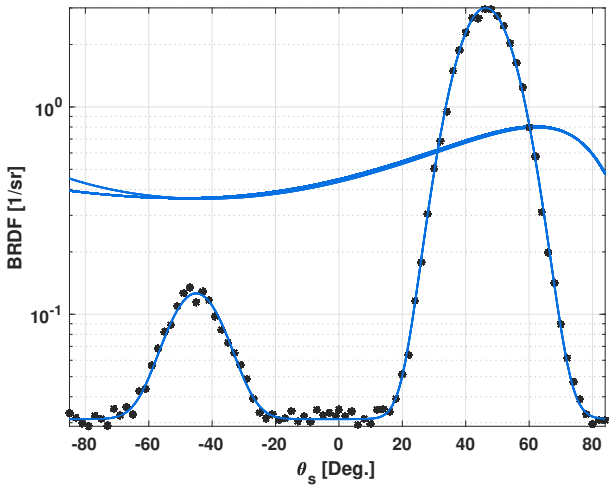

Figure 14. Fitting algorithm shows multiple local fit solutions (solid blue) to the test dataset (black asterisks). Relative global best fits are identified from the local solutions.

stored for final fitting. Determining the best fit is made by considering multiple error metrics discussed in detail in the following section.

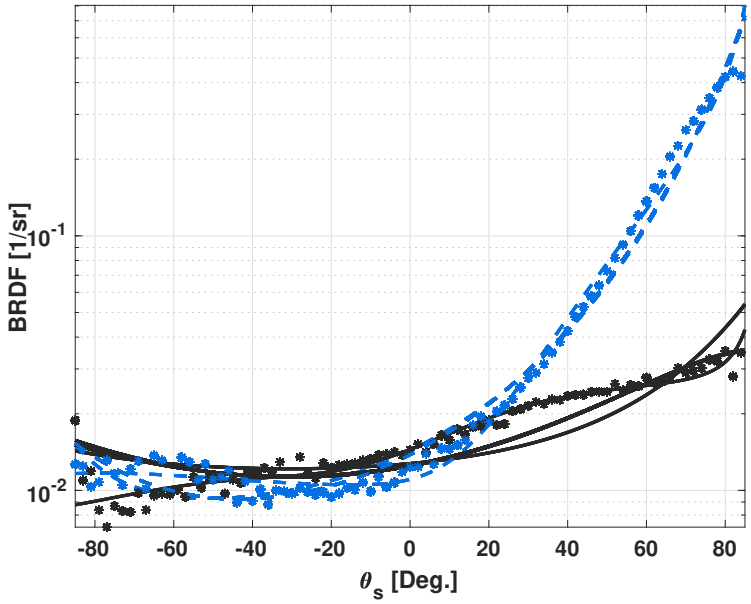

Figure 15. Preliminary tests of the fitting algorithm on PNT65 MWIR shows multiple local fit solutions (dashed blue and solid black) to the measured dataset (asterisks) at $\theta_s = 30°$ and $\theta_s = 60°$. Relative global best fits are identified from the array of local solutions.

3.3.2 Error Metrics.

Measurement noise is largest at the specular peak and drops off quickly at off-specular measurements. At 0.5° away from specular, measurement uncertainty is under 8% and is on average less than 3% over the full observation range for comparable systems [18, 35]. Accordingly, a conservative 5% average error metric was used first to compare all data against model 1, the standard Cook-Torrance model. This analysis ensured the Cook-Torrance model did not already fall within the measurement noise, or 5% of the measured value. All samples were considered on average over the full observation region and uniquely in four sub-regions: backscatter grazing, backscatter non-grazing, forward scatter non grazing, and forward scatter grazing. Backscatter grazing is defined for this study as observation angles less than 45° for $\phi_s = 0°$. Functionally this is plotted as $\theta_s < -45°$. Backscatter non-grazing is the observation region $-45° \leq \theta_s < 0°$. Forward scatter non-grazing is defined as $0° \leq \theta_s \leq 45°$. Forward scatter grazing is defined as $\theta_s > 45°$. The difference in the fit of model 1 to the data was checked at each point. The number of points that fell within the measurement noise was considered as well as the average fit over all measurement points. In all cases, model 1 was not within the measurement noise on average and the number of fitted values that fell within the noise was less than half the total number of data points, suggesting the average was not heavily skewed by a large number of measurements within the measurement noise. Over all cases, the Cook-Torrance model had fit values that fell outside the noise of the measurement, suggesting the fit is not capable of providing an optimal solution.

The square of the Mean standard error (MSE^2) is the primary error metric used in this study to quantify relative model performance. MSE is calculated as

$$MSE = \frac{1}{n}||ln(\vec{x}) - ln(\vec{f})||, \tag{77}$$

where $\vec{x}$ is the measured BRDF data, and $\vec{f}$ is the BRDF model fit using one of the seven models. To specify error within each observation sub-region, the Euclidean norm with n elements given by

$$||ln(\vec{x}) - ln(\vec{f})|| = \sqrt{\sum_{k=1}^{n} |ln(\vec{x_k}) - ln(\vec{f_k})|^2}, \tag{78}$$

can be squared to eliminate the square root thereby allowing each error sub-region to be independently expanded and given simply as:

$$(MSE)^2 = \frac{1}{n^2}\left(\sum_{k=1}^{m} |ln(\vec{x_k}) - ln(\vec{f_k})|^2 + \sum_{k=m+1}^{n} |ln(\vec{x_k}) - ln(\vec{f_k})|^2\right) \tag{79}$$

where if one defines point m as $\theta_s = 0$, within the array of n elements, one defines the contribution of error within the backscatter region and forward scatter region uniquely. The same can be done for the four sub-regions as previously defined.

Data was fit using the natural logarithm of the data to ensure models optimized over the full observation region. As discussed in the previous section, this avoids a biased fit to the forward specular peak and provides a clearer full model fit perspective.

Model fits are determined for both the full observation region and divided into each sub-region region for comparison. This allows observation of fit error shift that may be otherwise overlooked if only considering the full model MSE^2. This study considers MSE^2 at each incident angle equally. MSE^2 is the model performance metric used to identify the best fit solutions for each model. For instances where multiple equivalent best fit solutions were found over the full observation region, the parameter set giving the best backscatter MSE^2 was chosen next for the model best fit.

This study has two incident angles for the majority of samples and at most five incident angles investigated. While a single parameter set is fit for the entire model, such an approach with few incident angles will yield results biased toward that set

of incident angles. Accordingly, this study investigates the capabilities of each model uniquely and its ability to provide a best fit for the particular incident angles measured. Investigation of parameter scaling is presented as a topic of future work in Chapter 5. Chapter 4 presents results and analysis of this methodology.

IV. Results

Following the optimization algorithm described in Chapter 3, each of the 15 datasets were fit to six models. Recall, model 1 is the baseline model (modified Cook-Torrance) given by Equation (36) and model 2 given by Equation (71) is the baseline model plus a semi-empirically derived multi-lobe directional volume term. Model 3 given by Equation (72) is the baseline model plus the modified Kubelka-Munk directional volume scatter term. Model 4 given by Equation (73) is the baseline model plus the Beard-Maxwell directional volume term. Model 5 given by (74) is the baseline model plus the Sandford-Robertson directional volume term. Model 6 given by Equation (75) is the baseline model plus the Oren-Nayar directional volume term.

This chapter discusses the resulting fits, error metrics, and analysis of the study, with particular attention to backscatter as the notable region impacted by a directional volume scatter term. These results showed that a directional volume scatter term can improve backscatter modeling performance and overall model fit. Adding a directional volume term with the Cook-Torrance surface model can particularly improve fit quality for rough surface coatings that display both forward and backscatter specular lobes. Resulting fits for each model are presented as well as a bar chart for comparison of each model. Comparison of model fit quality to BRDF measurement is highlighted and cause of error is discussed. Three contributions of this thesis include (1) hybrid model development and comparison of volumetrically inclusive models to the Cook-Torrance model and (2) validation of volume scatter significance in BRDF modeling, and (3) evaluation of various existing directional volume terms for several different materials and several wavelengths. The following sections further outline these contributions.

4.1 Rough Surface Comparison

The following presents results for rough surface materials. PNT65 measurement data is presented for illumination by a NIR source along with each model fit. Solutions to model 7 did not converge using the optimization algorithm described in Chapter 3 and are not included. A subset of the randomized initial conditions would not allow model 7 convergence to a best fit solution or forced solutions by ignoring imaginary components. Further analysis is required as discussed in the future work section of Chapter 5. Figure 16 shows illumination at $\theta_i = 30^\circ$ and $\theta_i = 60^\circ$. Model 1 fits the Cook-Torrance model which does not include a directional volumetric term. Model 2 includes the semi-empricially derived directional volume term that allows for a backscatter specular lobe. The addition of this secondary specular lobe improves fit quality as seen in Figure 16(b) when compared to Figure 16(a). Across all five hybrid models, fit quality is noticeably impacted in the backscatter region.

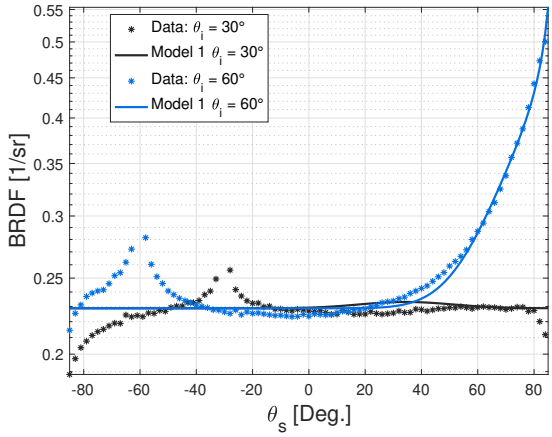

(a) PNT65 NIR data and model 1 fit

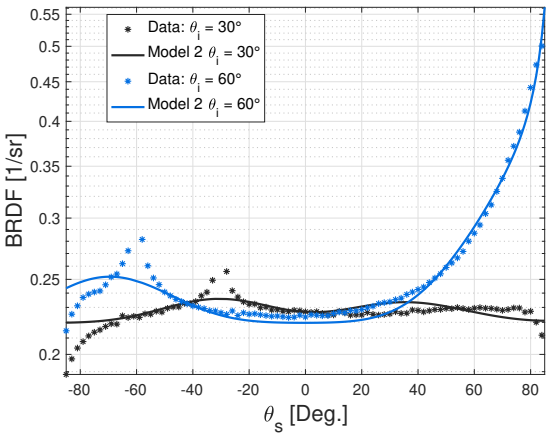

(b) PNT65 NIR data and model 2 fit

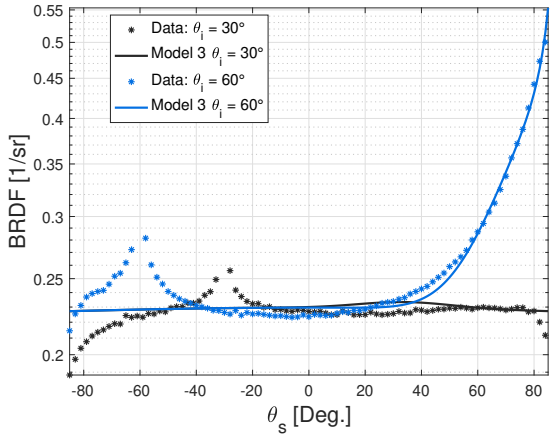

(c) PNT65 NIR data and model 3 fit

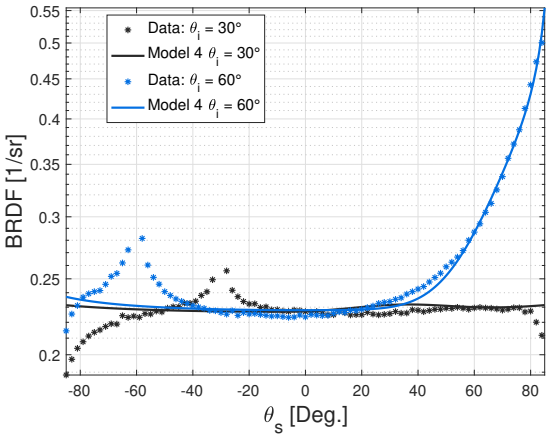

(d) PNT65 NIR data and model 4 fit

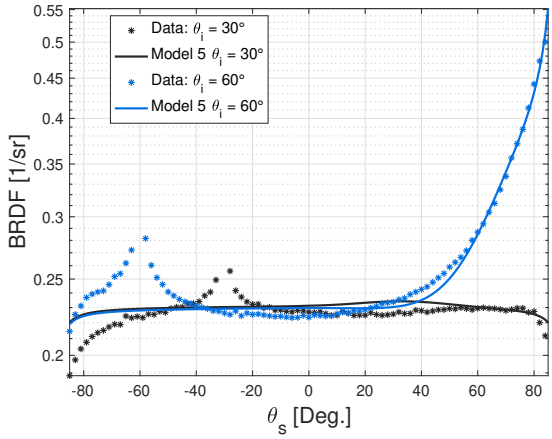

(e) PNT65 NIR data and model 5 fit

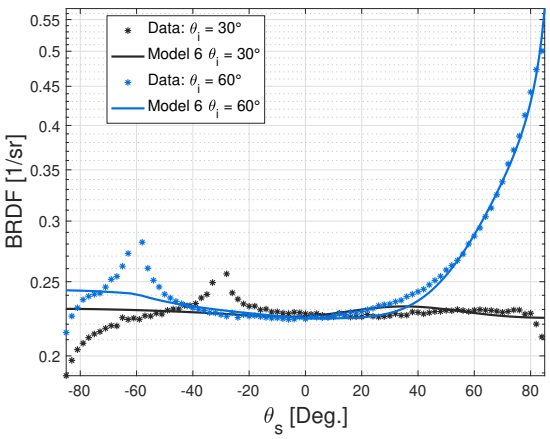

(f) PNT65 NIR data and model 6 fit

Figure 16. Resulting 6 models fit to diffuse paint (PNT65) illuminated by a NIR source.

Recall from Chapter 4 the square of the mean standard error over all incident angles is the primary performance metric in this study. This allows model comparison for a specific observation region since MSE is an average error over all observation locations not a total error. Figure 17 shows an example stacked error figure used throughout this work. For each model, the square of the mean standard error is determined based on the model fit. Full model error over the full observation region is categorized into each contributing amount of error by observation region. Forward scatter and backscatter are defined as $\theta_s \geq 0°$ and $\theta_s < 0°$ respectively. Forward grazing and backscatter grazing is defined as $\theta_s > 45°$ and $\theta_s < -45°$ ($\theta_s > 45°$; $\phi_s = 0°$) respectively. Each fit is presented similarly for comparison across models as shown in Figure 18.

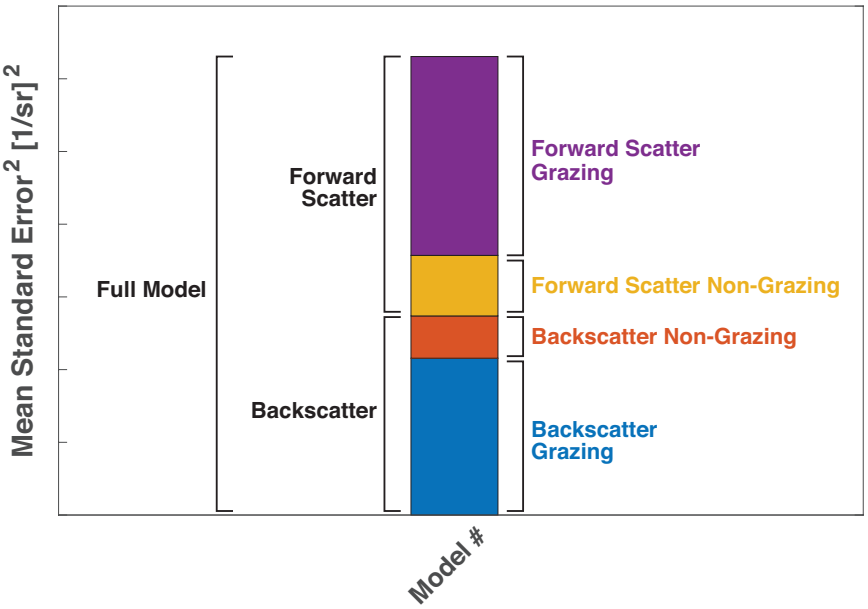

Figure 17. Each model fit includes a depiction of the full model error divided into contributing error by region.

Figure 18 shows model 2 provided 50% decrease in error over the baseline model (model 1). Forward scatter error increased 19% while backscatter fit quality improved 59%. Backscatter grazing showed the largest improvement over model 1 at 60%.

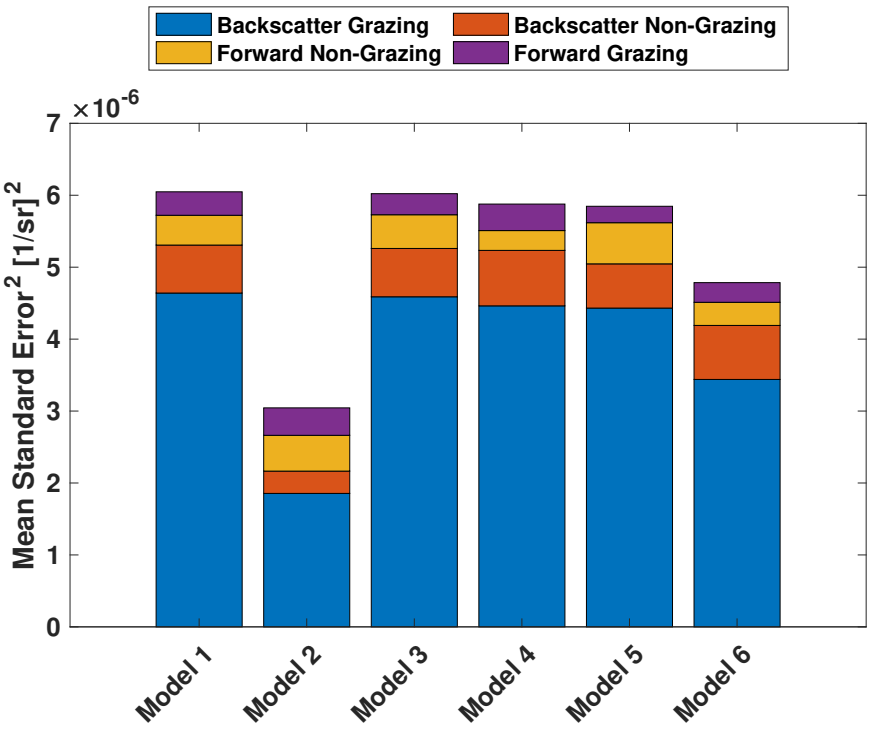

Figure 18. This PNT65 NIR model comparison bar chart shows error broken into regions contributing to the full model error. Including a directional volumetric term improved performance over model 1 in 4/5 hybrid models, most notably for backscatter grazing.

The remainder of this section is presented as a condensed version of Figure 16 and Figure 18. Each figure provides model 1 as the baseline model. Two additional noteworthy fits are also presented. One is the model with the best fit quality and the second is a fit worthy of additional discussion. This additional plot provides unique insight to this study such as a fit that converges to the model 1 baseline solution, or one that shows significant improvement, etc. The error bar chart is also provided for a glancing comparison across all models. For highly specular materials or materials with overlapping backscatter peaks, an additional set of scaled plots is provided to more clearly see the fit quality at the point of specular backscatter. Appendix A provides the reader with all model fit plots for each material at each illumination wavelength in the same format as Figure 16.

In 37 of 75 fits, the hybrid model converged to the model 1 (Cook-Torrance)

baseline solution. This baseline solution does not include a directional volume scatter term. In these instances, either ρ_v converges to 0 or a directional volume specific parameter forced the directional volume scatter term to 0 thereby duplicating the function and fit found by model 1. This occurs in general for three cases: (1) when the forward specular lobe largely dominates the BRDF profile, (2) when the material exhibits low volume scatter behavior, and (3) when the directional scatter term in the model describes Lambertian scatter in its limiting case. Each is discussed further in the summary of results at the end of this chapter.

The following presents results for the remaining rough surface materials. Figure 19 shows models 2, 4, and 6 improved fit quality over model 1 for PNT65 MWIR. Model 2 and 6 showed the largest improvement with 9% full model error reduction. The majority of model 2 improvement is found in the backscatter grazing region with 27% improvement. Functionally, backscatter grazing regions occur at $||\theta_s|| > 45^\circ$ and $\phi = 0$. Models 3 and 5 converged to the baseline solution.

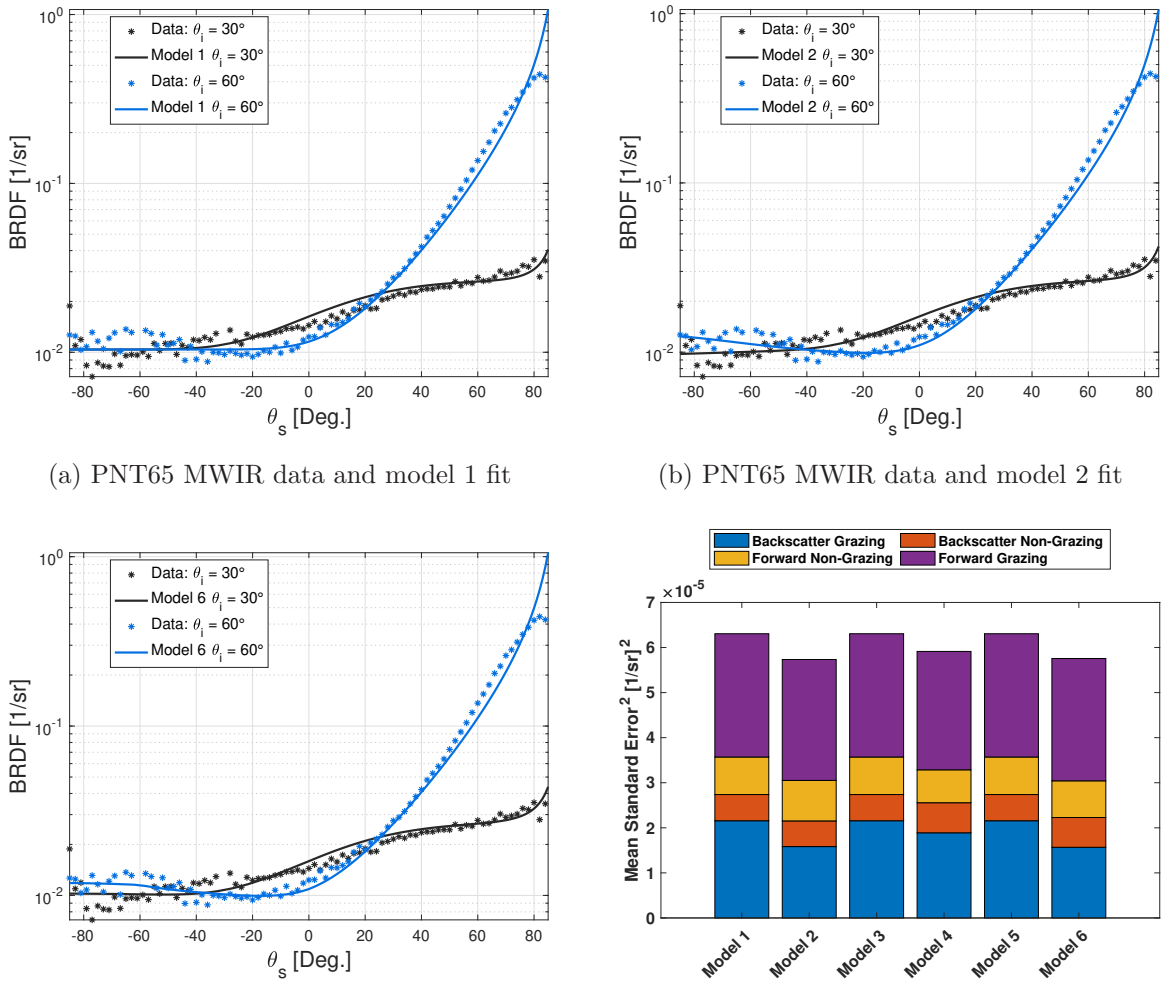

(a) PNT65 MWIR data and model 1 fit

(b) PNT65 MWIR data and model 2 fit

(c) PNT65 MWIR data and model 6 fit

(d) PNT65 MWIR model comparison bar chart

Figure 19. Resulting fits of diffuse paint PNT65 illuminated by a MWIR source show small improvement with the directioanl volume terms in models 2, 4, and 6. Improvements are predominantly found at large observation angles in the backscatter grazing region.

As shown in Figure 20, results for diffuse paint PNT65 LWIR show model 5 provided the best overall error decrease at 6% as well as the best backscatter fit quality with 63% error reduction over model 1. Model 3 provided similar full model improvement, albeit a slightly smaller improvement to backscatter at 54% error reduction. Backscatter grazing fit quality is most improved by the directional volume terms by modeling the non-Lambertian attenuation behavior observed at large observation an-

gles. At 60° incident angle, the material exhibits more forward specular behavior than at 30° but is still not highly specular. Accordingly, the forward specular peak is not well weighted by measurements at its highest specular data point and the models consistently underestimate the forward grazing lobe. Models 2, 4, and 6 converged to the baseline solution.

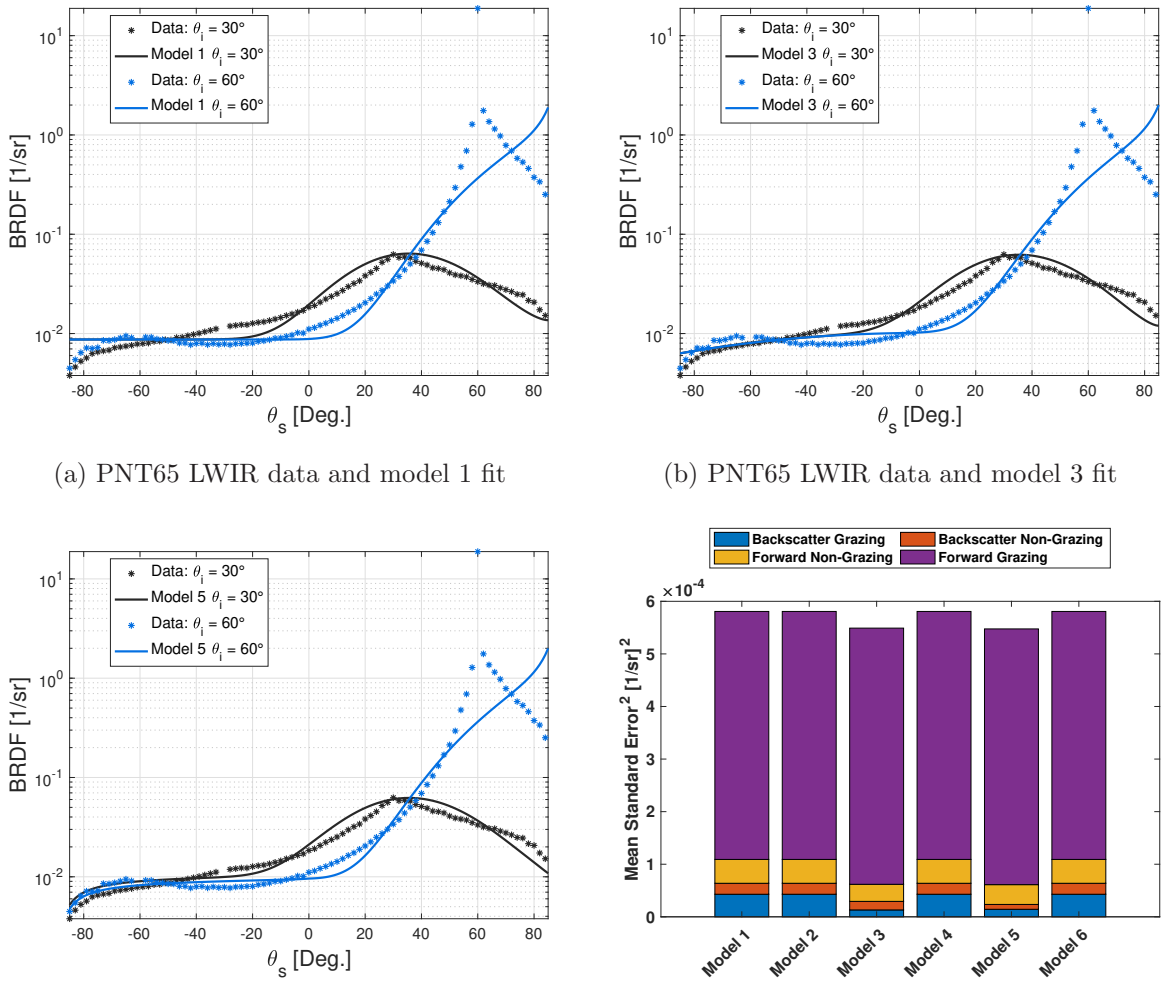

(a) PNT65 LWIR data and model 1 fit

(b) PNT65 LWIR data and model 3 fit

(c) PNT65 LWIR data and model 5 fit

(d) PNT65 LWIR model comparison bar chart

Figure 20. Resulting fits to diffuse paint PNT65 LWIR show model 5 provides 45% **error reduction in backscatter. Model 4 converged to the baseline solution.**

Figure 21 shows results for diffuse paint PNT65 illuminated by a UV source. Model 6 provided the best full model fit improvement of this study with 78% error

reduction over the full observation range. Backscatter error was reduced 92% from the baseline with the majority of improvement observed at $\theta_i = 60°$. Model 2 showed 69% full model improvement and a significant (91%) improvement in the forward scatter region. Models 3 and 5 converged to the baseline solution.

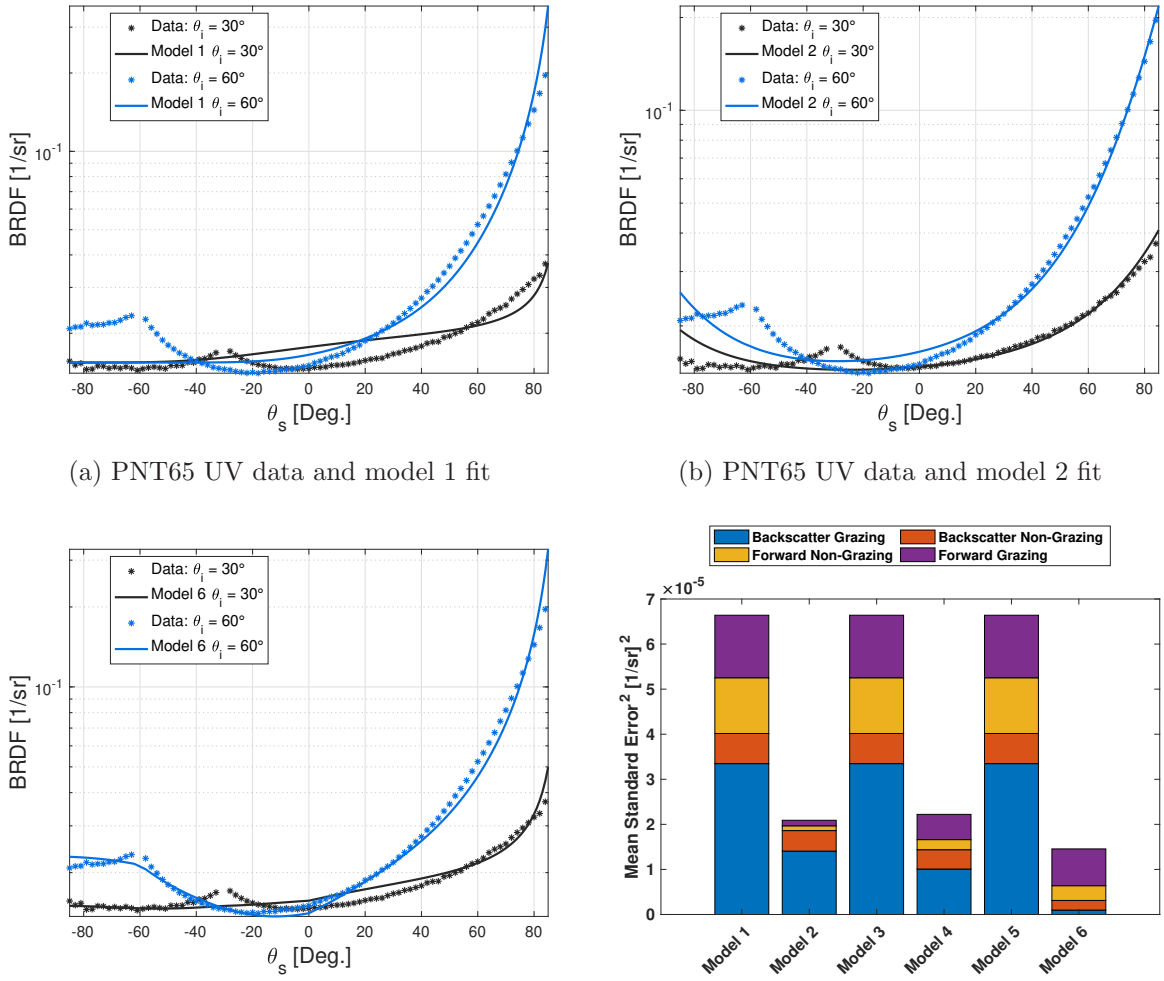

(a) PNT65 UV data and model 1 fit

(b) PNT65 UV data and model 2 fit

(c) PNT65 UV data and model 6 fit

(d) PNT65 UV model comparison bar chart

Figure 21. Model 2 improved fit quality 69% **with the largest improvement to the forward scatter region. Model 6 showed the largest backscatter fit improvement with** 92% **reduction in MSE^2 for diffuse paint PNT65 UV.**

Results of PNT65 VIS shown in Figure 22 show that the baseline model struggles to capture specular backscatter behavior despite reasonable forward scatter performance. The directional volume term in model 2 allows the surface term to improve

forward specular fit and specular backscatter fit simultaneously. Model 2 provided the best full model fit improvement with 75% MSE^2 reduction over the full observation range. Fit quality is improved specifically in the backscatter region by 85% by capturing the backscatter specular features otherwise unmodeled by the baseline. Models 3 and 5 converged to the baseline solution. Forward grazing error increased slightly in model 2 and model 6 in exchange of improved backscatter grazing fit quality.

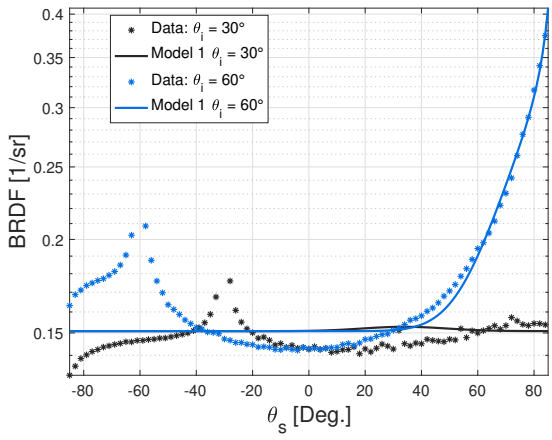

(a) PNT65 VIS data and model 1 fit

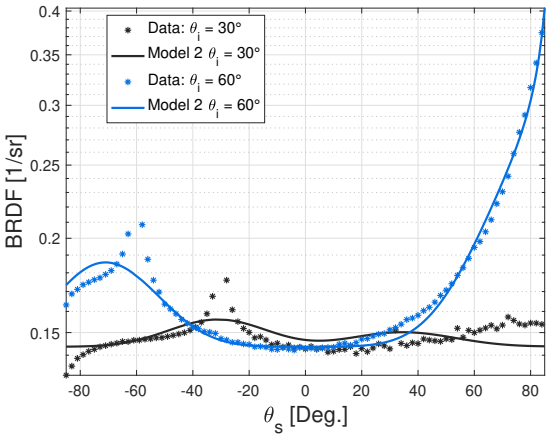

(b) PNT65 VIS data and model 2 fit

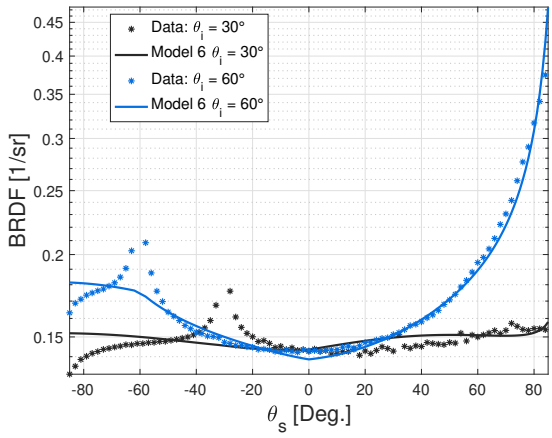

(c) PNT65 VIS data and model 6 fit

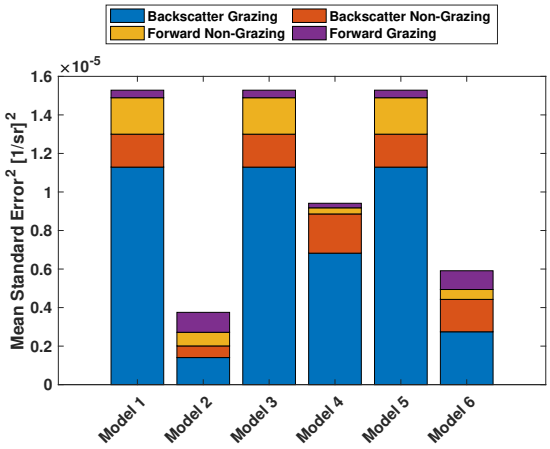

(d) PNT65 VIS model comparison bar chart

Figure 22. PNT65 VIS fit to model 2 improved full model fit quality 75% largely by capturing the non-Lambertian backscatter specular peaks. Models 3 and 5 converged to the baseline solution. Model 6 improved total fit quality 61% at the expense of an increase in forward grazing error.

Results for PNT66 NIR shown in Figure 23 show model 3 provided little full model improvement at 6%, but increased error in the forward scatter non-grazing region by 18%. Models 2, 4, and 6 converged to the baseline solution while models 3 and 5 found improvement in the forward grazing region. MSE^2 is reduced in the backscatter grazing region by 16% with model 5.

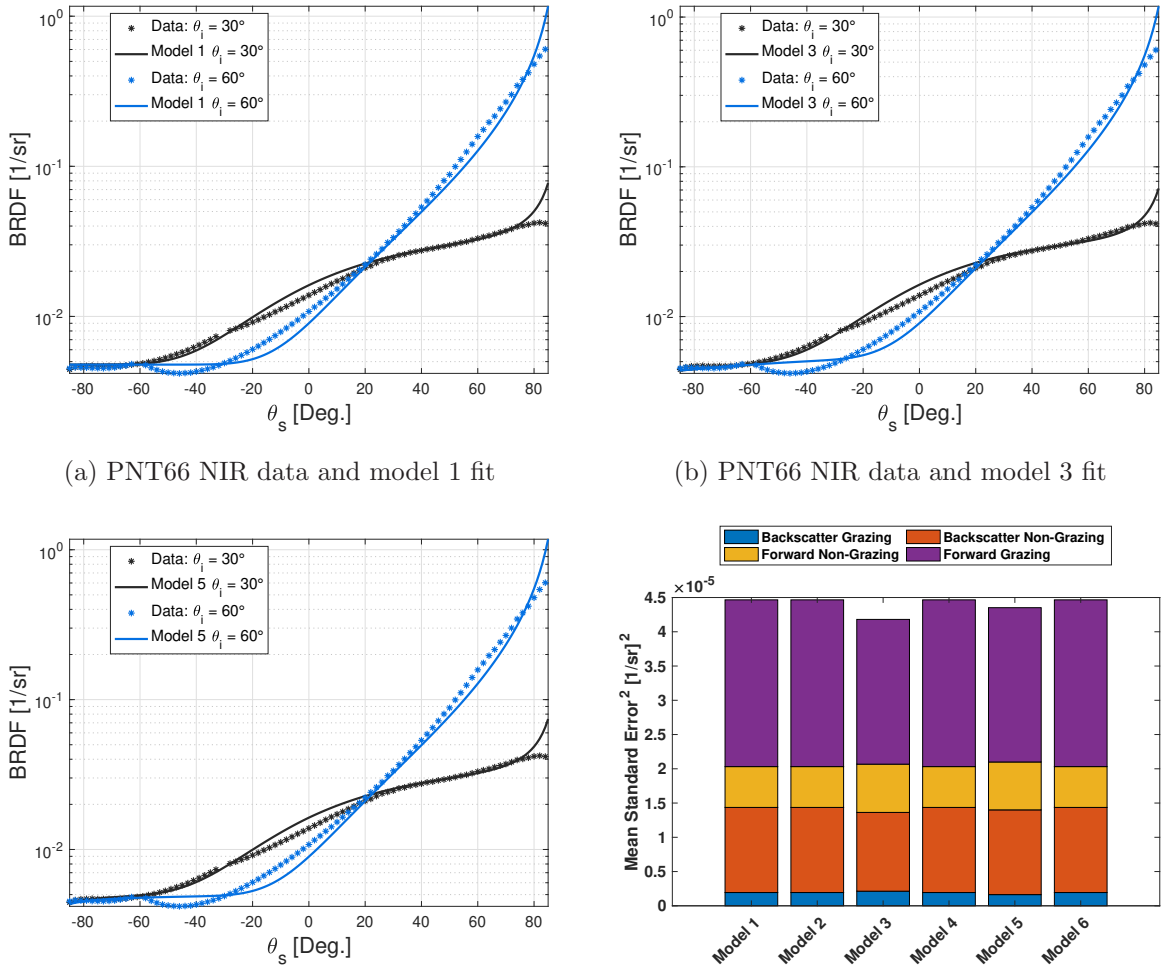

(a) PNT66 NIR data and model 1 fit

(b) PNT66 NIR data and model 3 fit

(c) PNT66 NIR data and model 5 fit

(d) PNT66 NIR model comparison bar chart

Figure 23. PNT66 NIR shows little improvement for all models. The lack of a dominant specular backscatter peak allows the baseline to fit reasonably well. Models 2, 4, and 6 converged to the baseline solution.

Results of PNT66 MWIR data fit to all models show statistically insignificant improvements in all but model 5. Statistical significance is taken as improvements in

MSE^2 greater than 10%. Most notable improvement in model 5 is in the backscatter non-grazing region at 44% where the directional volume term better fits the non-lambertian attenuating backscatter. Models 2, 4, and 6 converged to the baseline solution. Improvements are minimal due in part to the large measurement noise in the backscatter grazing region.

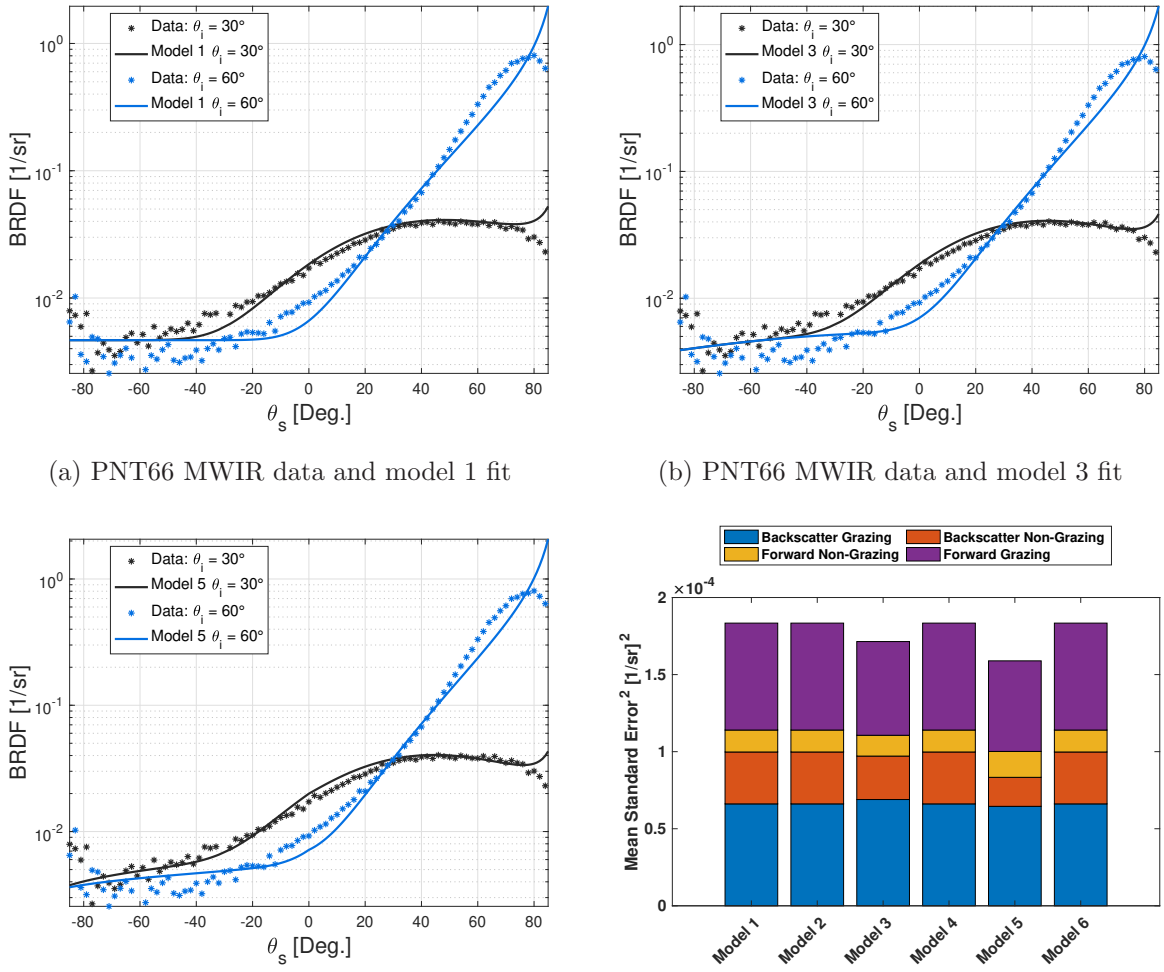

(a) PNT66 MWIR data and model 1 fit

(b) PNT66 MWIR data and model 3 fit

(c) PNT66 MWIR data and model 5 fit

(d) PNT66 MWIR model comparison bar chart

Figure 24. PNT66 MWIR fits show statistically insignificant improvements over model 1. Improvements are minimal due in part to large measurement noise in the backscatter region.

Results of PNT66 UV show models 2, 3, 5, and 6 converged to the baseline solution. Model 4 showed statistically insignificant full model improvement of 2%.

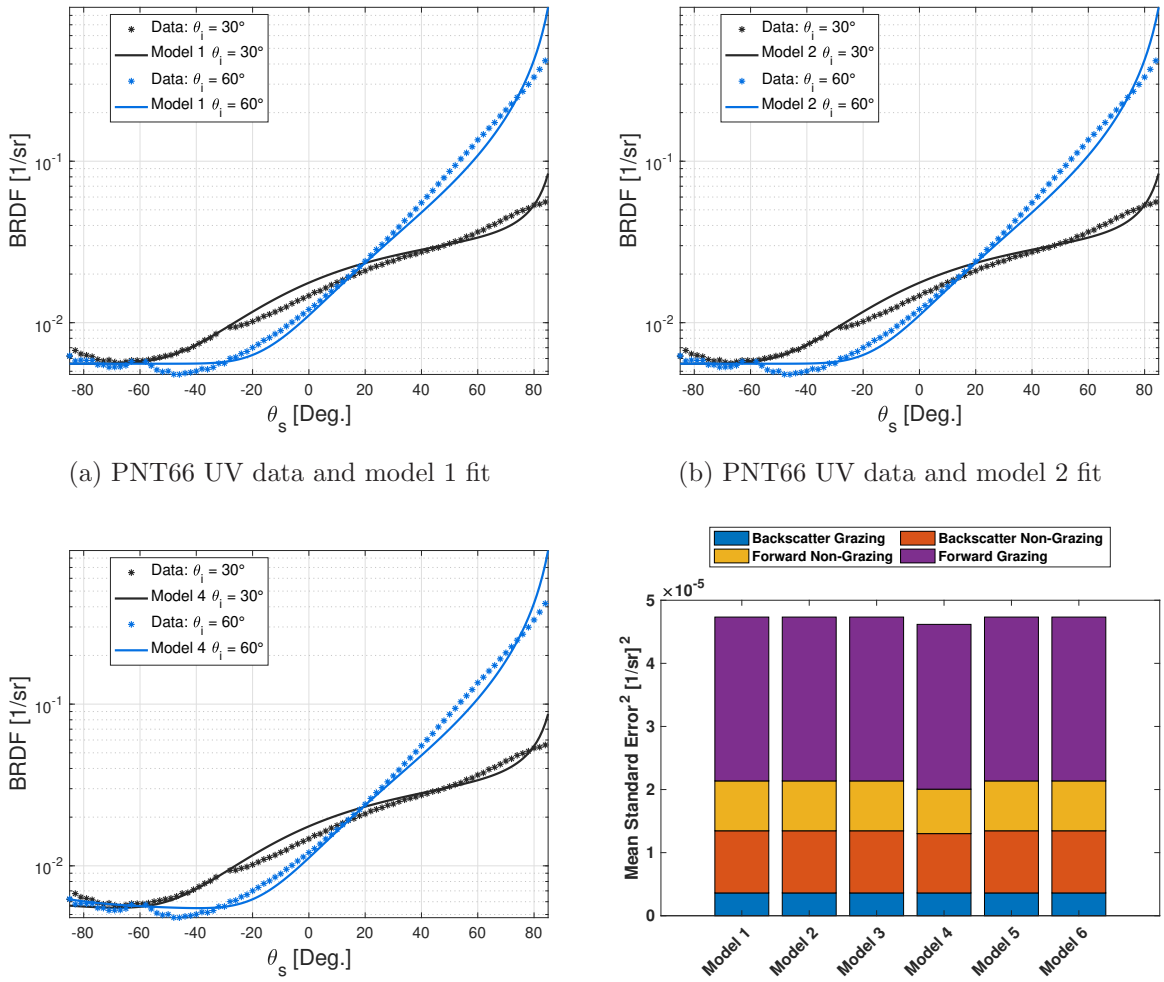

(a) PNT66 UV data and model 1 fit

(b) PNT66 UV data and model 2 fit

(c) PNT66 UV data and model 4 fit

(d) PNT66 UV model comparison bar chart

Figure 25. PNT66 UV fit to all models shows negligible 2% improvement over the baselien with model 4. All other models converged to the baseline solution.

PNT36375 NIR measurements show a strong specular backscatter signature. Model 2 provides a strong specular backscatter lobe which makes it well suited to improve fit quality with this material. Figure 26 shows model 2 provided the best MSE improvement for PNT36375 NIR at 24% over the full observation range and 55% in the backscatter region. Model 6 improved backscatter fit quality 51% with the majority of improvement observed at large incident angles in the backscatter grazing region. Models 3 and 5 converged to the baseline solution.

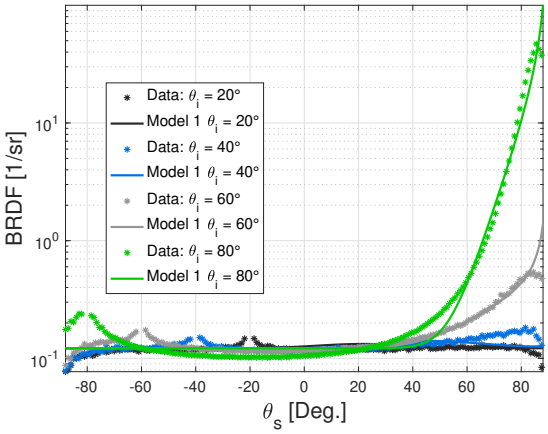

(a) PNT36375 data and model 1 fit

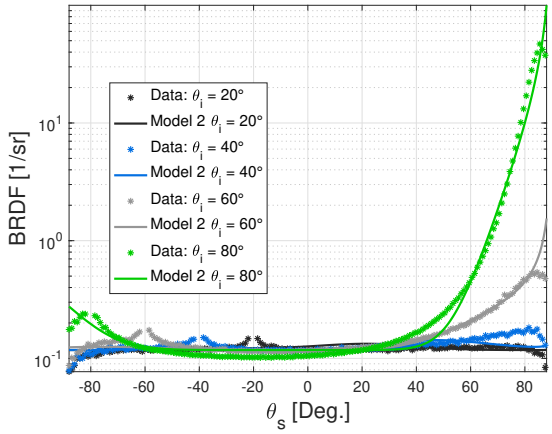

(b) PNT36375 data and model 2 fit

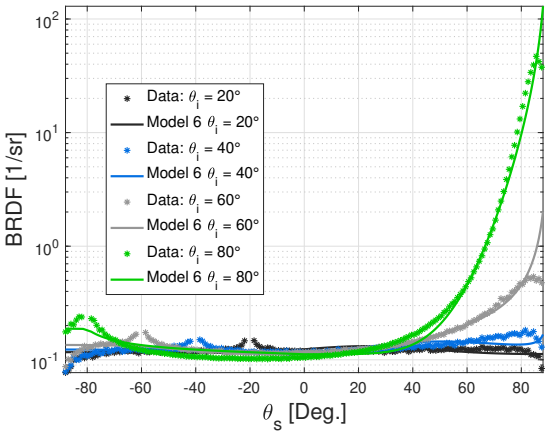

(c) PNT36375 data and model 6 fit

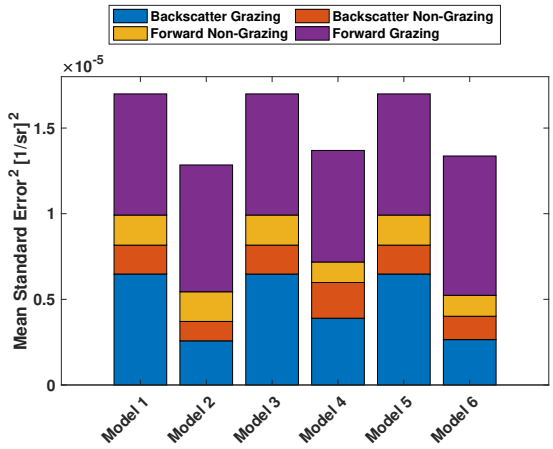

(d) PNT36375 NIR model comparison bar chart

Figure 26. PNT36375 NIR fit results show models 2 and 6 provided 24% and 21% MSE^2 full model improvement respectively. Improvements are most notable at large incident angles and backscatter grazing observations where strong specular backscatter lobes are present.

Figure 27 shows a closer look at PNT36375 NIR results with particular attention given to the specular backscatter region. Models 2 and 6 better simulate the backscatter specular peak that is otherwise unmodeled by the baseline.

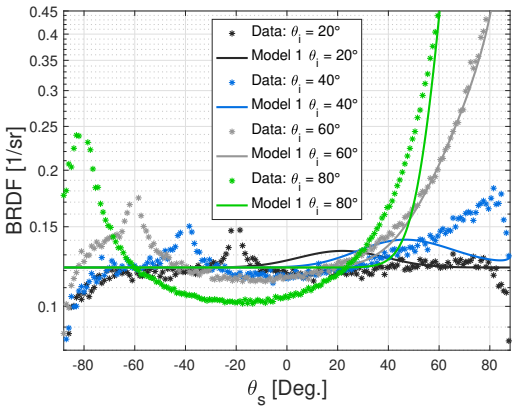

(a) PNT36375 data and model 1 fit

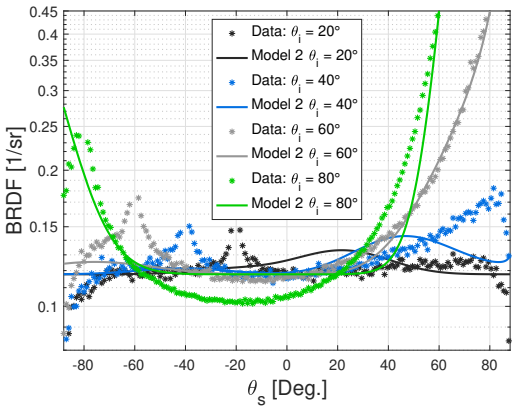

(b) PNT36375 data and model 2 fit

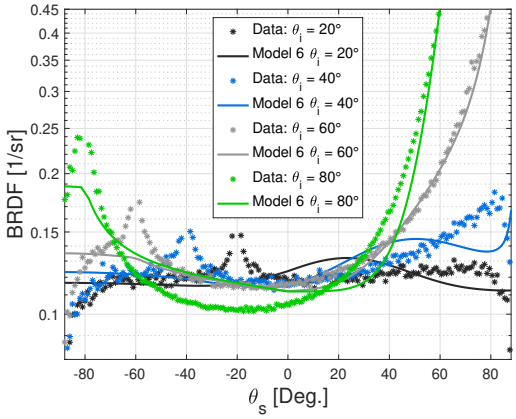

(c) PNT36375 data and model 6 fit

Figure 27. A closer look at the PNT36375 NIR fit results show model 2 provided 55% **MSE^2 improvement in the backscatter region by capturing the specular peak at $\theta_i = 80°$ that is unmodeled in the baseline. Model 6 also performs well at large incident angles.**

Results of PNT36495 VIS show model 2 provided the best error reduction by improving backscatter fit quality by 56%. Full model MSE^2 is reduced 17% with the most notable improvement at the backscatter specular peaks. Model 3 converged to the baseline solution while model 5 converged to a solution similar to the model 1 fit by allowing the directional volumetric scatter term to behave Lambertian. Model 6 improved backscatter grazing fit quality 54% most notably by simulating a specular increase near grazing observation at large incident angles.

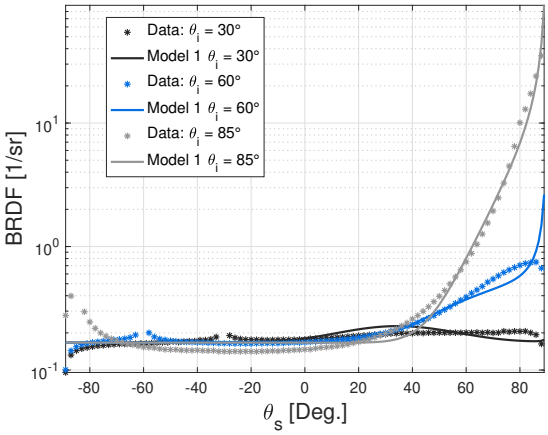

(a) PNT36495 data and model 1 fit

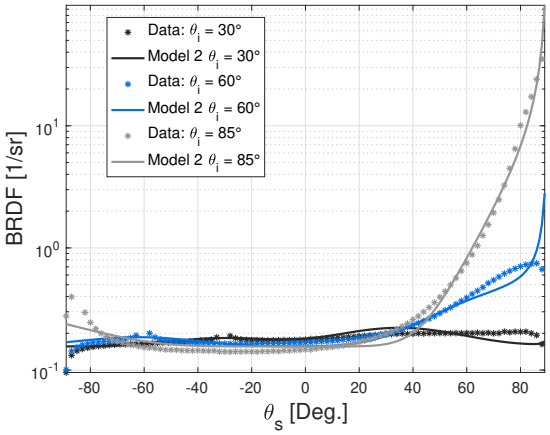

(b) PNT36495 data and model 2 fit

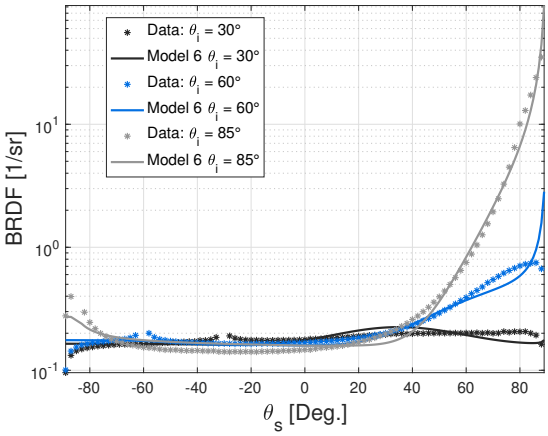

(c) PNT36495 data and model 6 fit

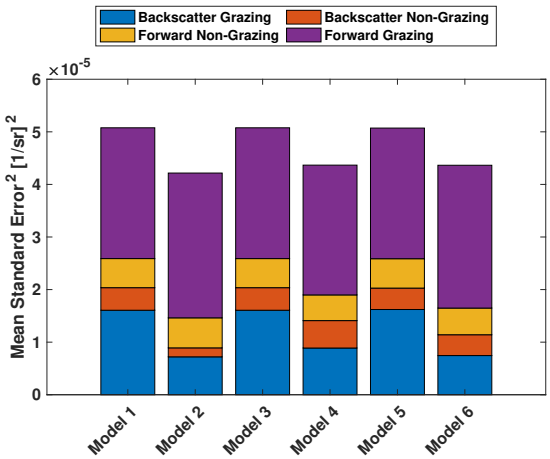

(d) PNT36495 VIS model comparison bar chart

Figure 28. PNT36495 VIS fit to model 2 provided the best fit quality improvement with 56% MSE^2 reduction in the backscatter region. Model 6 fits well at large incident angles but underestimates backscatter at lower incident angles.

Figure 29 shows a closer look at PNT36495 VIS results with particular attention given to the specular backscatter region. Model 2 more closely models the backscatter specular peak that is otherwise unmodeled by the baseline model. As a result, backscatter fit is improved by 56%.

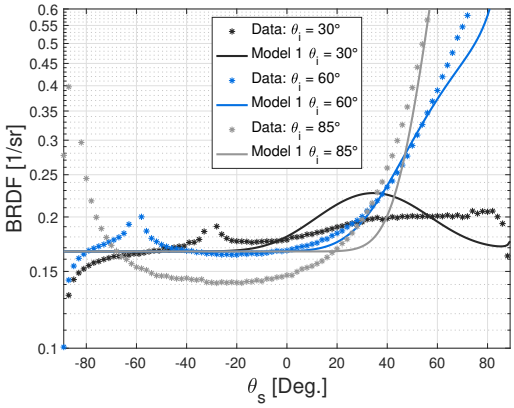

(a) PNT36495 data and model 1 fit

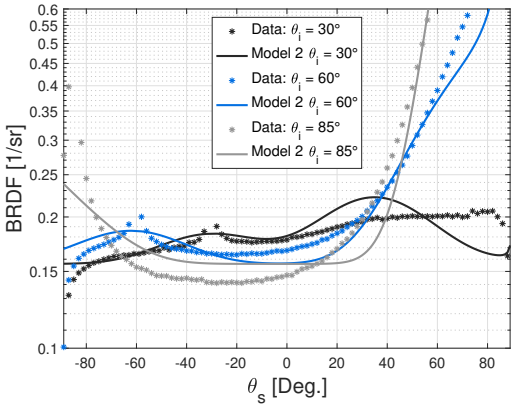

(b) PNT36495 data and model 2 fit

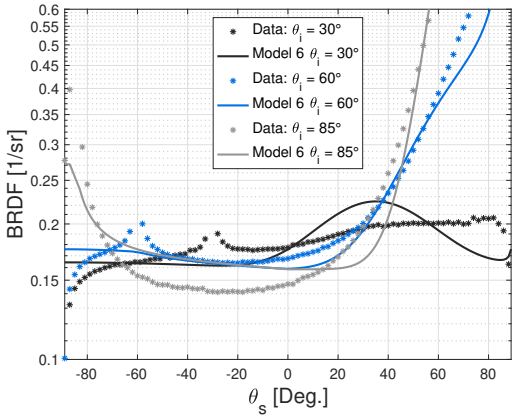

(c) PNT36495 data and model 6 fit

Figure 29. PNT36495 VIS fit to model 2 provided the best fit quality improvement with 56% MSE reduction in the backscatter region. Model 6 fits well at large incident angles but more clearly underestimates backscatter at lower incident angles.

4.2 Polished Surface Comparison

The following section presents results for specular paints PNT01006 and PNT01014. All models showed statistically insignificant improvements over the baseline solution provided with model 1. The directional volume scatter terms included in each hybrid model are anticipated to improve fit quality in materials displaying high volume scatter. For these specular materials, the diffuse scatter structure is less pronounced

compared to the large forward specular peak. Accordingly, improvements to the diffuse scatter regions are largely overshadowed by existing error in the forward specular lobe.

Figure 30 shows PNT01006 fit to all models. Particularly at small incident angles and grazing observations, model 5 outperformed model 1. In general, however, fit improvement is minimal for this highly specular material as the diffuse scatter structure is less pronounced compared to the large specular peak. Model 5 showed 5% MSE^2 reduction over the full observation region but 51% MSE improvement in the backscatter grazing region. Model 4 and 6 converged to the baseline solution while model 2 converged to a unique solution with similar performance as the baseline. Model 3 improved backscatter grazing fit quality 28%.

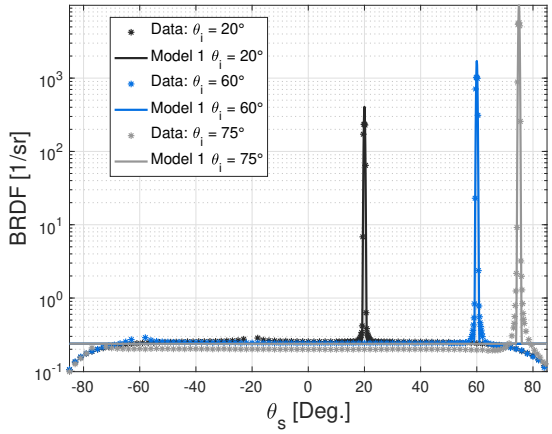

(a) PNT01006 data and model 1 fit

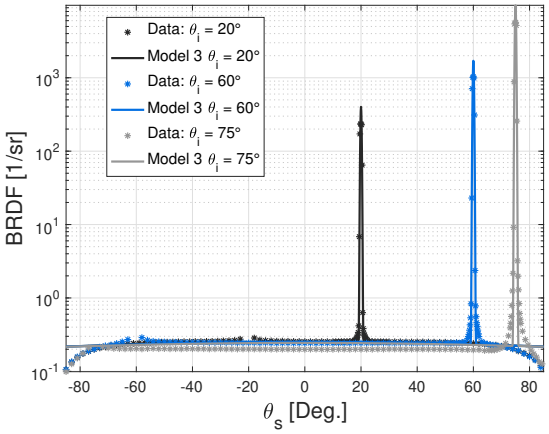

(b) PNT01006 data and model 3 fit

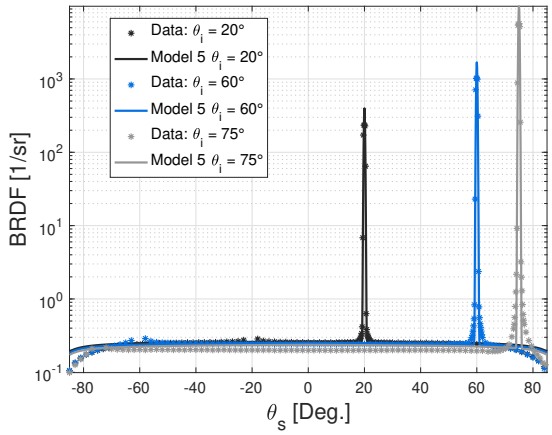

(c) PNT01006 data and model 5 fit

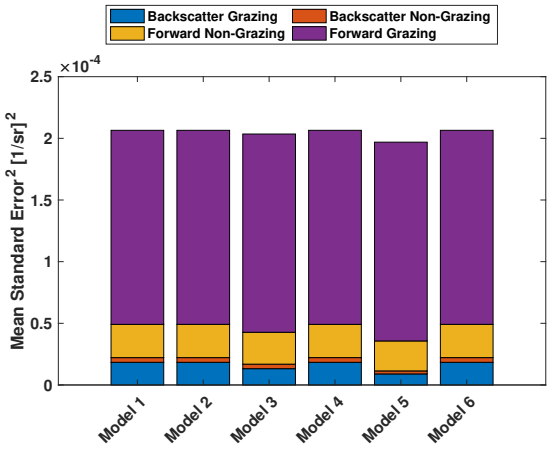

(d) PNT01006 NIR comparison bar chart

Figure 30. PNT01006 fit improvements are minimal for this highly specular material as the diffuse scatter structure is less pronounced compared to the large specular peak. Accordingly, improvements are largely in the backscatter grazing regions and are in total overshadowed by error in the forward specular lobe.

Figure 31 shows a closer look at PNT01006 NIR results with particular attention given to the specular backscatter region.

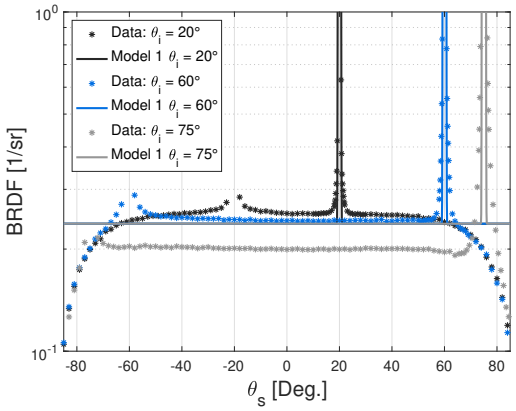

(a) PNT01006 data and model 1 fit

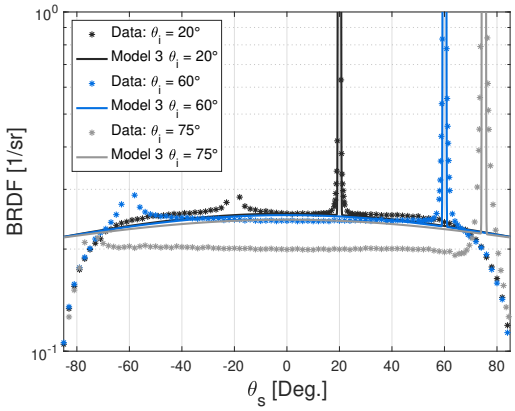

(b) PNT01006 data and model 3 fit

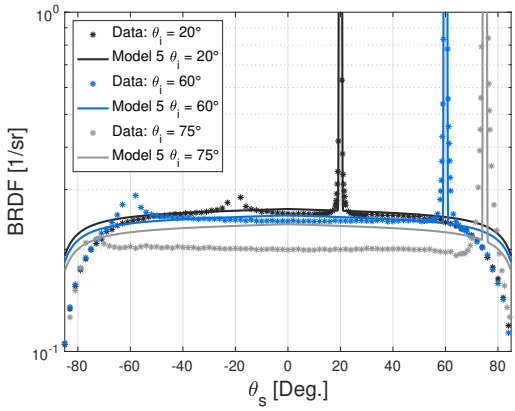

(c) PNT01006 data and model 5 fit

Figure 31. PNT01006 fit improvements are largely located in the backscatter region and are in total overshadowed by error in the forward specular lobe. Improvements are most notable at $||\theta_s|| > 45°$.

Figure 32 shows that models fit to PNT01014 NIR data suffer similar specular peak bias as seen with PNT01006 NIR. Fit improvement is again minimal as any improvements to diffuse scatter are overshadowed by error in the forward specular lobe. Models 2, 3, 5, and 6 converged to the baseline solution. Model 4 uniquely weighted the forward specular peak to provide a solution with increased forward scatter fit quality by 17%. This occured at the expense of a large increase to the backscatter error, thereby reducing the full model improvement to 5%.

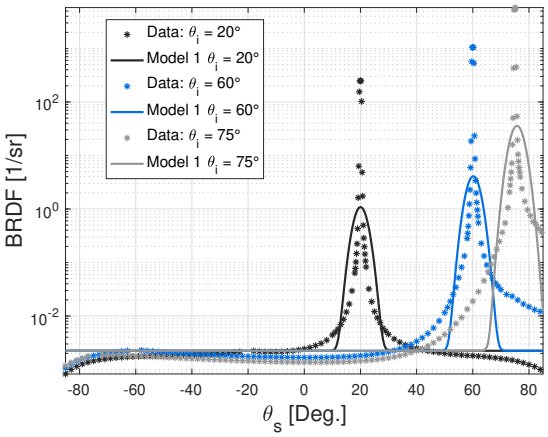

(a) PNT01014 data and model 1 fit

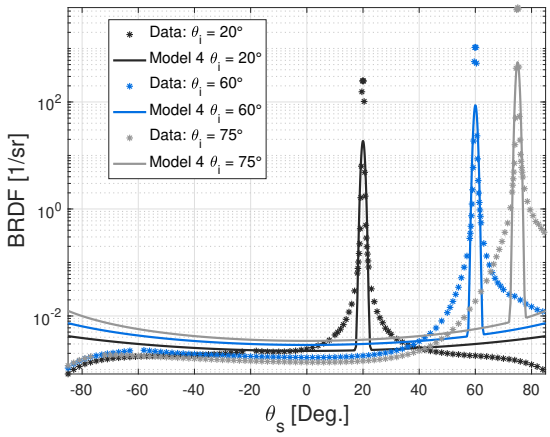

(b) PNT01014 data and model 4 fit

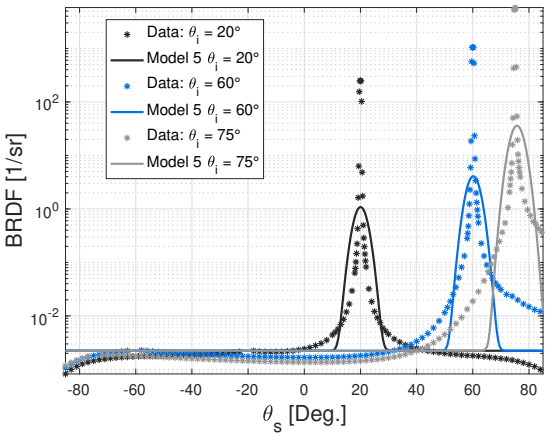

(c) PNT01014 data and model 5 fit

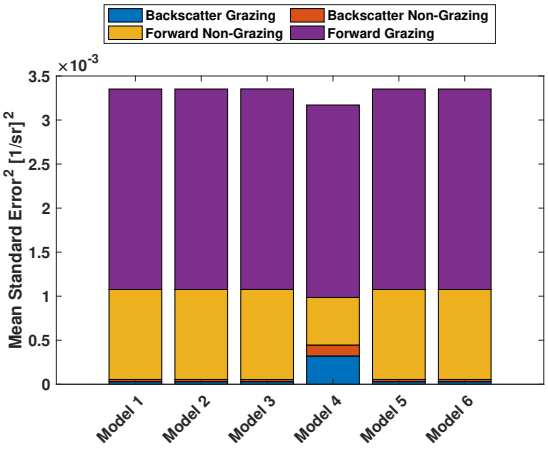

(d) PNT01014 NIR comparison bar chart

Figure 32. Models fit with PNT01014 NIR data suffer from specular peak biasing. Overall MSE improvement is minimal as any improvements to diffuse scatter are overshadowed by error in the forward specular lobe. Accordingly all models show MSE improvements less than 5%**.**

Figure 33 shows a closer look at PNT01014 NIR results with particular attention given to the specular backscatter region.

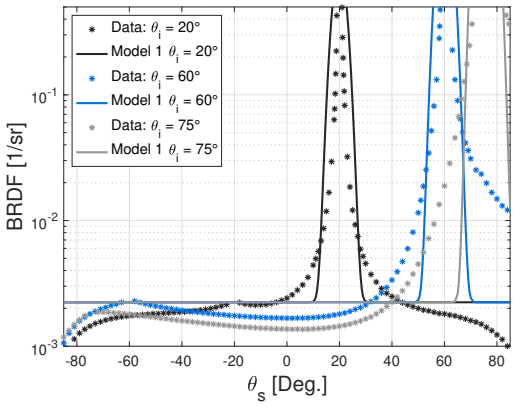

(a) PNT01014 data and model 1 fit

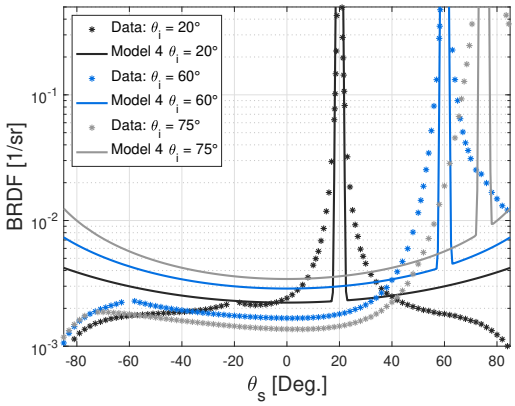

(b) PNT01014 data and model 4 fit

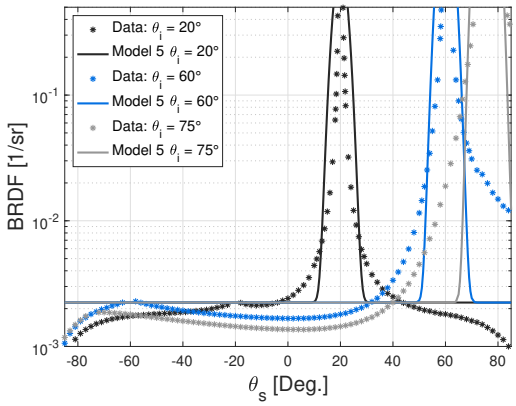

(c) PNT01014 data and model 5 fit

Figure 33. Models fit with PNT01014 NIR data suffer from specular peak biasing. Overall MSE improvement is minimal as any improvements to the relatively diffuse backscatter region is overshadowed by error in the forward specular lobe. Model 4 loses fit quality near grazing in exchange for improved forward specular fit. Alternatively, all other models 5 show equivalent performance as the baseline.

4.3 NIST Standards Comparison

The following presents results and analysis of three NIST standards. Figure 34 shows STD00696 MWIR fit with models 1, 3 and 5. All three standards exhibit low volume scatter and high surface scatter. Accordingly the addition of a directional volume term in each hybrid model is most impactful for non-Lambertian grazing ob-

servations but in general do not provide statistically significant full model improvement over the baseline. Model 3 and 5 performed similarly with MSE^2 reductions of 8% and 7% respectively over both the full observation range. Models 2, 4, and 6 converged to the baseline solution.

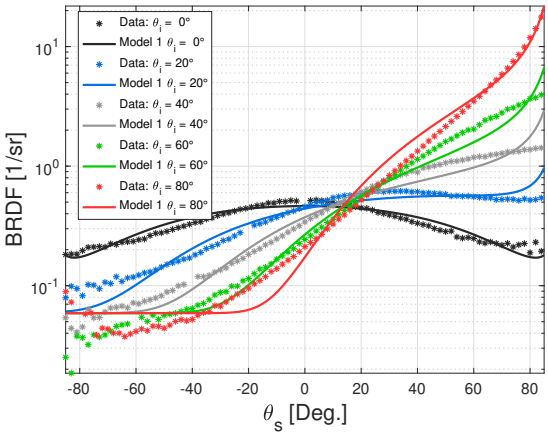

(a) STD00696 data and model 1 fit

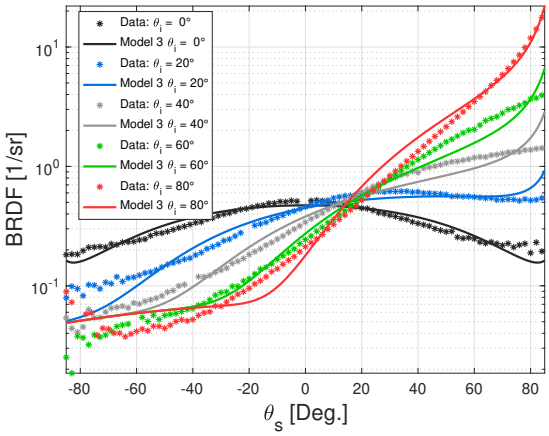

(b) STD00696 data and model 3 fit

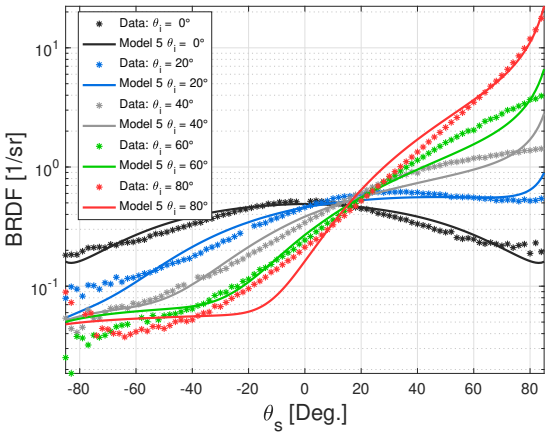

(c) STD00696 data and model 5 fit

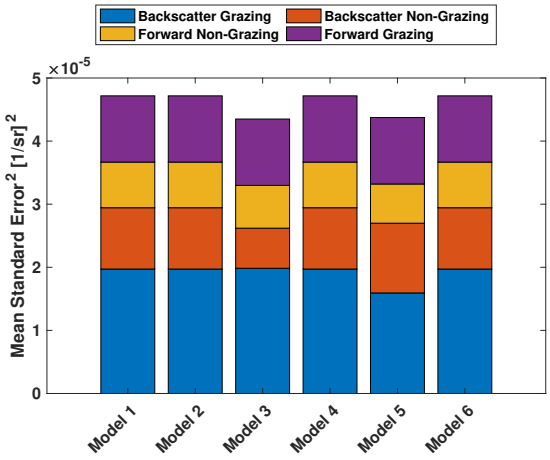

(d) STD00696 MWIR comparison bar chart

Figure 34. STD00696 MWIR fit to models 3 and 5 showed statistically insignificant improvement over the baseline, while models 2, 4, and 6 converged to the baseline solution. This material exhibits high surface scatter and low volume scatter. Accordingly, existing error in the surface model largely overshadow improvements gained in the volume components.

Figure 35 shows STD00698 MWIR results. The baseline model fit well and each of the five hybrid models showed small (< 2%) improvement in the full model. Fit

differences occur at backscatter grazing observations where measurement noise is highest. Statistically, these differences provide little improvement to the full MSE[2]. Models 3 and 5 converged to the baseline solution.

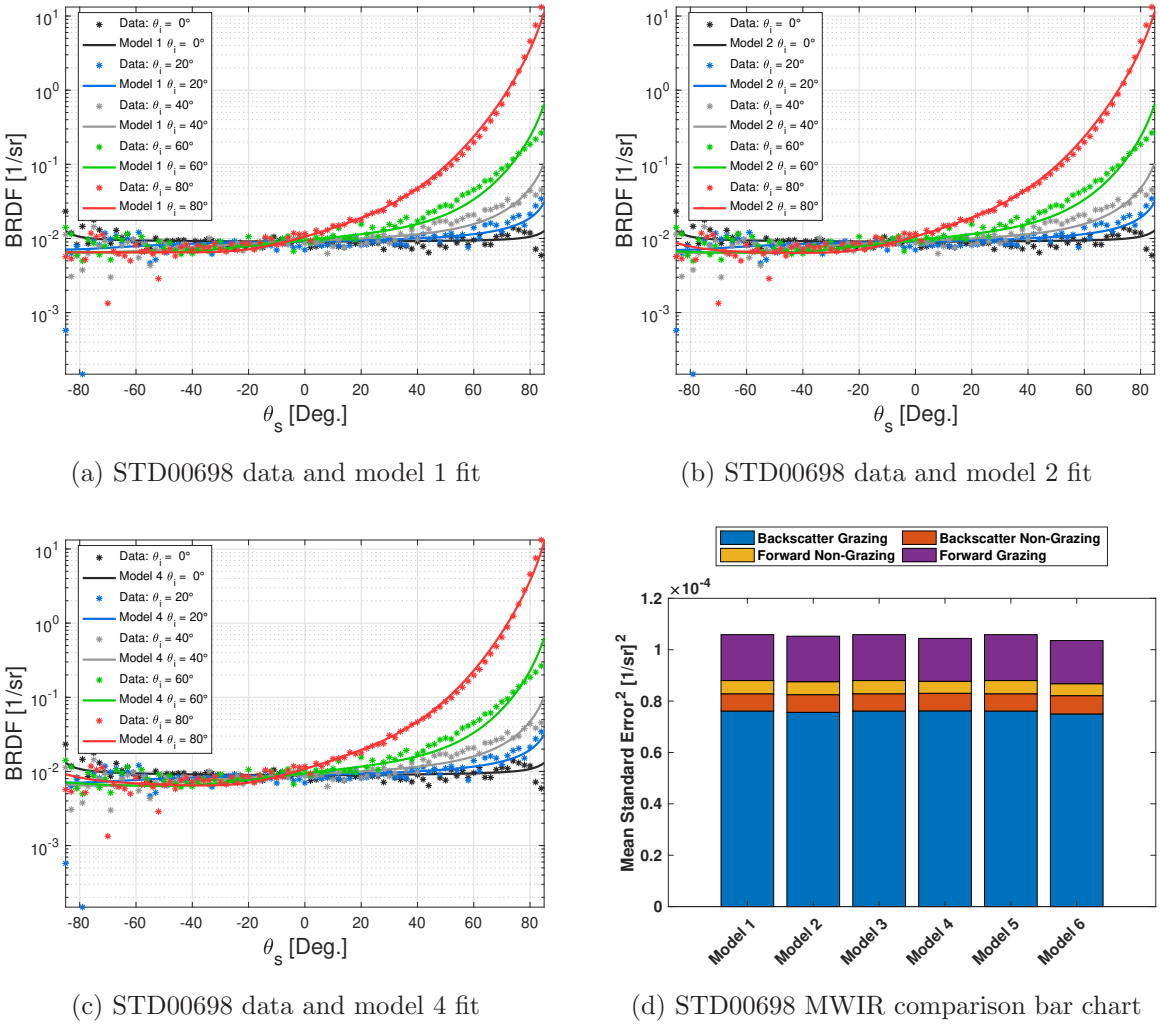

(a) STD00698 data and model 1 fit

(b) STD00698 data and model 2 fit

(c) STD00698 data and model 4 fit

(d) STD00698 MWIR comparison bar chart

Figure 35. Results of STD00698 show model 1 performed well despite the observed backscatter measurement noise. Accordingly, all five hybrid models showed less than 2% full model improvement.

Figure 36 shows a closer look at STD00698 MWIR results with particular attention given to the specular backscatter region.

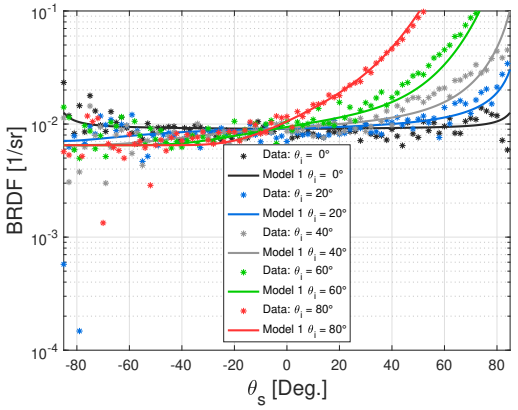

(a) STD00698 data and model 1 fit

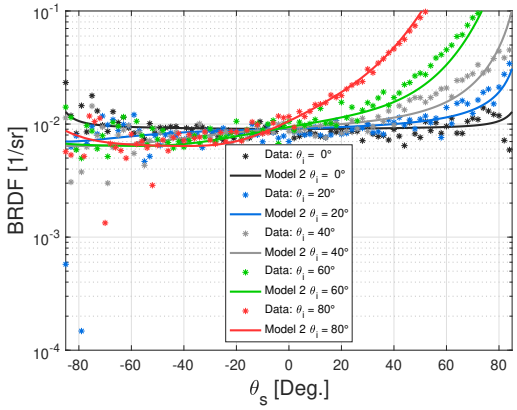

(b) STD00698 data and model 2 fit

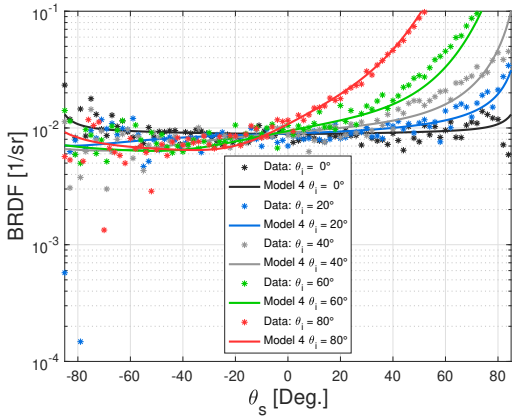

(c) STD00698 data and model 4 fit

Figure 36. A closer look at backscatter results of STD00698 shows the baseline model performed well considering the measurement noise.

Figure 37 shows resulting fits for STD00699. Error in the forward specular region is most significant in the baseline model. This high surface scatter material has low volume scatter, therefore model performance is driven by the model's ability to simulate high surface scatter. Accordingly, minimal improvement is observed in by adding a directional volume scatter term. Model 4 yielded 4% full model improvement and 19% backscatter grazing improvement over the baseline. Model 4 improved backscatter grazing performance for $\theta_i = 80°$, where the material's specular behavior increases. Models 2, 3, and 5 converged to the baseline solution.

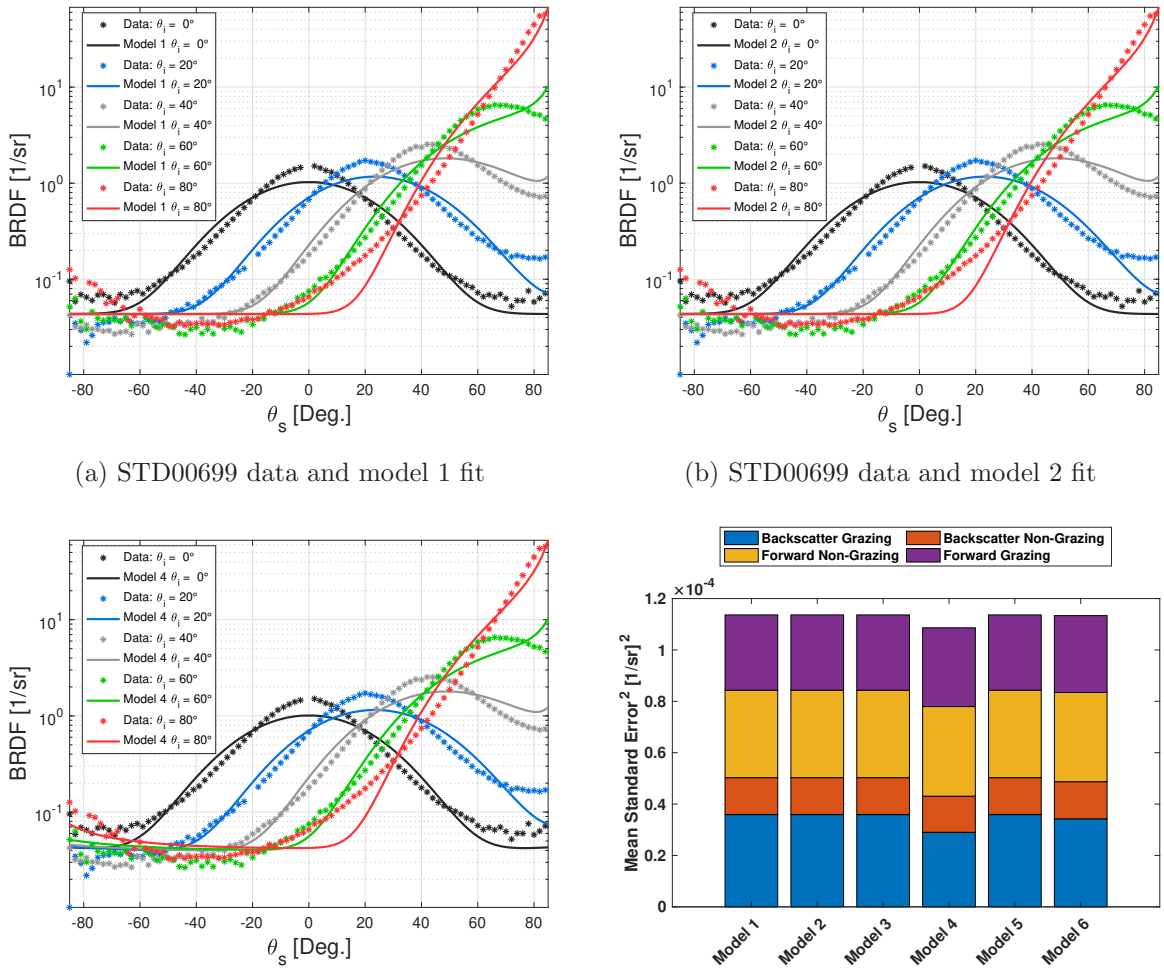

(a) STD00699 data and model 1 fit

(b) STD00699 data and model 2 fit

(c) STD00699 data and model 4 fit

(d) STD00699 MWIR comparison bar chart

Figure 37. Results of STD00699 show model 1 performed well except at large incident angles, where backscatter measurements exhibit non-Lambertian behavior near grazing observations. All models showed minimal full model improvement, each less than 4%. Model 4 yielded the largest improvement in the backscatter grazing region at 19%.

4.4 Summary of Results

The following discussion summarizes the analysis of results presented in Chapter 4. Table 6(a) and 6(b) provide improvement percentages over the baseline (model 1). This is the amount of MSE^2 reduced by the hybrid model relative to the baseline (model 1) MSE^2. Table 6(a) includes all material datasets expected to have high volume scatter components, characterized by a significant off-specular diffuse compo-

nent. Table 6(b) includes all materials exhibiting low volume scatter, characterized by a small diffuse scatter component relative to the forward specular component. Green highlighted values identify statistically significant improvements defined as MSE^2 improvements greater than 10%. Blue identifies results that converged to the baseline (model 1) modified Cook-Torrance solution.

Recall from Chapter 3, model 1 is the baseline model (Cook-Torrance) given by Equation (36) and model 2 given by Equation (71) is the baseline model plus a semi-empirically derived multi-lobe directional volume term. Model 3 given by Equation (72) is the baseline model plus the modified Kubelka-Munk directional volume scatter term. Model 4 given by Equation (73) is the baseline model plus the Beard-Maxwell directional volume term. Model 5 given by Equation (74) is the baseline model plus the Sandford-Robertson directional volume term. Model 6 given by Equation (75) is the baseline model plus the Oren-Nayar directional volume term. Table 5 shows the total number of fit parameters in each model. The hybrid models are similarly parameterized ensuring equitable parameterization for comparison.

Convergence to the baseline solution occurred in 37/75 fits for three reasons. First, recall polished materials have large specular lobes. In glossy materials PNT01006 and PNT01014, off-specular observations greater than $\pm 10^\circ$ show BRDF values that are six orders of magnitude smaller than the specular peak. Fitting to the specular peak is emphasized and structure in the diffuse region is less pronounced. Results show

Model	Number of Parameters
1	5
2	6
3	7
4	6
5	7
6	7

Table 5. The number of parameters in each model are comparable ensuring equitable parameterization across models.

that improvements from adding a volumetric scatter term are less likely for materials with highly specular profiles. The Lambertian diffuse term in the Cook-Torrance model can be a sufficient diffuse description for materials with uniform off-specular profiles.

Second, convergence to the baseline solution is most commonly found in materials with low volume scatter. For these materials, the fit quality is largely determined by the model's surface description. In these materials, a model's directional volume term must help to improve fit quality in forward scatter as well as backscatter otherwise the model is likely to converge to the baseline. Models 3 and 5 showed little impact on forward scatter behavior thus often converged to the baseline.

Third, convergence to the baseline solution can be seen in cases where the directional volume term describes Lambertian scatter in its limiting case. Models 3, 5, and 6 have directional volume scatter terms that converge easily to a Lambertian description. When off-specular measurements are approximately Lambertian, a directional volume scatter term does not improve fit quality.

Convergence to the baseline solution occurs most often in models 3 and 5 which have two of the above characterisitcs: minimal ability to improve forward scatter and a directional volume term with convergence to Lambertian scatter.

Overall, the backscatter region is most positively impacted by a directional volume term. Improvements occur most often for rough surface materials exhibiting high volume scatter. These high volume scatter materials are not highly specular nor approximately Lambertian. Their BRDF profiles vary two to three orders of magnitude over the full observation range and display backscatter peaks at locations where $\theta_s = -\theta_i$. This specular backscatter region was the most dominant source of error in model 1 and was the most impacted region by including a directional volume term.

Models 2 and 6 performed uniquely well at improving full model fit quality. Model

PNT	65 NIR	65 UV	65 VIS	36375 NIR	36495 VIS	01006 NIR
Model 2	50	69	75	24	17	0
Model 3	0	0	0	0	0	1
Model 4	3	67	38	19	14	0
Model 5	3	0	0	0	0	5
Model 6	21	78	61	21	14	0

(a) Full model improvement (%) for high volume scatter materials

PNT	65 MWIR	65 LWIR	66 NIR	66 MWIR	66 UV	01014 NIR	STD00696	STD00698	STD00699
Model 2	9	0	0	0	0	0	0	1	0
Model 3	0	5	6	7	0	0	8	0	0
Model 4	6	0	0	0	2	5	0	1	4
Model 5	0	6	3	13	0	0	7	0	0
Model 6	9	0	0	0	0	0	0	2	0

(b) Full model improvement (%) for low volume scatter materials

Table 6. Models 2, 4, and 6 consistently show statistically significant improvement over the baseline model (model 1) for materials exhibiting high volume scatter. Fit quality improvement by including a directional volume term is minimal for materials with low volume scatter.

2 gave the best fit improvement in 4/6 high volume scatter material datasets. MSE^2 is reduced in 5/6 high volume scatter datasets for an average MSE^2 improvement of 39% over the full observation range and an average of 52% over the backscatter region. The directional volume term's ability to model specular backscatter in model 2 and model 6 added capability lacking in model 1.

Model 6 reduced MSE^2 in 5/6 high volume scatter datasets for an average MSE^2 improvement of 33% over the full observation range and an average of 46% over the backscatter region. Model 4 also showed statistically significant full model improvement in 4/6 high volume scatter datasets with an average improvement of 23%. The Beard-Maxwell directional volume term in model 4 reduced backscatter MSE^2 64% in PNT65 UV and reduced MSE^2 74% in PNT65 VIS. While model 4 did not consistently show the largest full model improvements, it did provide the only statistically

significant forward scatter improvement to any visually specular dataset. However, this improvement is observed at the expense of increased MSE^2 in the backscatter observation region.

All hybrid models showed to be statistically insignificant for improving fit quality in low volume scatter materials. As anticipated, models fit to these materials are reliant on the capability of the surface description for fit quality. As the volume scatter is low, improvements to the volume description are often too insignificant to impact the full model error. Accordingly, 44/45 fits to low volume scatter materials were found to be statistically insignificant. The outlying case occurred for PNT66 MIWR which has relatively large measurement noise in the backscatter region. In this region model 5 converged to a non-Lambertian attenuating backscatter profile and improved the full model fit 13%. These results suggest the addition of a direcitonal volume term is unlikely to improve full model fit quality in low volume scatter materials but may improve backscatter fit quality for non-Lambertian low volume backscatter cases.

Furthermore, improvements are found at large backscatter observation angles. Measurements show BRDF attenuation at low incident angles and BRDF spikes at large incident angles. Accordingly, the Lambertian volume term in model 1 either underestimates or over estimates the BRDF depending on incident angle. Directional volume scatter terms allowed for non-Lambertian backscatter modeling and improved fit quality in this region.

Despite improvements throughout this study, the backscatter region remains a dominant source of remaining error across all materials. Fit error continues to occur in samples with regions of high specular backscatter. While the addition of directional volume scatter terms improved fit quality in this region, existing volume scatter terms provide a gradual fit and continue to underestimate the BRDF at backscatter peaks as seen in PNT65 NIR, PNT65 VIS, PNT65 UV, and PNT36375 results.

It is shown that including a volumetric scatter term can improve overall fit quality in high volume scatter materials 39% over model 1 when model 2 is applied. Improvements can be attributed to improved fit quality in the backscatter region by the model's specular backscatter lobe. Large improvements to fit quality can be gained by including a directional volume scatter term with minimal risk of increasing error in subregions and no risk of increasing total model error. As each term in the hybrid models have independent scale factors, fit quality will not be worse than a model without the directional volume term, but overall fit quality may improve. Applications, such as passive detection of objects predominantly oriented for backscatter observation, will benefit most by including a directional volume scatter term. This is particularly true when the directional volume term in model 2 is used as it performs best to improve specular backscatter model agreement. Aside from the semi-empirically derived term in model 2, the Beard-Maxwell term in model 4 and the Oren-Nayar volume scatter term used in model 6 provide a median solution for fit improvement over a range of diffuse high volume scatter materials for both forward and backscatter observations.

V. Conclusion

Directional volume scatter BRDF models were compared to the Cook-Torrance microfacet model using a two step fit optimization algorithm that recursively identifies a range of local best fit solutions then extracts the relative global best fit. In total, five hybrid models were developed and compared to the baseline Cook-Torrance model (model 1). Model 2 is the baseline model plus a semi-empirically derived multi-lobe directional volume term. Model 3 is the baseline plus the modified Kubelka-Munk directional volume term. Model 4 is the baseline plus the Beard-Maxwell directional volume term. Model 5 is the baseline plus the Sandford-Robertson directional volume term. Model 6 is the baseline plus the Oren-Nayar directional volume term.

The square of the Mean Standard Error (MSE^2) was calculated for the full observation range and presented for each observation region's contribution to the full model error. The Lambertian term in the baseline model consistently over-estimated grazing backscatter observations for low incident angles and under-estimated the BRDF for large incident angles. In general, inclusion of a directional volume term improved grazing backscatter performance and overall fit quality in high volume scatter materials due to its added specular modeling capability. Diffuse scatter measurements are not commonly well approximated by Lambertian scatter, therefore require a directional component that is commonly left out of microfacet models. This indication is particularly true for materials that are not highly specular in forward observations but show specular backscatter behavior. Three exceptions to performance improvements were found where adding a directional volume scatter term did not improve overall fit quality. These exceptions were observed primarily in low volume scatter materials and for materials already well described by the baseline model. As each term in the hybrid models have independent scale factors, fit quality will not be worse than a model without the directional volume term, but overall fit quality may improve.

Maximum fit improvement occurred using model 2 and model 6. Each showed instances of fit error reduction greater than 75%. Models 2 and 6 each showed improved backscatter fit quality in 5/6 high volume scatter datasets for an average of 52% and 46% respectively. Model 4 showed statistically significant reductions to MSE^2 in 4/6 high volume scatter datasets with an average improvement of 23% over the full observation range. In all cases, including a directional volume scatter term can provide improved fit quality with minimal risk of increasing sub-region error and no risk of increasing full model MSE^2. Applications such as passive detection of objects in backscatter geometries will benefit most by including a directional volume scatter term.

A number of additional topics of interest came from this work and should be considered for future work including:

- Parameter wavelength and incident angle scaling
- Butler Fresnel correction validity in directional volume scatter models
- Application of the Roujean directional volume term in the microfacet model
- Anchoring MSE improvements to 3-D rendered observations
- Physical volume model development based on Rayleigh scatter

Foremost of these topics is the investigation of parameter scaling. Measurements anchoring model parameters and incident wavelength largely impact model parameters. Parameter scaling between illumination wavelengths cannot be assumed to be linear. Similarly, linking parameters with specific materials can only be reliably done once measurements are made over a large number of incident angles. Otherwise, there is potential for the parameter to be biased toward a specific incident angle and observation configuration. Another valuable extension of this thesis would be application

of the Butler Fresnel approximation [18] to directional volumetric scatter terms, not just the surface scatter term. Results may improve fit quality in the remaining dominant error region and may change which directional volume scatter model provides the best fit quality improvement. Also, further investigation of the Roujean model outlined in Chapters 2 and 3 may show additional directional volume scatter performance that is capable of addressing the shortcomings identified through this study. An alternate optimization algorithm or further analysis of its parameter dependencies may provide a path for comparison against the results presented here. additionally, rendering of the results presented in this thesis would be beneficial to strategic level mission planners as well as the graphics rendering community. Observed MSE improvements greater than 75% may significantly alter what is graphically rendered and has potential to increase observation clarity for the end user. Finally, with the extent of microfacet directional volume models outlined in this work, progress toward a physical volume model can be made. Investigation of a directional volume model that exploits the known dynamics of Rayleigh scatter is well warranted.

This study takes the first steps toward a comprehensive BRDF model using in-depth analysis of directional volumetric scatter terms. Resulting contributions of this thesis work includes: (1) development of a multi-lobe semi-empirical directional volumetric term, (2) robust categorization of several directional volume scatter models for several materials and wavelengths, (3) hybrid model development and comparison to the Cook-Torrance model, (4) validation of directional volume scatter term significance in BRDF modeling, (5) identification of need for a Rayleigh-based physical BDRF model, and (6) Correction to the Yang modified Kubelka-Munk model. Ultimately, a predictive physical BRDF model that is wavelength scalable and is accurate for a range of material types is desired, this research lays the initial directional volumetric scatter work necessary to achieve that objective.

Appendix A. All Fitted Models

This appendix provides all resulting model fits for each material at each illumination wavelength. This includes those not provided in Chapter 4, such as solutions equivalent to the baseline model (model 1), and fits that did not add exceptional value to the results discussion. For highly specular materials or materials with overlapping backscatter peaks, an additional set of scaled plots is provided to more clearly see the fit quality in the specular backscatter region.

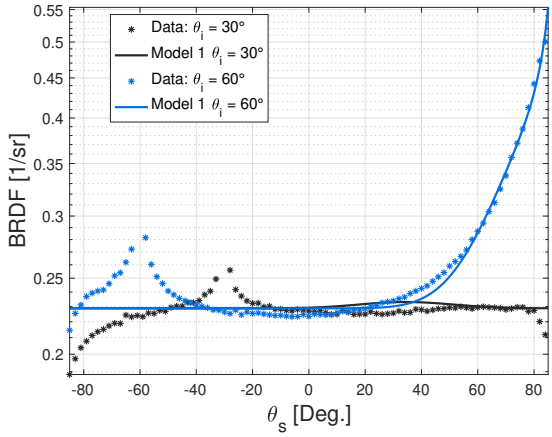

(a) PNT65 NIR measurements and model 1 fit

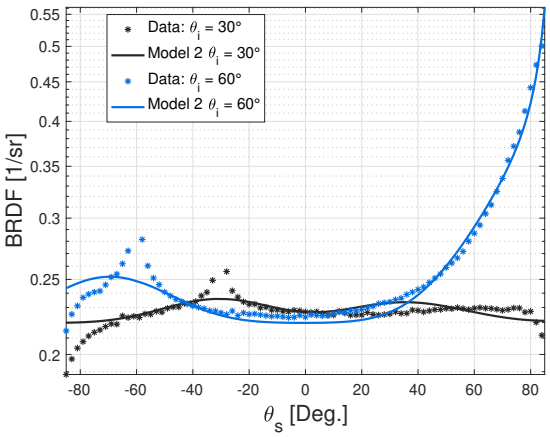

(b) PNT65 NIR measurements and model 2 fit

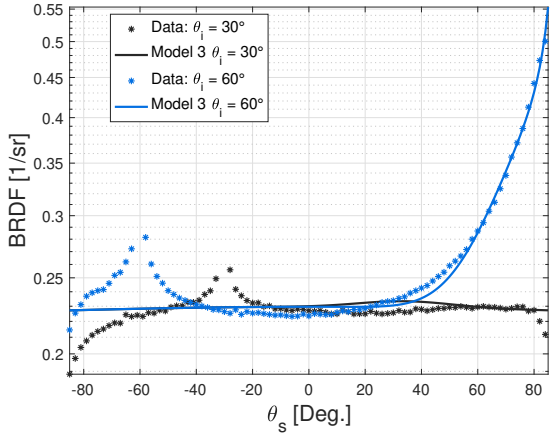

(c) PNT65 NIR measurements and model 3 fit

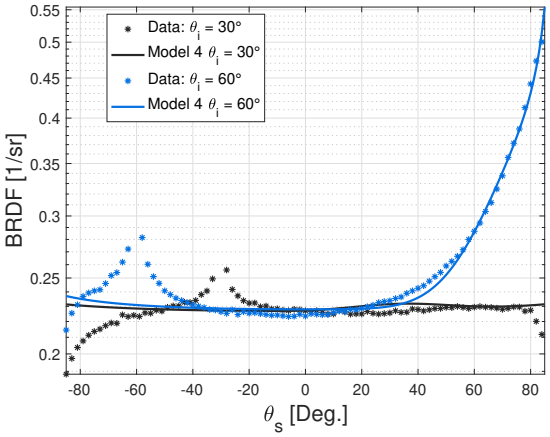

(d) PNT65 NIR measurements and model 4 fit

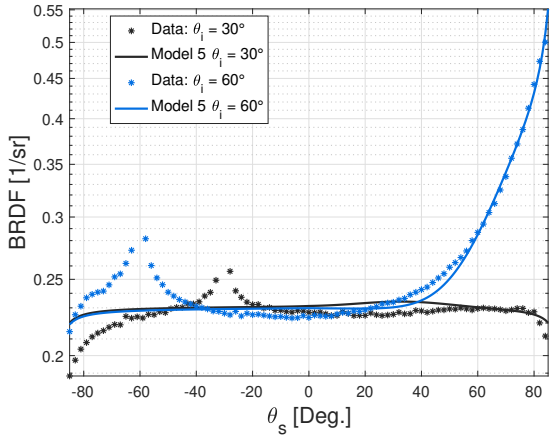

(e) PNT65 NIR measurements and model 5 fit

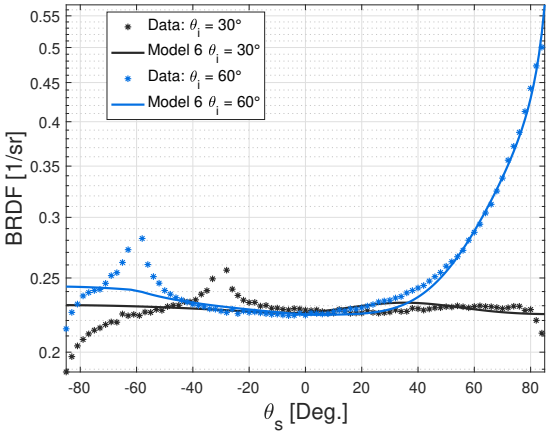

(f) PNT65 NIR measurements and model 6 fit

Figure 38. Resulting six models fit to diffuse paint PNT65 illuminated by a NIR source.

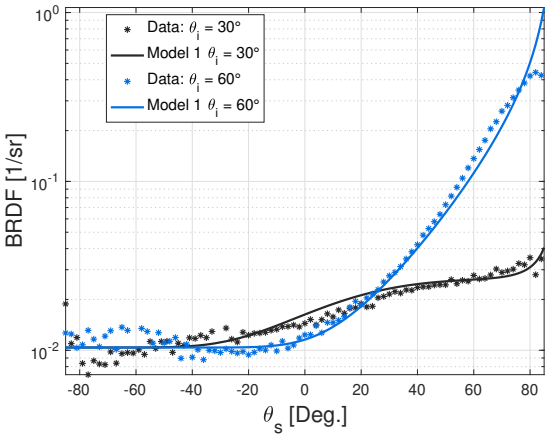

(a) PNT65 MWIR measurements and model 1 fit

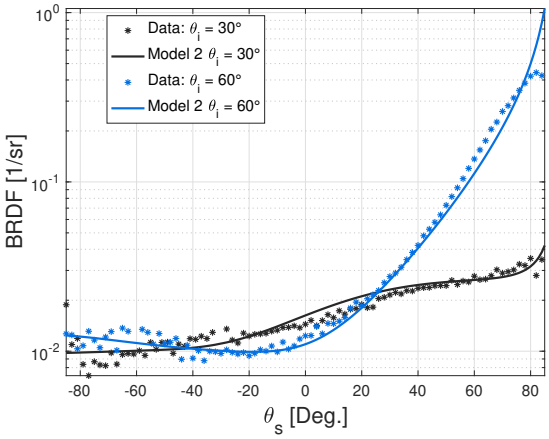

(b) PNT65 MWIR measurements and model 2 fit

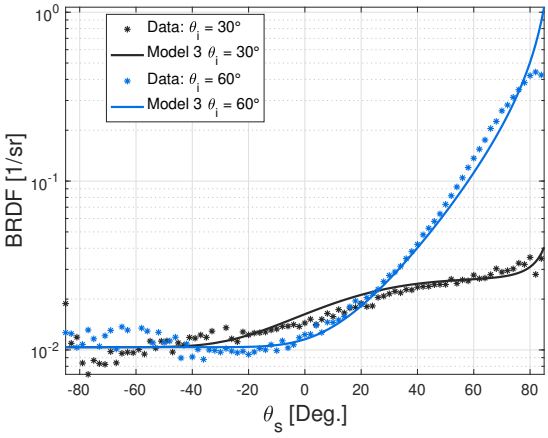

(c) PNT65 MWIR measurements and model 3 fit

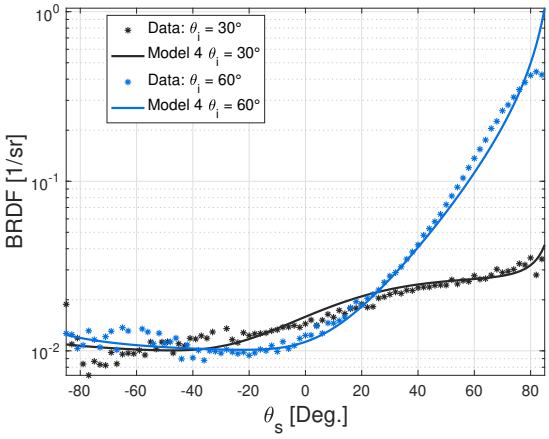

(d) PNT65 MWIR measurements and model 4 fit

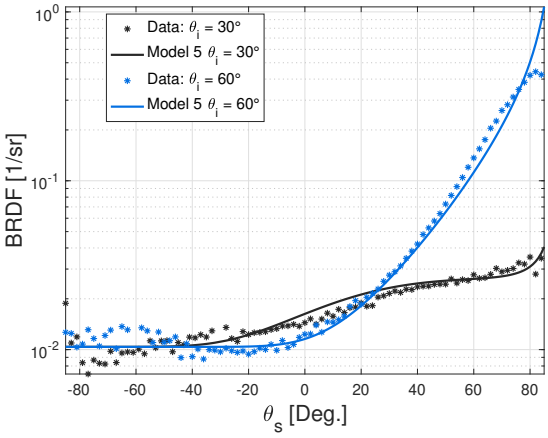

(e) PNT65 MWIR measurements and model 5 fit

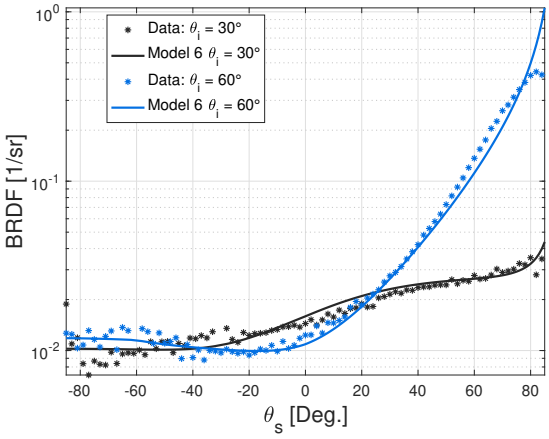

(f) PNT65 MWIR measurements and model 6 fit

Figure 39. Resulting six models fit to diffuse paint PNT65 illuminated by a MWIR source.

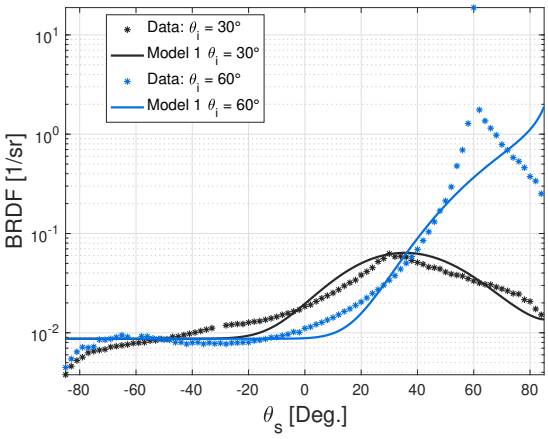

(a) PNT65 LWIR measurements and model 1 fit

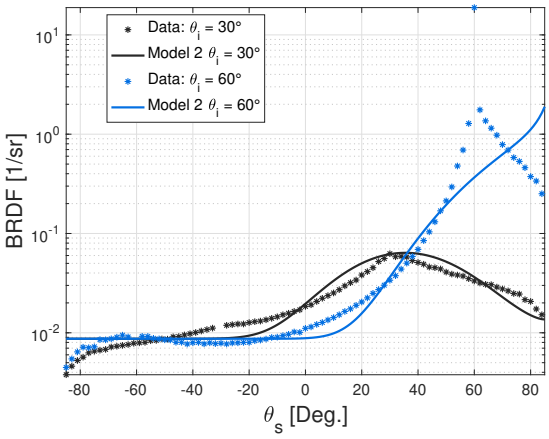

(b) PNT65 LWIR measurements and model 2 fit

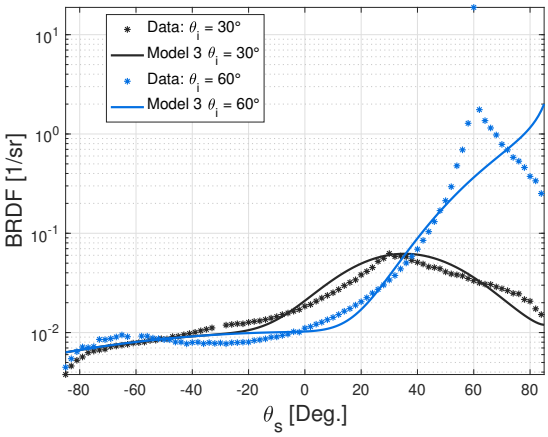

(c) PNT65 LWIR measurements and model 3 fit

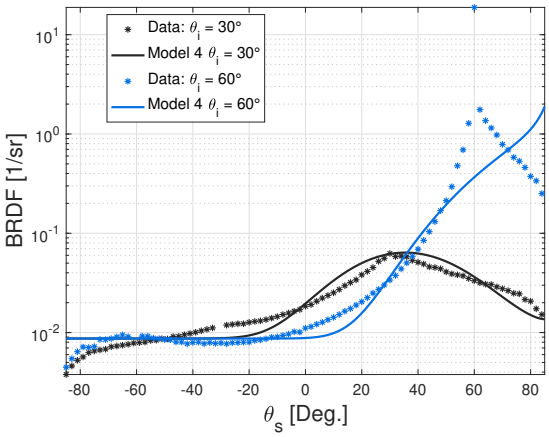

(d) PNT65 LWIR measurements and model 4 fit

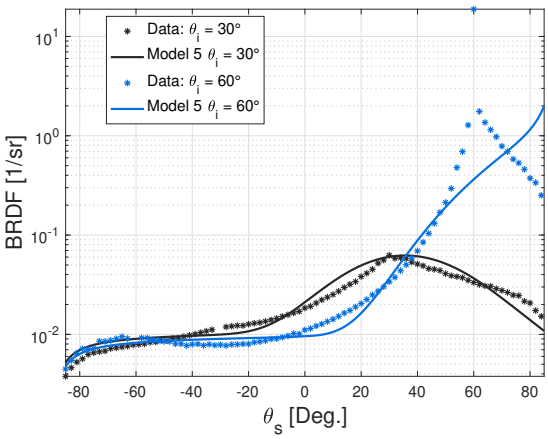

(e) PNT65 LWIR measurements and model 5 fit

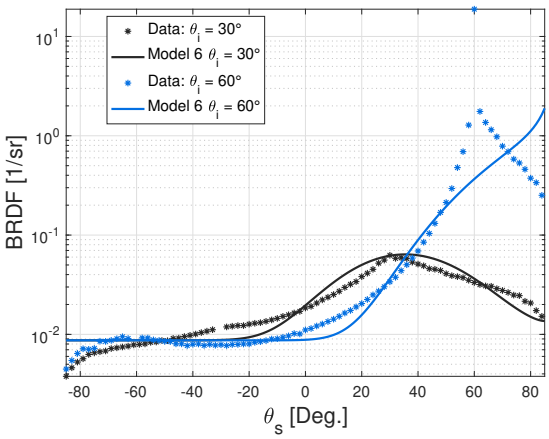

(f) PNT65 LWIR measurements and model 6 fit

Figure 40. Resulting six models fit to diffuse paint PNT65 illuminated by a LWIR source.

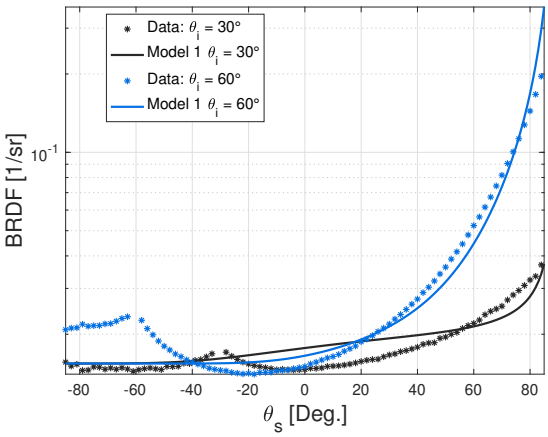

(a) PNT65 UV measurements and model 1 fit

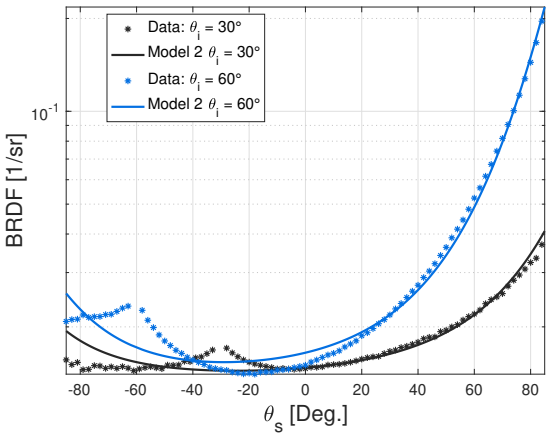

(b) PNT65 UV measurements and model 2 fit

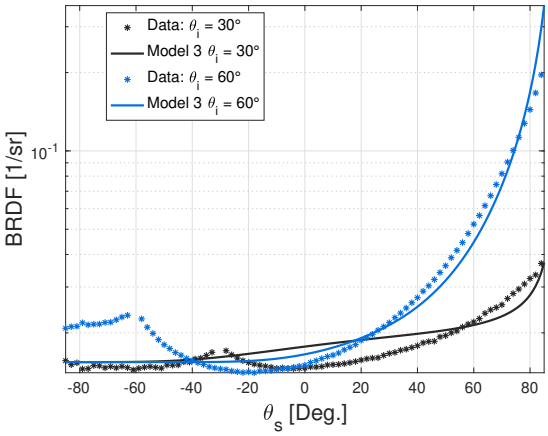

(c) PNT65 UV measurements and model 3 fit

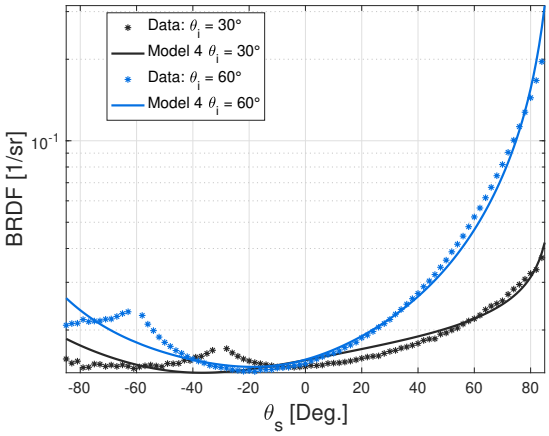

(d) PNT65 UV measurements and model 4 fit

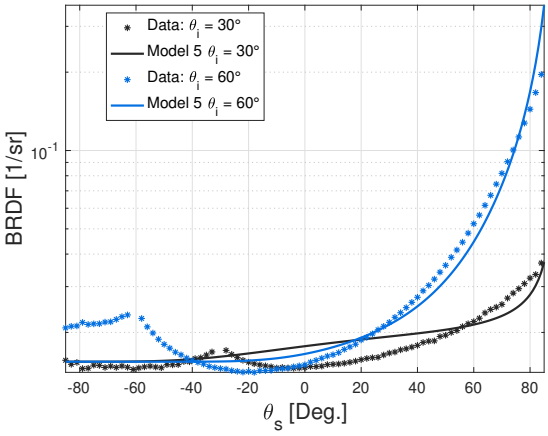

(e) PNT65 UV measurements and model 5 fit

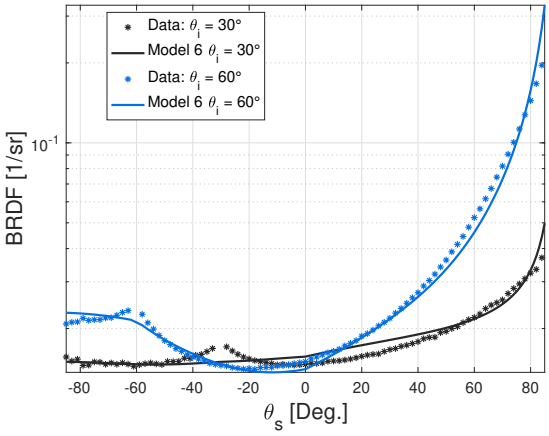

(f) PNT65 UV measurements and model 6 fit

Figure 41. Resulting six models fit to diffuse paint PNT65 illuminated by an UV source.

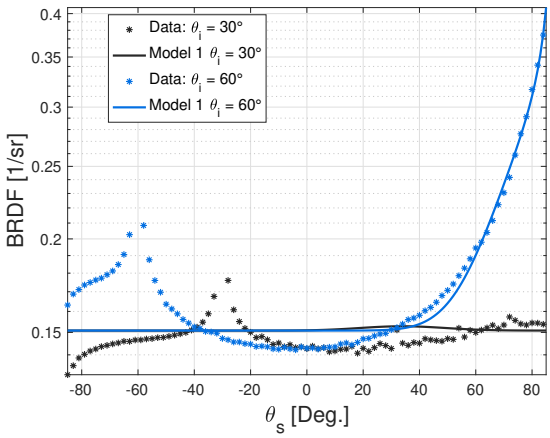

(a) PNT65 VIS measurements and model 1 fit

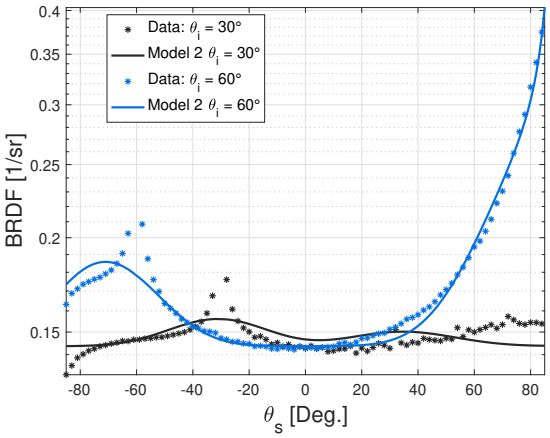

(b) PNT65 VIS measurements and model 2 fit

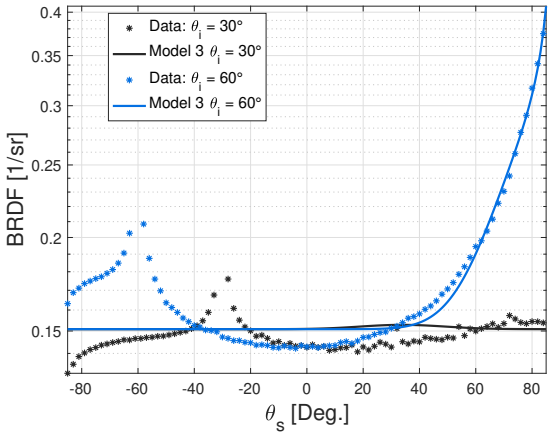

(c) PNT65 VIS measurements and model 3 fit

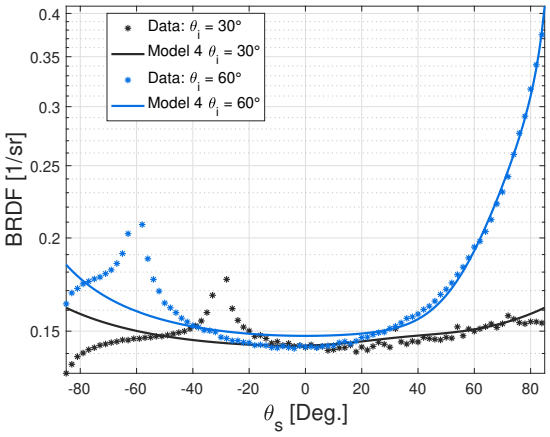

(d) PNT65 VIS measurements and model 4 fit

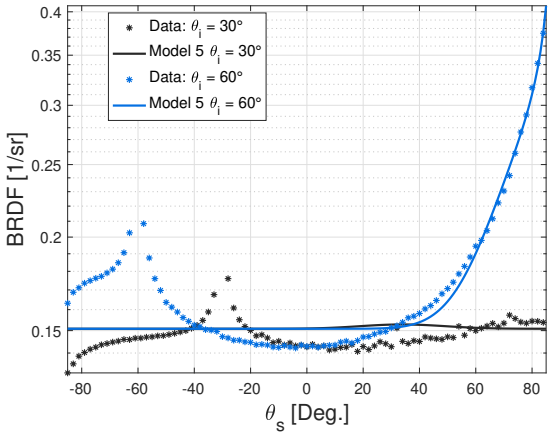

(e) PNT65 VIS measurements and model 5 fit

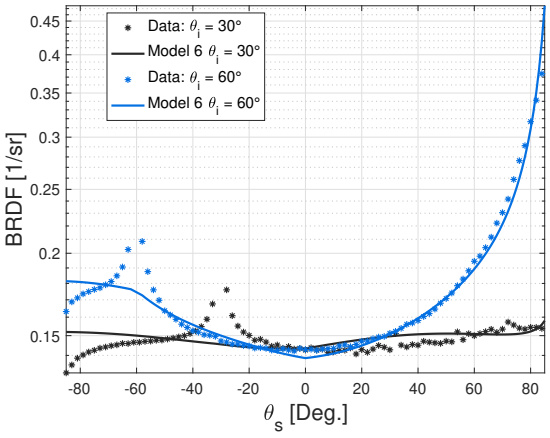

(f) PNT65 VIS measurements and model 6 fit

Figure 42. Resulting six models fit to diffuse paint PNT65 illuminated by a VIS source.

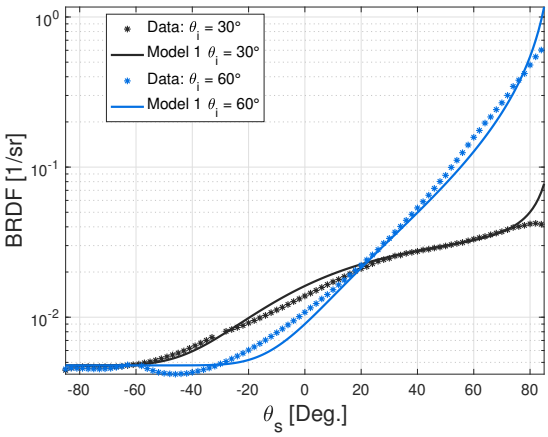

(a) PNT66 NIR measurements and model 1 fit

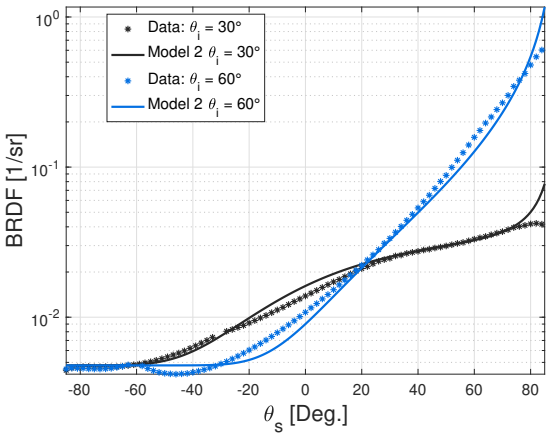

(b) PNT66 NIR measurements and model 2 fit

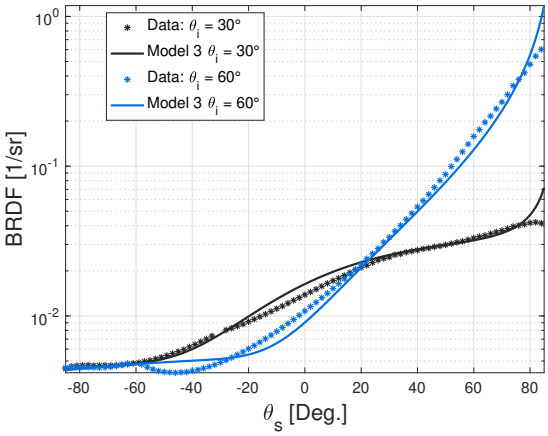

(c) PNT66 NIR measurements and model 3 fit

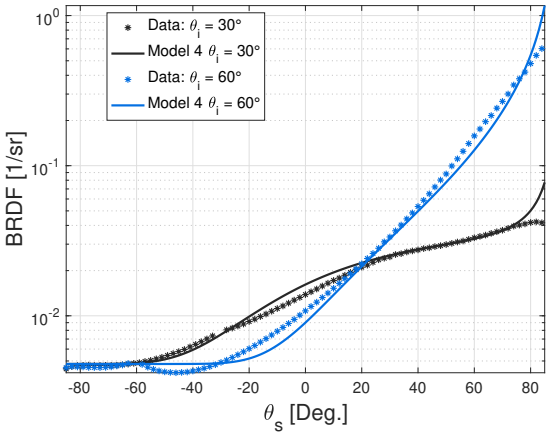

(d) PNT66 NIR measurements and model 4 fit

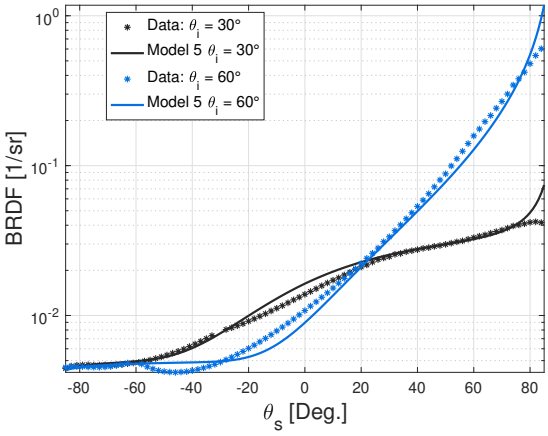

(e) PNT66 NIR measurements and model 5 fit

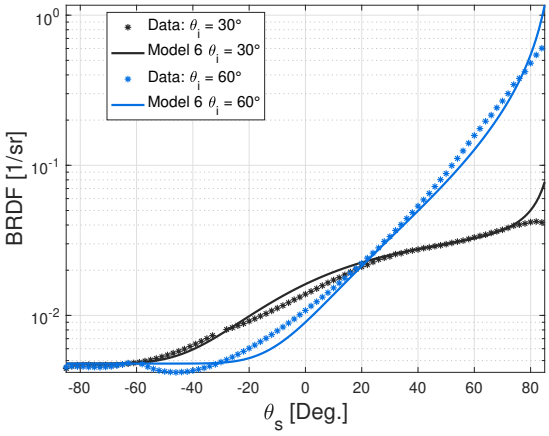

(f) PNT66 NIR measurements and model 6 fit

Figure 43. Resulting six models fit to diffuse paint PNT66 illuminated by a NIR source

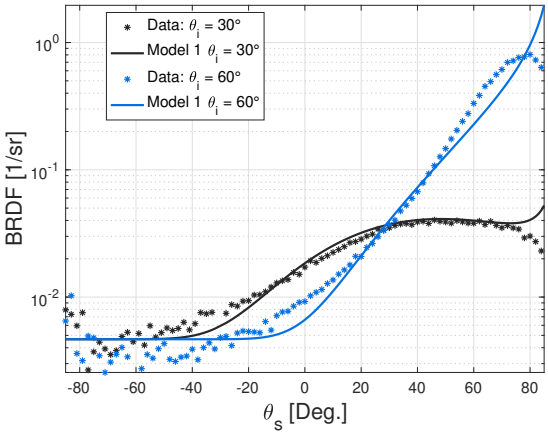

(a) PNT66 MWIR measurements and model 1 fit

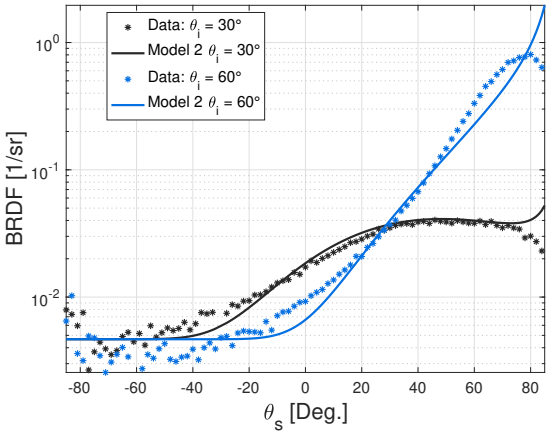

(b) PNT66 MWIR measurements and model 2 fit

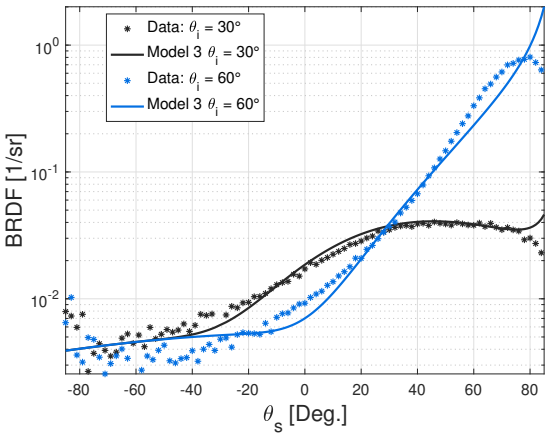

(c) PNT66 MWIR measurements and model 3 fit

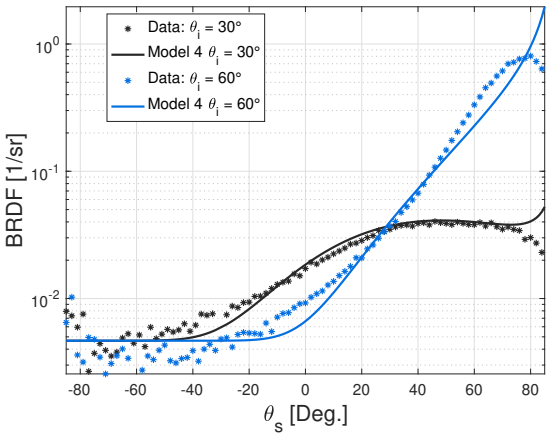

(d) PNT66 MWIR measurements and model 4 fit

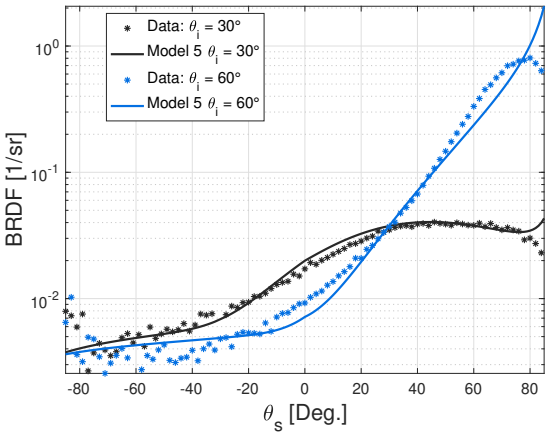

(e) PNT66 MWIR measurements and model 5 fit

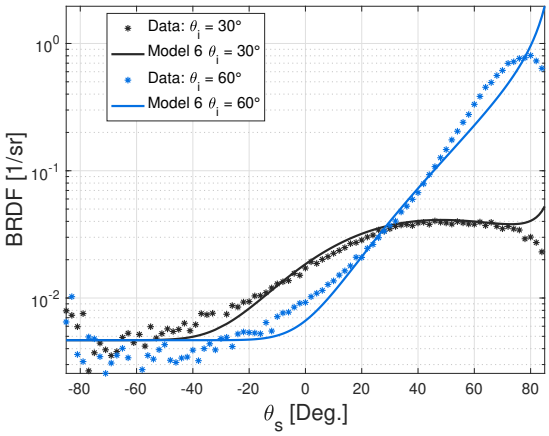

(f) PNT66 MWIR measurements and model 6 fit

Figure 44. Resulting six models fit to diffuse paint PNT66 illuminated by a MWIR source.

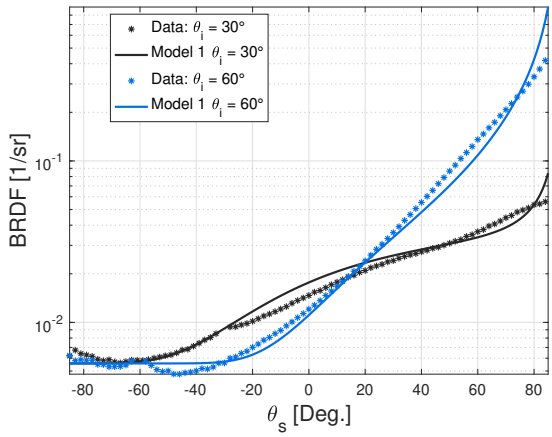

(a) PNT66 UV measurements and model 1 fit

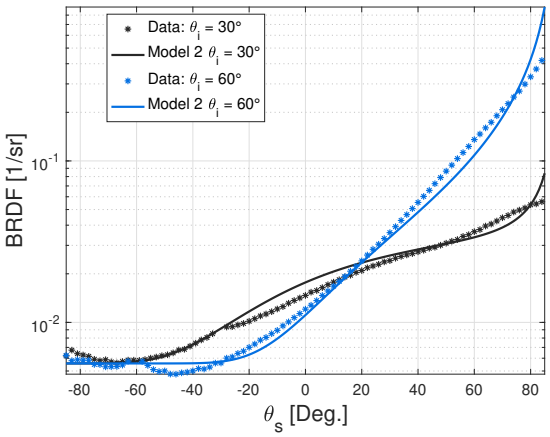

(b) PNT66 UV measurements and model 2 fit

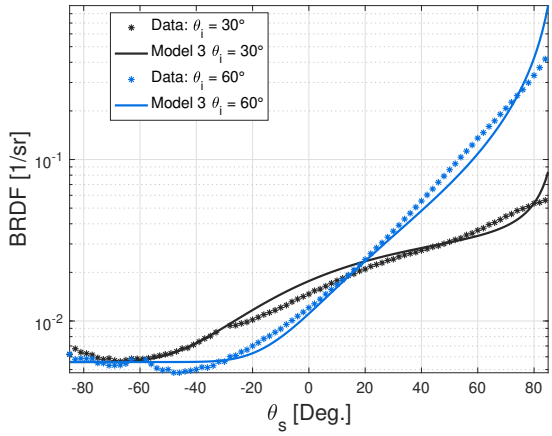

(c) PNT66 UV measurements and model3 fit

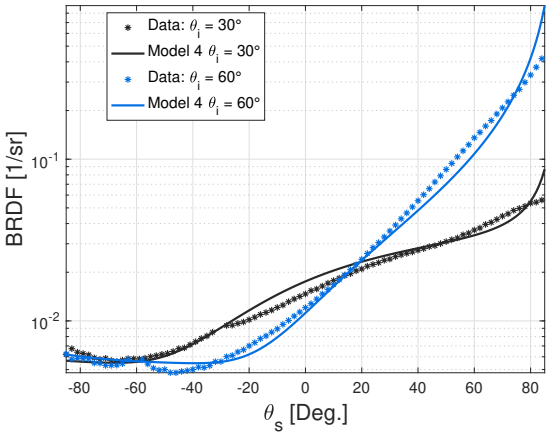

(d) PNT66 UV measurements and model 4 fit

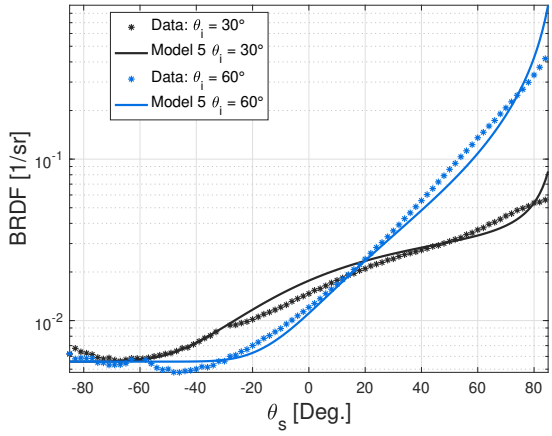

(e) PNT66 UV measurements and model 5 fit

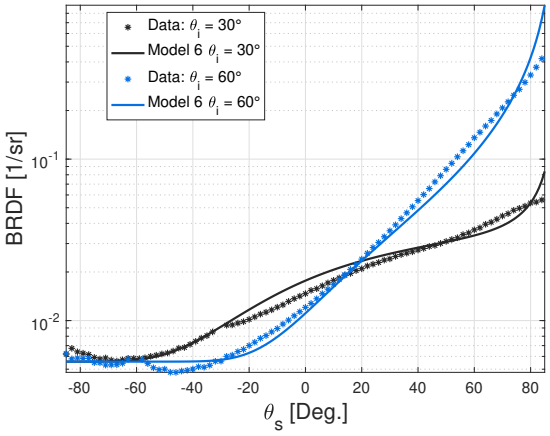

(f) PNT66 UV measurements and model 6 fit

Figure 45. Resulting six models fit to diffuse paint PNT66 illuminated by an UV source.

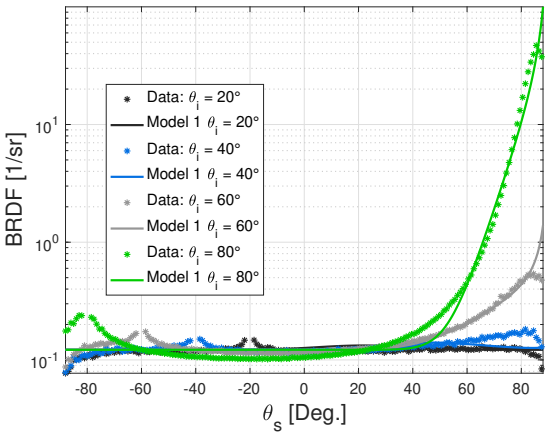

(a) PNT36375 measurements and model 1 fit

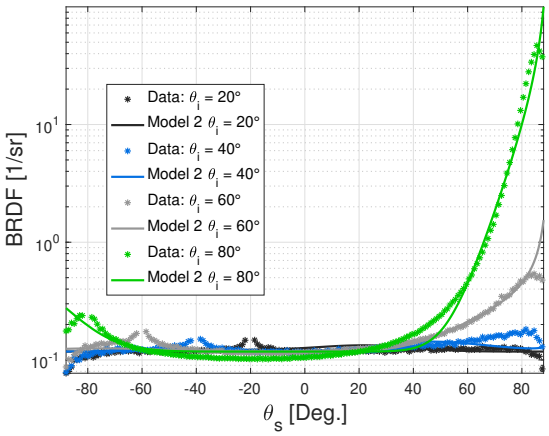

(b) PNT36375 measurements and model 2 fit

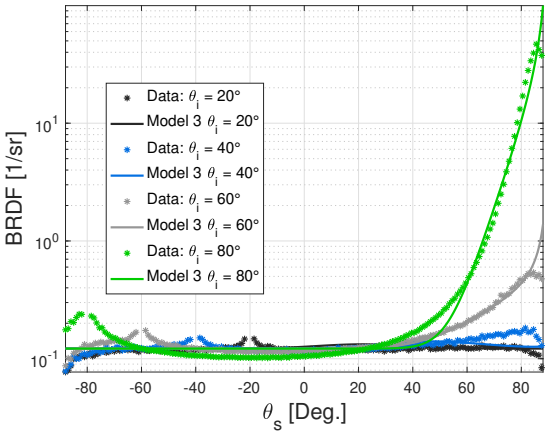

(c) PNT36375 measurements and model 3 fit

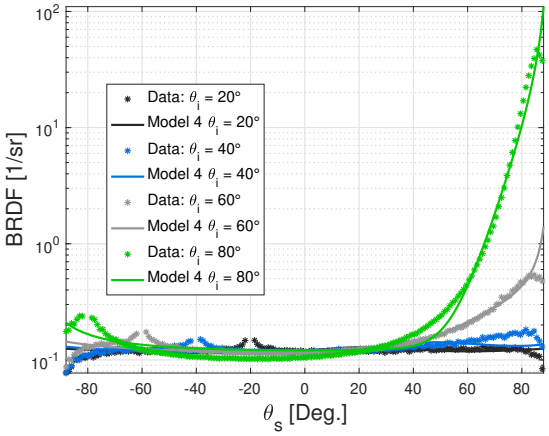

(d) PNT36375 measurements and model 4 fit

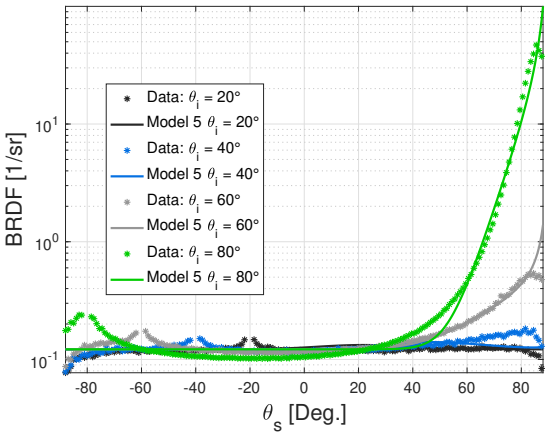

(e) PNT36375 measurements and model 5 fit

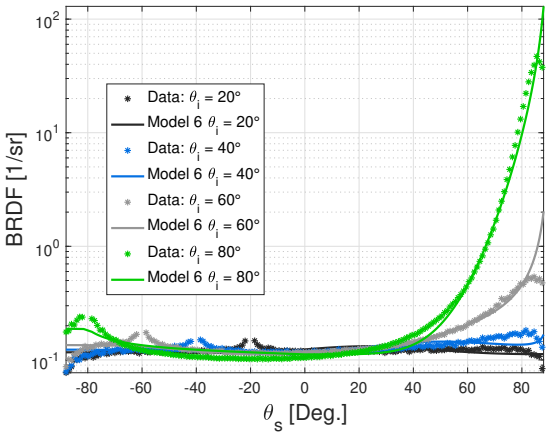

(f) PNT36375 measurements and model 6 fit

Figure 46. Resulting six models fit to diffuse paint PNT36375 illuminated by a NIR source.

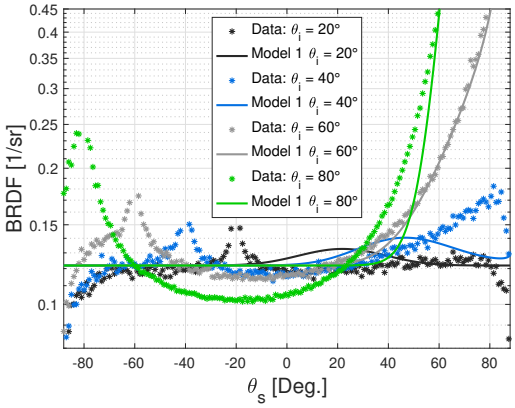

(a) PNT36375 measurements and model 1 fit

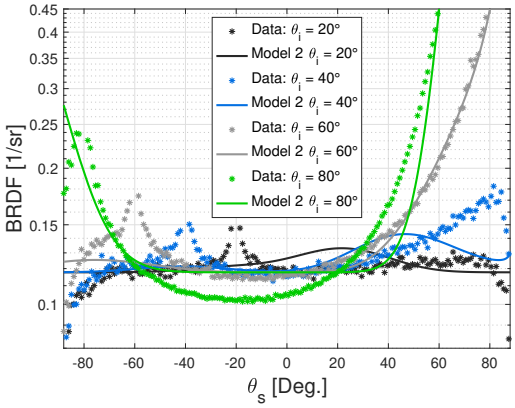

(b) PNT36375 measurements and model 2 fit

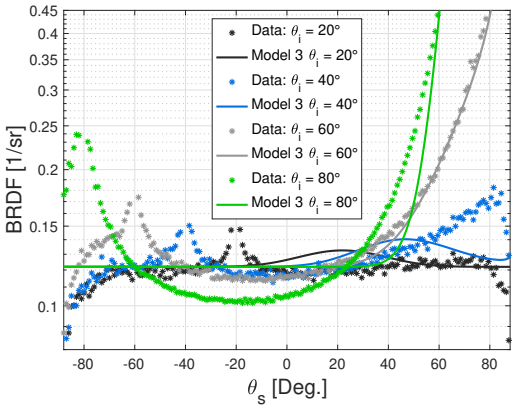

(c) PNT36375 measurements and model 3 fit

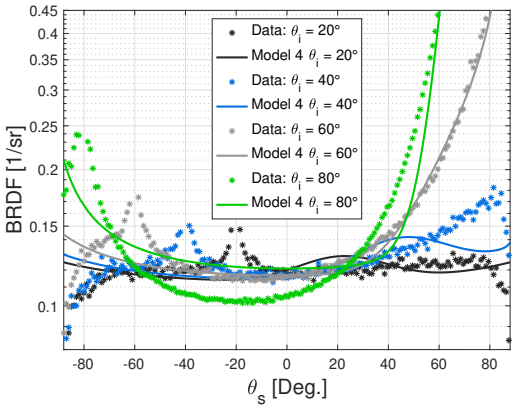

(d) PNT36375 measurements and model 4 fit

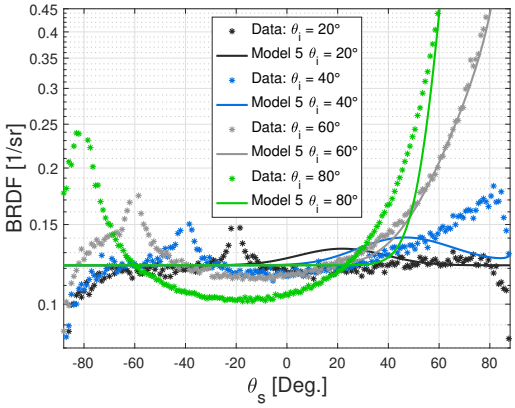

(e) PNT36375 measurements and model 5 fit

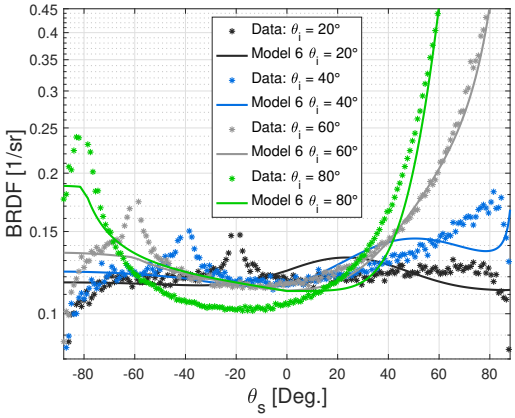

(f) PNT36375 measurements and model 6 fit

Figure 47. All PNT36375 NIR Backscatter Results

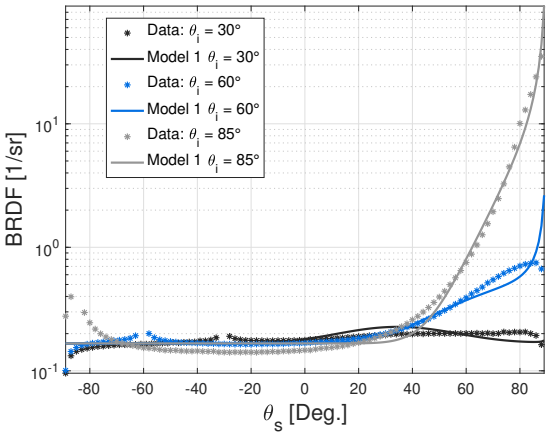

(a) PNT36495 measurements and model 1 fit

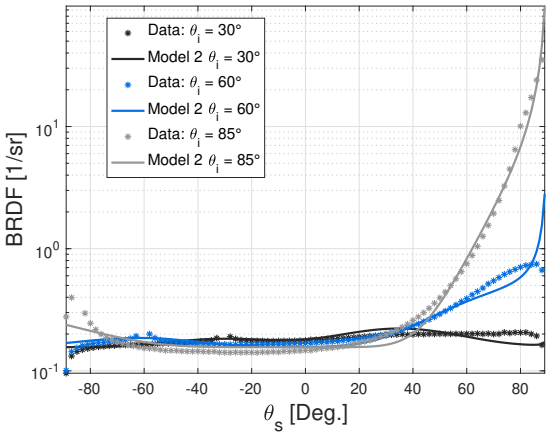

(b) PNT36495 measurements and model 2 fit

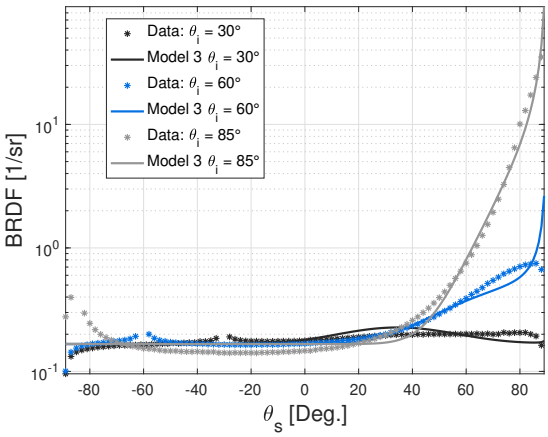

(c) PNT36495 measurements and model 3 fit

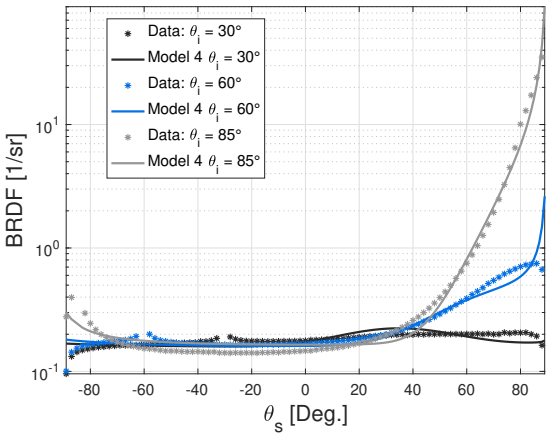

(d) PNT36495 measurements and model 4 fit

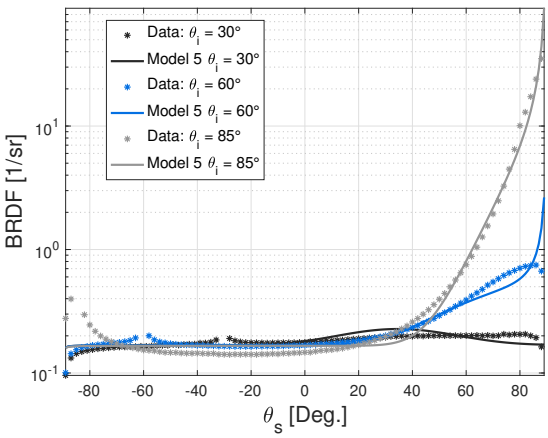

(e) PNT36495 measurements and model 5 fit

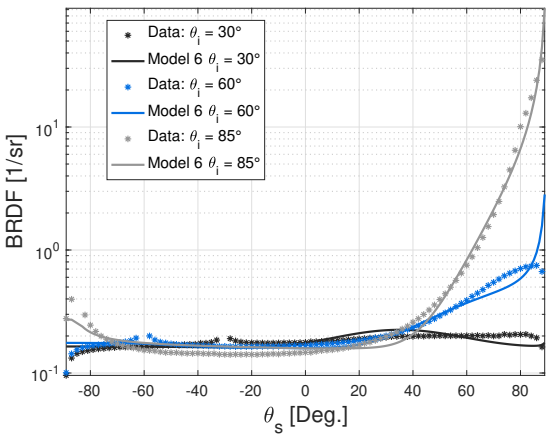

(f) PNT36495 measurements and model 6 fit

Figure 48. Resulting six models fit to diffuse paint PNT36495 illuminated by a VIS source.

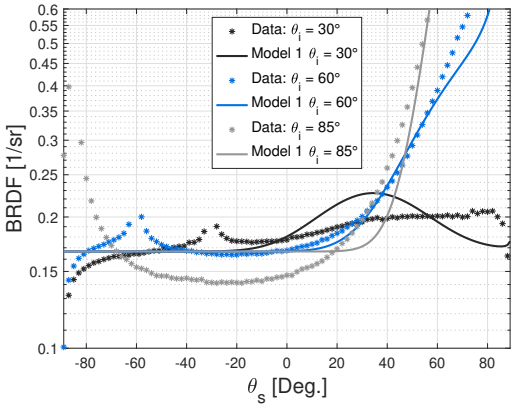

(a) PNT36495 measurements and model 1 fit

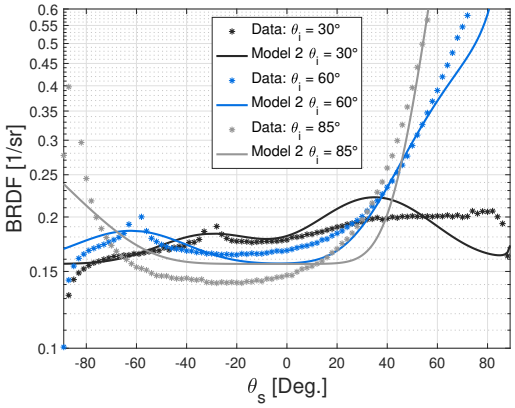

(b) PNT36495 measurements and model 2 fit

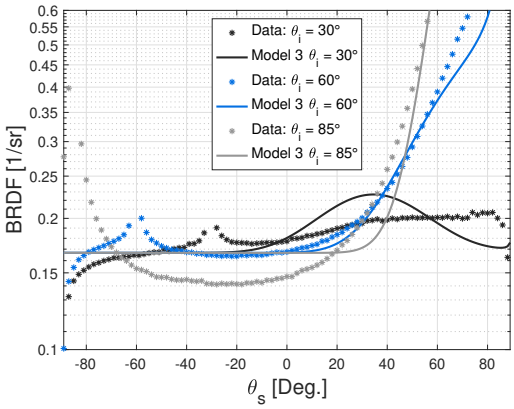

(c) PNT36495 measurements and model 3 fit

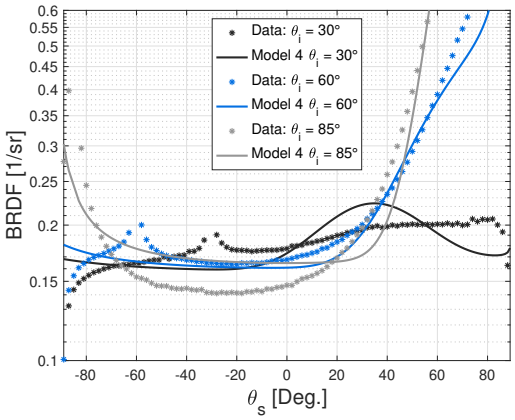

(d) PNT36495 measurements and model 4 fit

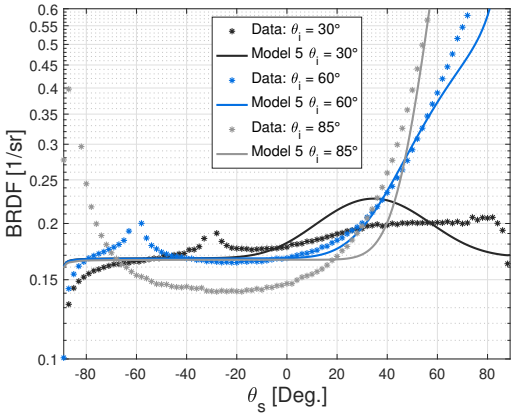

(e) PNT36495 measurements and model 5 fit

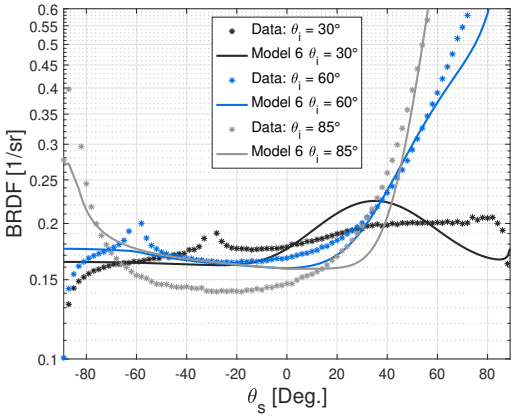

(f) PNT36495 measurements and model 6 fit

Figure 49. All PNT36495 VIS Backscatter Results

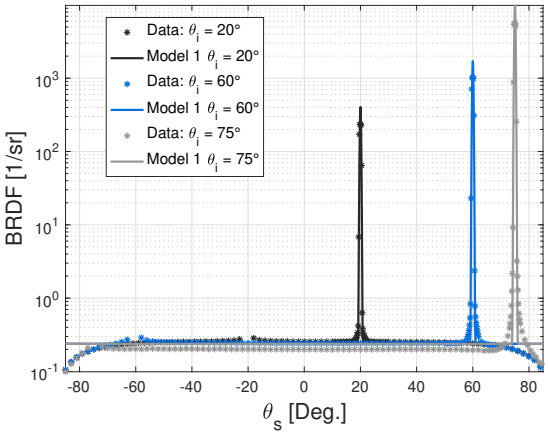

(a) PNT01006 measurements and model 1 fit

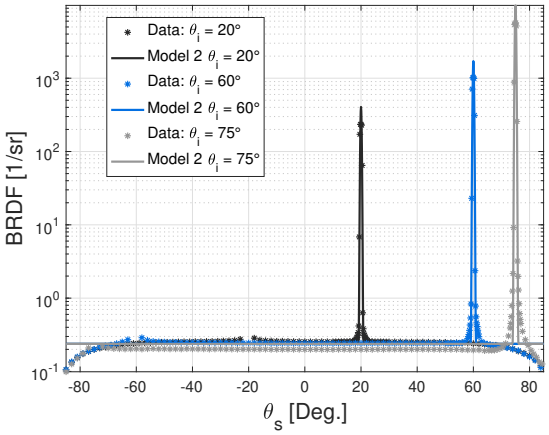

(b) PNT01006 measurements and model 2 fit

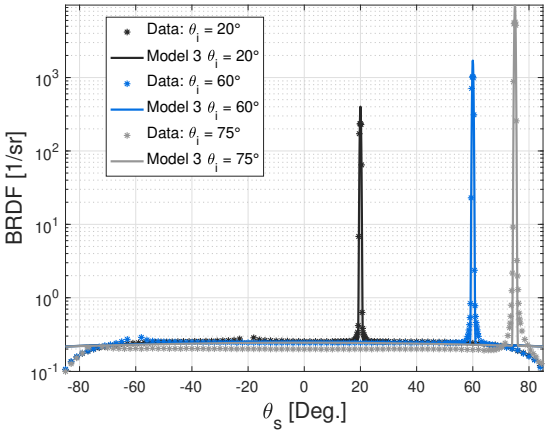

(c) PNT01006 measurements and model 3 fit

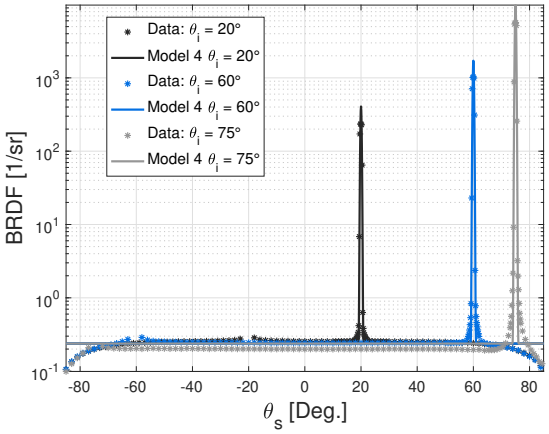

(d) PNT01006 measurements and model 4 fit

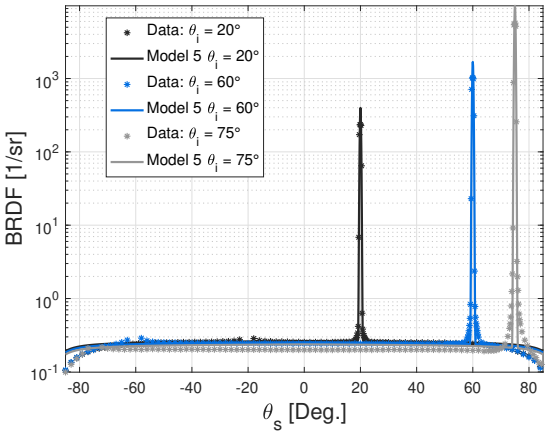

(e) PNT01006 measurements and model 5 fit

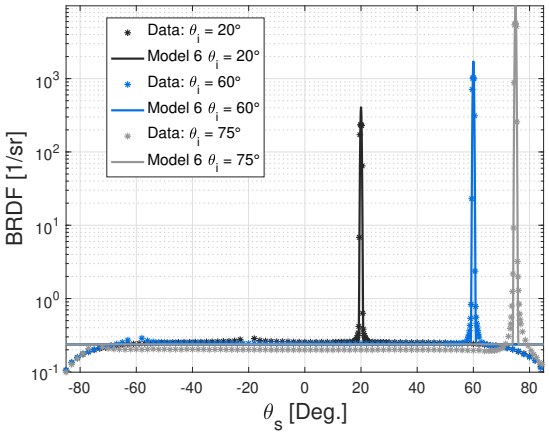

(f) PNT01006 measurements and model 6 fit

Figure 50. Resulting six models fit to glossy paint PNT01006 illuminated by a NIR source.

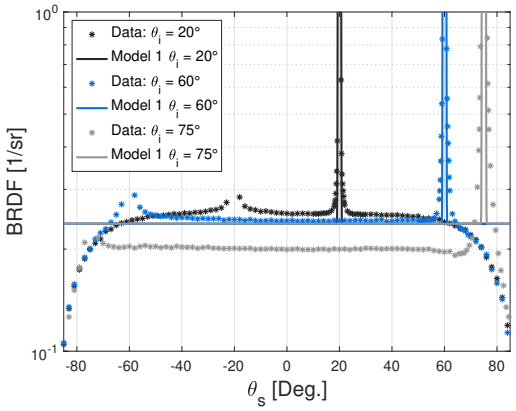

(a) PNT01006 measurements and model 1 fit

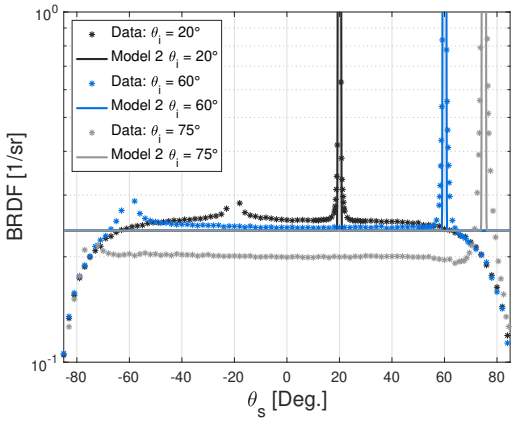

(b) PNT01006 measurements and model 2 fit

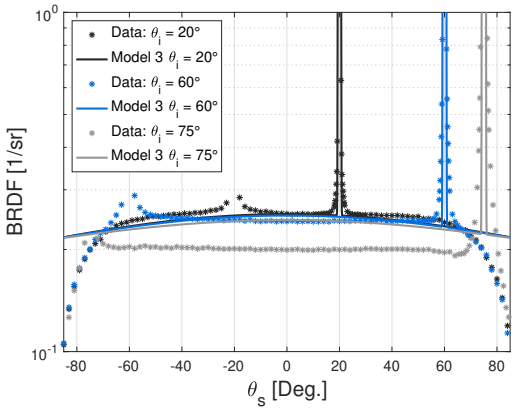

(c) PNT01006 measurements and model 3 fit

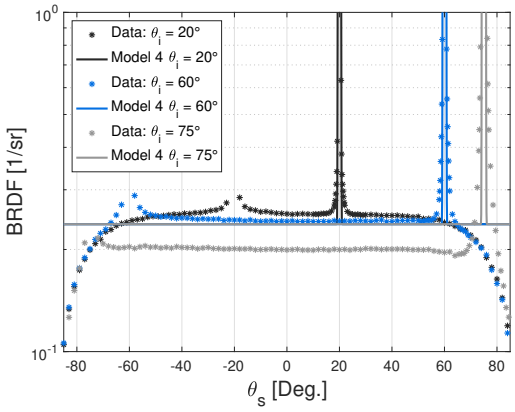

(d) PNT01006 measurements and model 4 fit

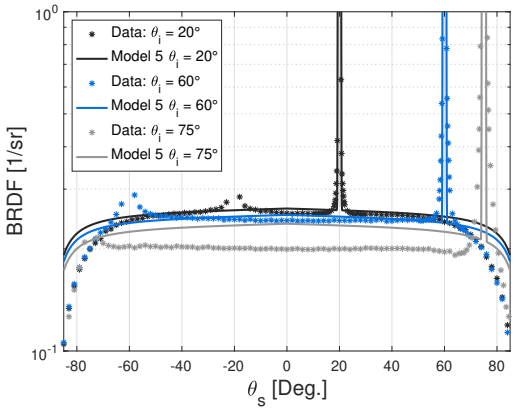

(e) PNT01006 measurements and model 5 fit

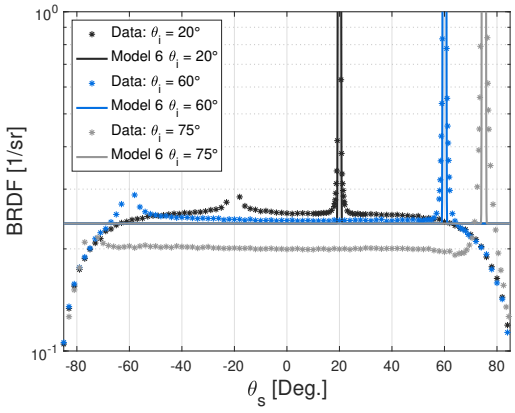

(f) PNT01006 measurements and model 6 fit

Figure 51. All PNT01006 NIR Backscatter Results

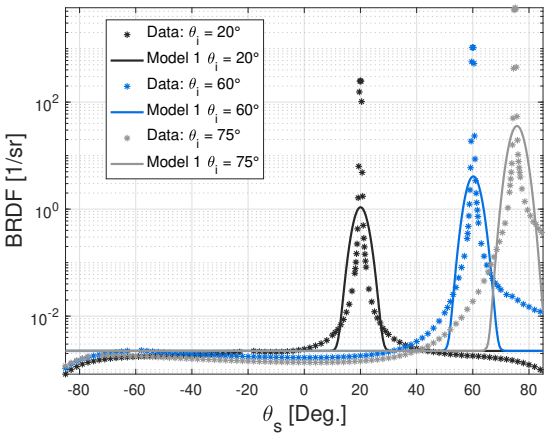

(a) PNT01014 measurements and model 1 fit

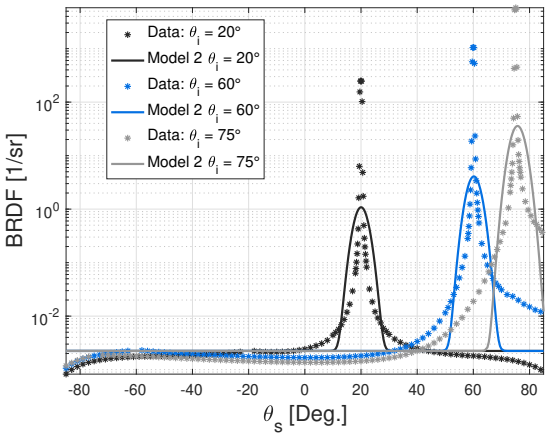

(b) PNT01014 measurements and model 2 fit

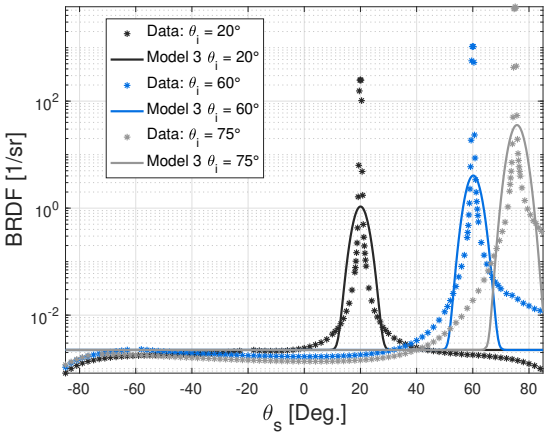

(c) PNT01014 measurements and model 3 fit

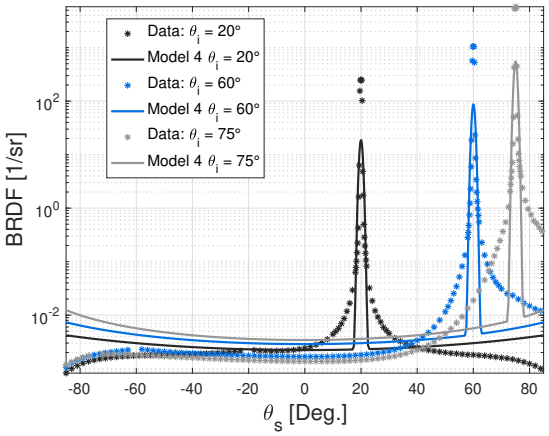

(d) PNT01014 measurements and model 4 fit

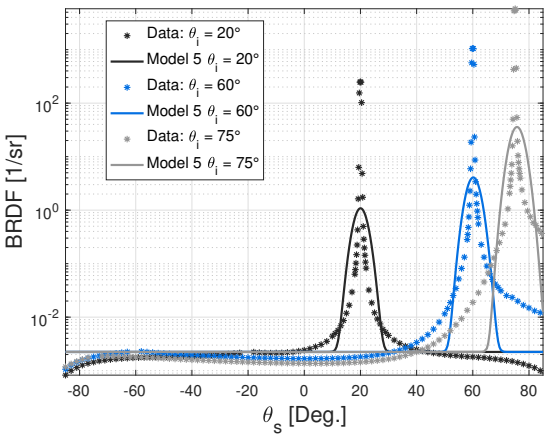

(e) PNT01014 measurements and model 5 fit

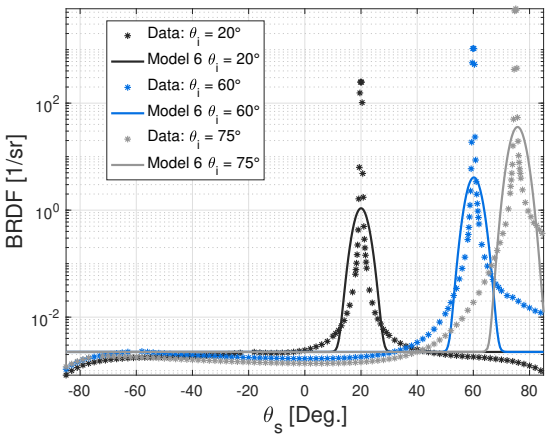

(f) PNT01014 measurements and model 6 fit

Figure 52. Resulting six models fit to glossy paint PNT01014 illuminated by a NIR source.

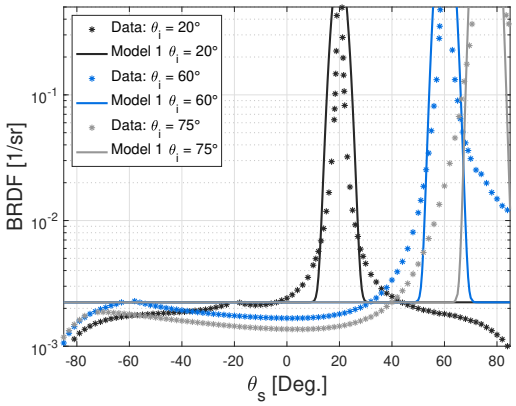

(a) PNT01014 measurements and model 1 fit

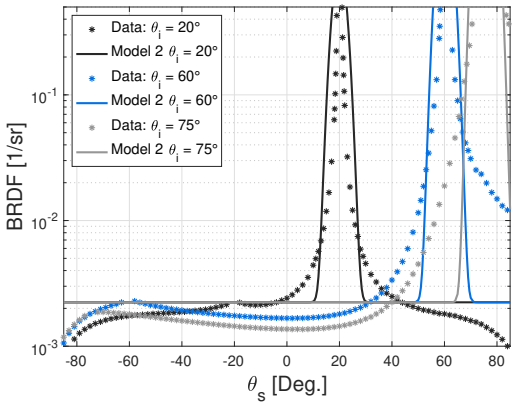

(b) PNT01014 measurements and model 2 fit

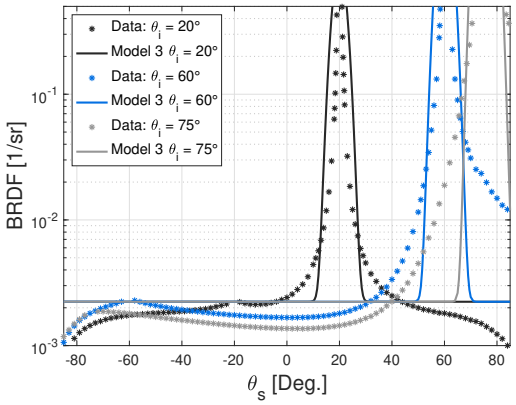

(c) PNT01014 measurements and model 3 fit

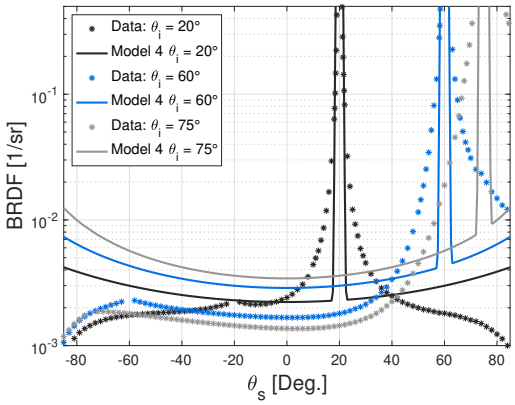

(d) PNT01014 measurements and model 4 fit

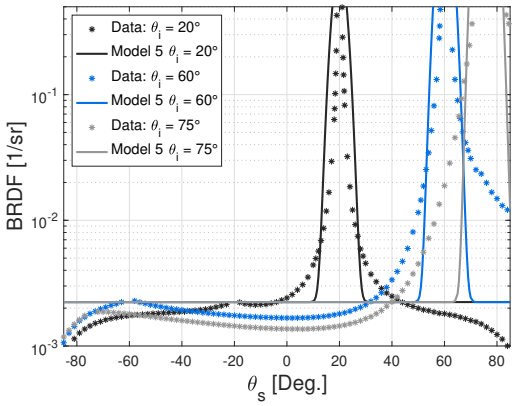

(e) PNT01014 measurements and model 5 fit

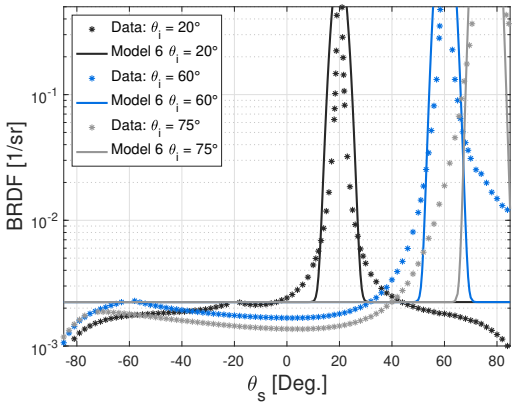

(f) PNT01014 measurements and model 6 fit

Figure 53. All PNT01014 NIR Backscatter Results

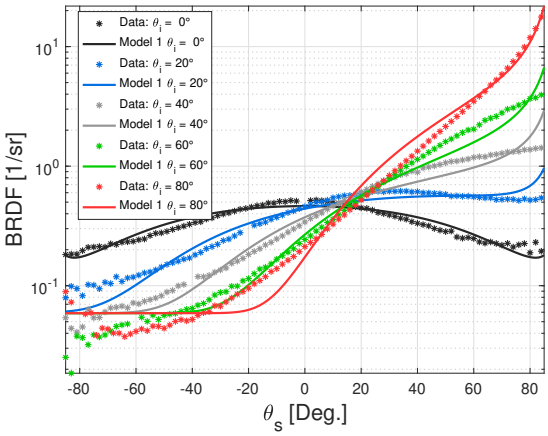

(a) STD00696 measurements and model 1 fit

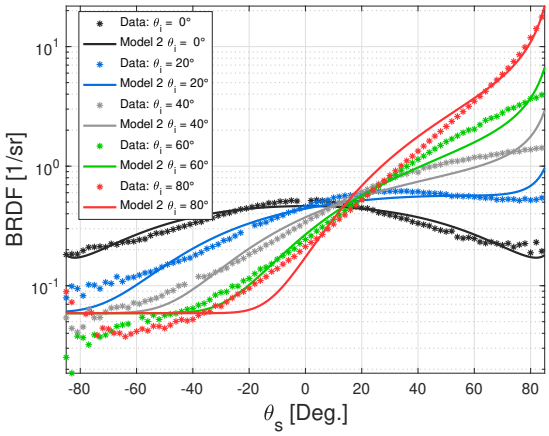

(b) STD00696 measurements and model 2 fit

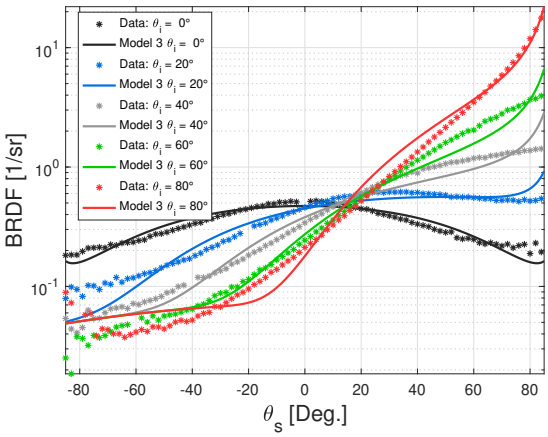

(c) STD00696 measurements and model 3 fit

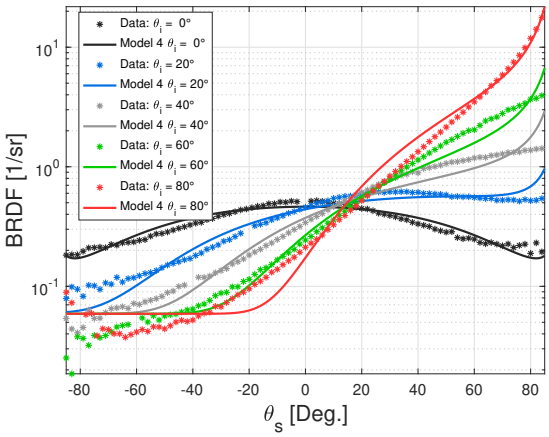

(d) STD00696 measurements and model 4 fit

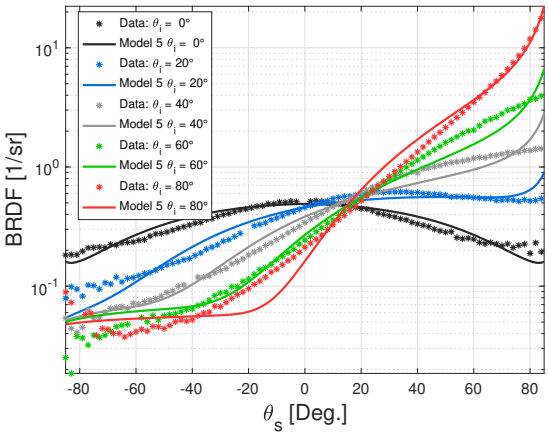

(e) STD00696 measurements and model 5 fit

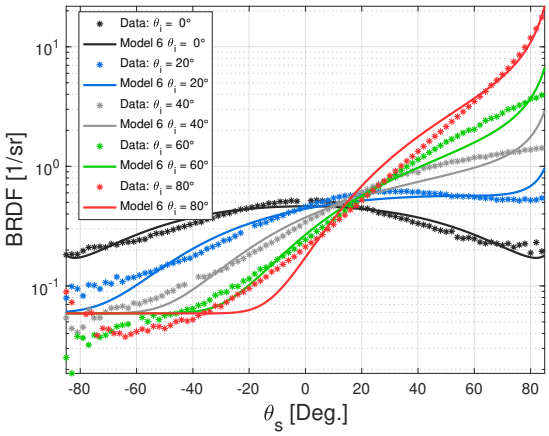

(f) STD00696 measurements and model 6 fit

Figure 54. Resulting six models fit to NIST standard STD00696 illuminated by a MWIR source.

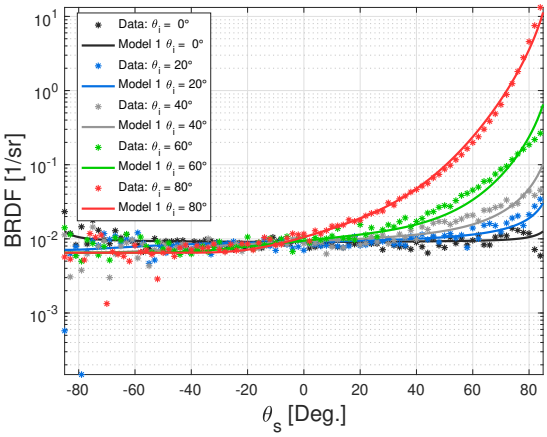

(a) STD00698 measurements and model 1 fit

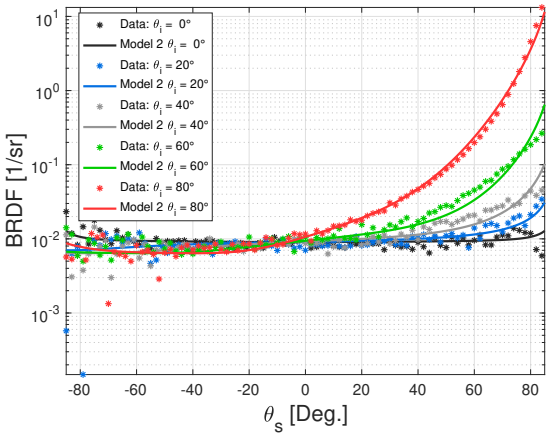

(b) STD00698 measurements and model 2 fit

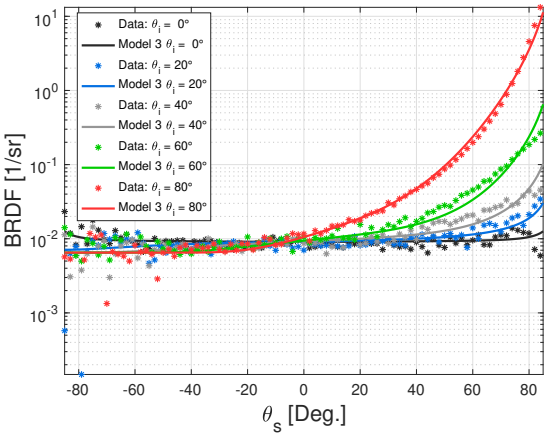

(c) STD00698 measurements and model 3 fit

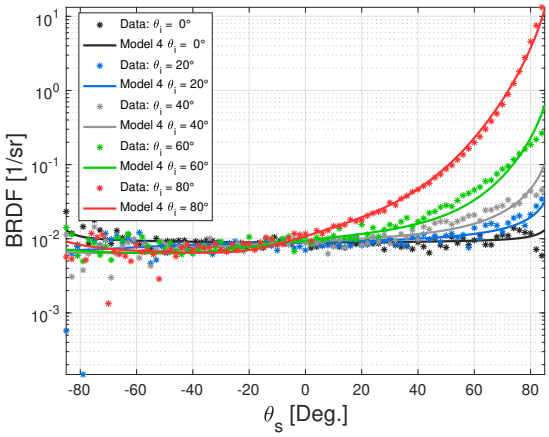

(d) STD00698 measurements and model 4 fit

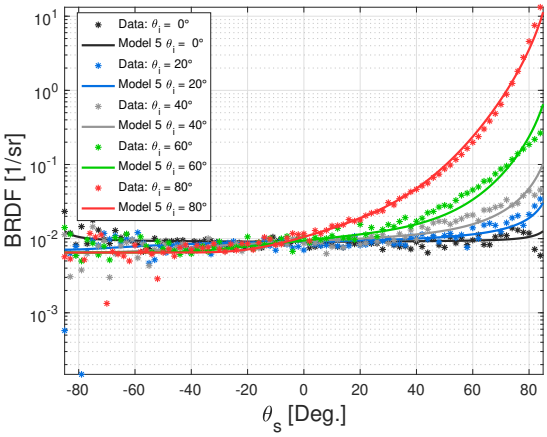

(e) STD00698 measurements and model 5 fit

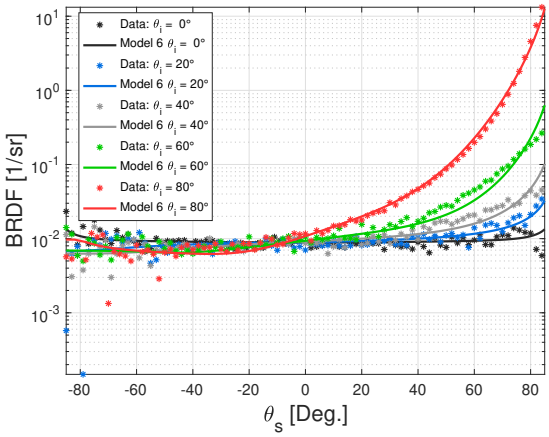

(f) STD00698 measurements and model 6 fit

Figure 55. Resulting six models fit to NIST standard STD00698 illuminated by a MWIR source.

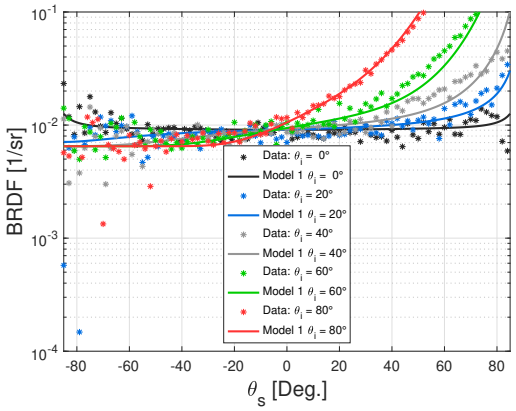

(a) STD00698 measurements and model 1 fit

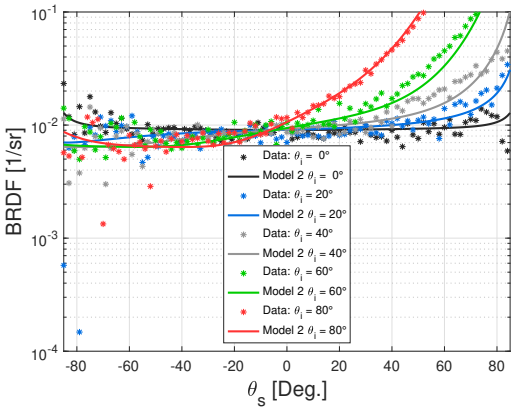

(b) STD00698 measurements and model 2 fit

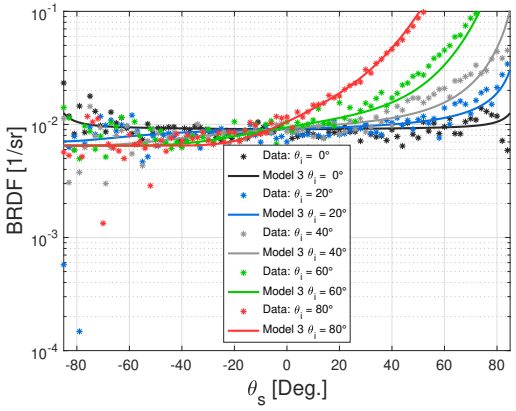

(c) STD00698 measurements and model 3 fit

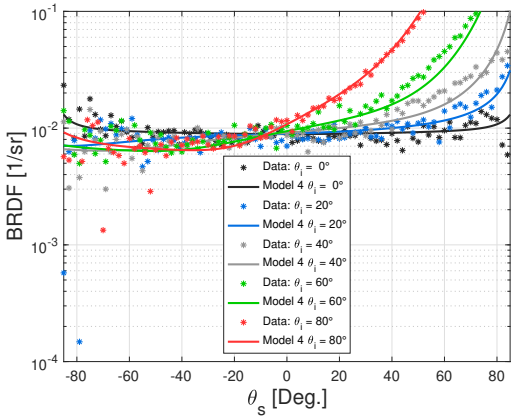

(d) STD00698 measurements and model 4 fit

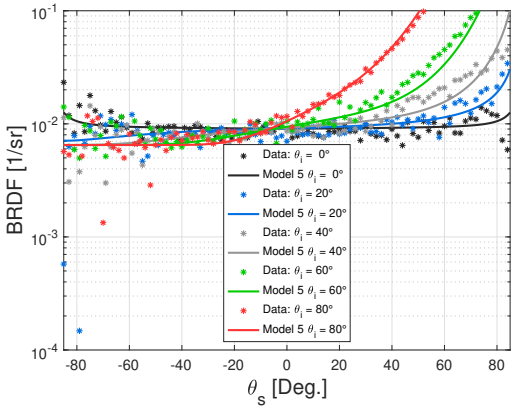

(e) STD00698 measurements and model 5 fit

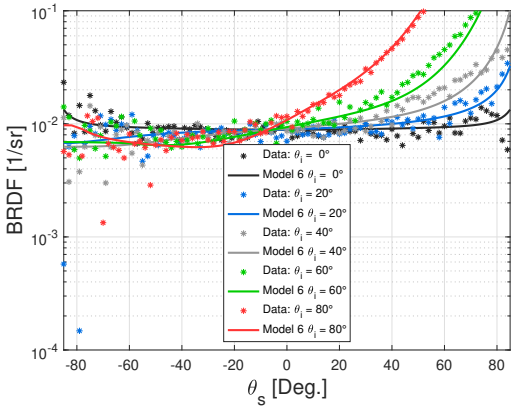

(f) STD00698 measurements and model 6 fit

Figure 56. All STD00698 MWIR Results

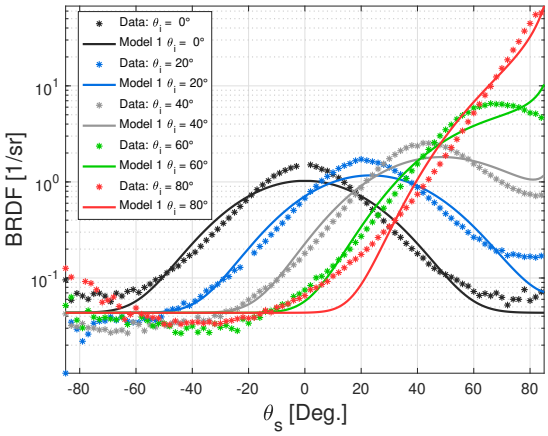

(a) STD00699 measurements and model 1 fit

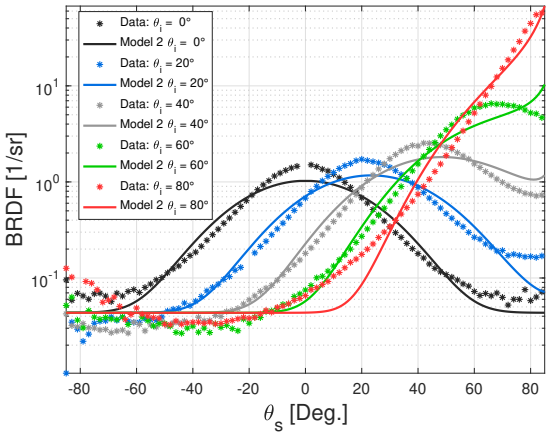

(b) STD00699 measurements and model 2 fit

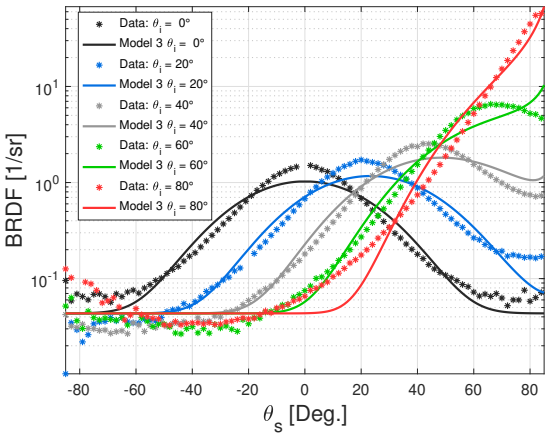

(c) STD00699 measurements and model 3 fit

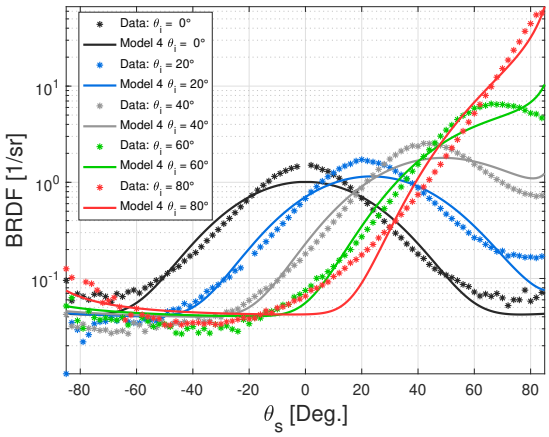

(d) STD00699 measurements and model 4 fit

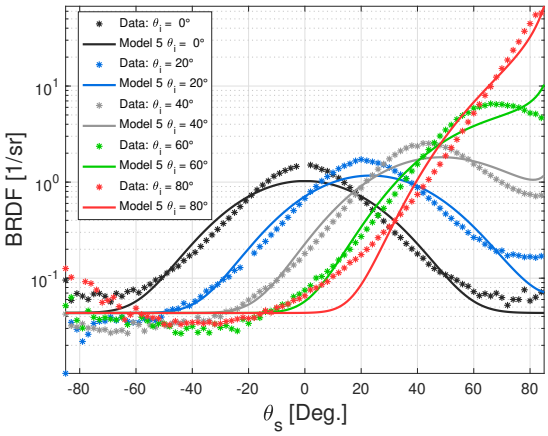

(e) STD00699 measurements and model 5 fit

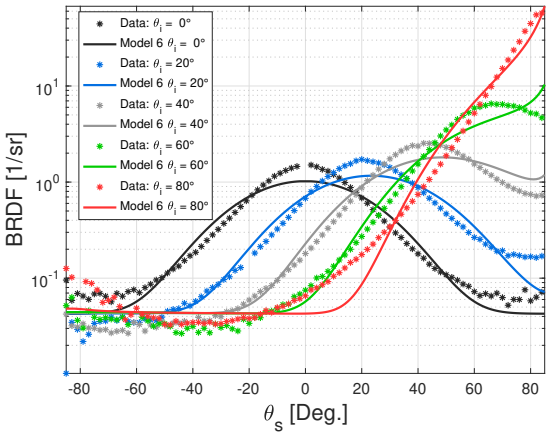

(f) STD00699 measurements and model 6 fit

Figure 57. Resulting six models fit to NIST standard STD00699 illuminated by a MWIR source

Bibliography

1. J. Cierniewski, J. Ceglarek, C. Kaźmierowski, and J.-L. Roujean, "Combined use of remote sensing and geostatistical data sets for estimating the dynamics of shortwave radiation of bare arable soils in europe," *International Journal of Remote Sensing*, vol. 40, no. 5-6, pp. 2359–2374, 2019.

2. M. Yang, W. Xu, J. Li, Z. Zhou, and Y. Lu, "A modified version of BRDF model based on Kubelka-Munk theory for coating materials," *Optik*, p. 162982, 2019.

3. M. A. Heald and J. B. Marion, *Classical electromagnetic radiation*. Dover, 2012.

4. E. Hecht, *Optics*. Pearson, 2017.

5. J. D. Jackson, *Classical electrodynamics*. John Wiley & Sons, 2007.

6. X. Li, L. Xie, and X. Zheng, "The comparison between the Mie theory and the Rayleigh approximation to calculate the EM scattering by partially charged sand," *Journal of Quantitative Spectroscopy and Radiative Transfer*, vol. 113, no. 3, pp. 251–258, 2012.

7. A. C. Melissinos and J. Napolitano, *Experiments in modern physics*. Gulf Professional Publishing, 2003.

8. R. L. Cook and K. E. Torrance, "A reflectance model for computer graphics," *ACM Transactions on Graphics (TOG)*, vol. 1, no. 1, pp. 7–24, 1982.

9. J. Maxwell, J. Beard, S. Weiner, D. Ladd, and S. Ladd, "Bidirectional reflectance model validation and utilization.," tech. rep., Environmental Research Inst of Michigan Ann Arbor Infrared and Optics Div, 1973.

10. B. P. Sandford and D. C. Robertson, "Infrared reflectance properties of aircraft paints," *Proc. IRIS Targets, Backgrounds, and Discrimination*, pp. 111–127, 1985.

11. G. J. Zissis, J. S. Accetta, and D. L. Shumaker, "The infrared & electro-optical systems handbook. sources of radiation, volume 1," tech. rep., Infrared Information and Analysis Center Ann Arbor, MI, 1993.

12. R. W. Boyd, "Radiometry and the detection of optical radiation," *New York, John Wiley and Sons, 1983, 261 p.*, 1983.

13. D. S. Immel, M. F. Cohen, and D. P. Greenberg, "A radiosity method for non-diffuse environments," in *ACM SIGGRAPH Computer Graphics*, vol. 20, pp. 133–142, ACM, 1986.

14. F. E. Nicodemus, J. C. Richmond, J. J. Hsia, I. W. Ginsberg, and T. Limperis, "Geometrical considerations and nomenclature for reflectance," *Final Report National Bureau of Standards, Washington, DC. Inst. for Basic Standards.*, 1977.

15. S. D. Butler and M. A. Marciniak, "Robust categorization of microfacet BRDF models to enable flexible application-specific BRDF adaptation," in *Reflection, Scattering, and Diffraction from Surfaces IV*, vol. 9205, p. 920506, International Society for Optics and Photonics, 2014.

16. S. M. Rusinkiewicz, "A new change of variables for efficient BRDF representation," in *Rendering techniques' 98*, pp. 11–22, Springer, 1998.

17. R. Montes and C. Ureña, "An Overview of BRDF Models," *Technical Report, University of Granada*, pp. 1–26, 2012.

18. S. D. Butler, "Experimental and Theoretical Basis for a Closed-Form Spectral BRDF Model," 2015.

19. J. F. Blinn, "Models of light reflection for computer synthesized pictures," in *ACM SIGGRAPH computer graphics*, vol. 11, pp. 192–198, ACM, 1977.

20. J.-L. Roujean, M. Leroy, and P.-Y. Deschamps, "A bidirectional reflectance model of the Earth's surface for the correction of remote sensing data," *Journal of Geophysical Research: Atmospheres*, vol. 97, no. D18, pp. 20455–20468, 1992.

21. M. Montanaro, "NEFDS Beard-Maxwell BRDF model implementation in Matlab," *Rochester Institute of Technology, DIRS Technical Report 2007-83*, vol. 174, 2007.

22. S. L. J. Townshend, "High performance algorithms for global BRDF retrieval," 1997.

23. C. Walthall, J. Norman, J. Welles, G. Campbell, and B. Blad, "Simple equation to approximate the bidirectional reflectance from vegetative canopies and bare soil surfaces," *Applied Optics*, vol. 24, no. 3, pp. 383–387, 1985.

24. T. Nilson and A. Kuusk, "A reflectance model for the homogeneous plant canopy and its inversion," *Remote Sensing of Environment*, vol. 27, no. 2, pp. 157–167, 1989.

25. W. Wanner, X. Li, and A. Strahler, "On the derivation of kernels for kernel-driven models of bidirectional reflectance," *Journal of Geophysical Research: Atmospheres*, vol. 100, no. D10, pp. 21077–21089, 1995.

26. C. Schlick, "A customizable reflectance model for everyday rendering," in *Fourth Eurographics Workshop on Rendering*, pp. 73–83, Paris, France, 1993.

27. C. Schlick, "An inexpensive BRDF model for physically-based rendering," in *Computer graphics forum*, vol. 13, pp. 233–246, Wiley Online Library, 1994.

28. M. Oren and S. K. Nayar, "Generalization of Lambert's reflectance model," in *Proceedings of the 21st annual conference on computer graphics and interactive techniques*, pp. 239–246, ACM, 1994.

29. A. Murphy, "Modified Kubelka–Munk model for calculation of the reflectance of coatings with optically-rough surfaces," *Journal of Physics D: Applied Physics*, vol. 39, no. 16, p. 3571, 2006.

30. H. R. Kang, *Computational color technology*. Spie Press Bellingham, 2006.

31. P. Kubelka and F. Munk, "An article on optics of paint layers," *Z. Tech. Phys*, vol. 12, no. 593-601, 1931.

32. M. Doi and S. Tominaga, "Spectral estimation of human skin color using the kubelka-munk theory," in *Color Imaging VIII: Processing, Hardcopy, and Applications*, vol. 5008, pp. 221–228, International Society for Optics and Photonics, 2003.

33. J. Saunderson, "Calculation of the color of pigmented plastics," *JOSA*, vol. 32, no. 12, pp. 727–736, 1942.

34. P. B. Johnson and R.-W. Christy, "Optical constants of the noble metals," *Physical review B*, vol. 6, no. 12, p. 4370, 1972.

35. F. M. Cady, D. R. Bjork, J. Rifkin, and J. C. Stover, "BRDF error analysis," in *Scatter from Optical Components*, vol. 1165, pp. 154–164, International Society for Optics and Photonics, 1990.

REPORT DOCUMENTATION PAGE

Form Approved
OMB No. 0704-0188

1. REPORT DATE *(DD-MM-YYYY)*	2. REPORT TYPE	3. DATES COVERED *(From - To)*

4. TITLE AND SUBTITLE	5a. CONTRACT NUMBER
	5b. GRANT NUMBER
	5c. PROGRAM ELEMENT NUMBER
6. AUTHOR(S)	5d. PROJECT NUMBER
	5e. TASK NUMBER
	5f. WORK UNIT NUMBER

7. PERFORMING ORGANIZATION NAME(S) AND ADDRESS(ES)	8. PERFORMING ORGANIZATION REPORT NUMBER
9. SPONSORING/MONITORING AGENCY NAME(S) AND ADDRESS(ES)	10. SPONSOR/MONITOR'S ACRONYM(S)
	11. SPONSOR/MONITOR'S REPORT NUMBER(S)

12. DISTRIBUTION/AVAILABILITY STATEMENT

13. SUPPLEMENTARY NOTES

14. ABSTRACT

15. SUBJECT TERMS

16. SECURITY CLASSIFICATION OF:			17. LIMITATION OF ABSTRACT	18. NUMBER OF PAGES	19a. NAME OF RESPONSIBLE PERSON
a. REPORT	b. ABSTRACT	c. THIS PAGE			Lt Col Samuel D. Butler, Ph.D
					19b. TELEPHONE NUMBER *(Include area code)*
		U	UU	128	937-255-3636 x4385